LBL-1019

A HIGH STATISTICS STUDY OF THE REACTION $\pi^- p \rightarrow \pi^0 n$ BETWEEN 1.0 AND 2.4 GeV/c

Jerry Earl Nelson
(Ph. D. Thesis)

August 1972

AEC Contract No. W-7405-eng-48

LBL-1019

DISCLAIMER

Contents

A HIGH STATISTICS STUDY OF THE REACTION $\pi^- p \rightarrow \pi^o n$ BETWEEN 1.0 AND 2.4 GeV/c

Jerry Earl Nelson

Lawrence Berkeley Laboratory
University of Califonria
Berkeley, California

ABSTRACT

Differential cross sections for the reaction $\pi^- p \rightarrow \pi^o n$ were measured at six incident pion momenta in the region 1.0 to 2.4 GeV/c. The experiment was performed at the Bevatron, using a negative pion beam focused onto a 20-cm liquid hydrogen target. The reaction was identified and measured using the decay of the π^o into two γ rays. The γ rays were detected by a set of lead-plate spark chambers which surrounded the target, covering about 3.7 π solid angle. The chambers were seven to eight radiation lengths thick to insure high γ-ray conversion probability and they covered five sides of a cube, the beam's entrance side being left open. This opening was nearly closed by a set of lead-scintillator sandwich gamma counters. At each momentum a very clean sample of between 2500 and 6500 π^o events with both γ-rays seen in the spark chambers was obtained. The spark chamber geometry was corrected in these events by a Monte Carlo calculation and the corrected sample was fitted with Legendre polynomials.

A comparison of the differential cross section with the predictions of phase shift analyses was made. The t-distributions were compared with the predictions of Regge theory. Extrapolated forward cross sections were compared with dispersion calculations.

Since the event trigger was on neutral final states the cross sections for $\pi^- p \rightarrow$ neutrals and the reactions $\pi^- p \rightarrow \eta n$, $\pi^o \pi^o n$, $\pi^o \pi^o \pi^o n$ were also obtained.

I. INTRODUCTION

The study of so-called elementary particles has received an enormous amount of attention in the last twenty years. With the advent of particle accelerators, more and more complex and sophisticated experiments have been performed and increasingly subtle theories formulated. In spite of this staggering effort, the properties of elementary particles are as yet only poorly understood.

The important interactions of elementary particles are usually categorized into strong, electromagnetic, and weak interactions. The strong interactions have been studied in the greatest detail, but in spite of this, we have the least understanding of this force compared to the other types of interactions. Pion-nucleon interactions are usually considered the simplest of the experimentally accessible strong interactions. Even among these, those reactions producing many particle final states are typically quite intractable.

The simplest pion-nucleon interaction is elastic scattering, with three reactions easily accessible experimentally:

$$\pi^+ p \rightarrow \pi^+ p \tag{1}$$

$$\pi^- p \rightarrow \pi^- p \tag{2}$$

$$\pi^- p \rightarrow \pi^o n \tag{3}$$

the existence of three charge states for the pion, and two for the nucleon implies that the interaction can take place in both isospin 3/2 and isospin 1/2 states. Reaction (1) is purely isospin 3/2, but (2) and (3) are mixtures of I = 3/2 and 1/2 states. Because of this mixture, the determination of the I = 3/2 and 1/2 amplitudes and their relative phase requires the measurement of all three reactions. In particular:

$$d\sigma/d\Omega(I=1/2) = 3/2[d\sigma/d\Omega(\pi^- p \rightarrow \pi^- p) + d\sigma/d\Omega(\pi^- p \rightarrow \pi^o n)] - 1/2\ d\sigma/d\Omega(\pi^+ p \rightarrow \pi^+ p) \quad (4)$$

thus all three reactions are needed to obtain the I=1/2 interaction. Figure 1 shows the total cross sections for $\pi^{\pm}$ p scattering and indicates the positions of some well known resonances. Figure 2 shows the I=3/2, 1/2 cross sections. In both figures, note the influence of resonances on the cross sections. Table I shows the kinematics for this experiment.

Formally, one can expand the scattering amplitude (for each isospin state) in angular momentum and obtain the "partial wave expansion" for the pion-nucleon scattering amplitude. The determination of the parameters in this expansion ("phase shifts") has been a major occupation in high energy physics. In principle these parameters can be derived from the study of reactions (1), (2), and (3).

In the low energy region below 1 GeV/c the phase-shifts for pion-nucleon scattering are fairly well known and the properties of a number of pion-nucleon resonances are firmly established. [1,2] In the high energy region above 4 GeV/c the partial wave expansion becomes rather cumbersome due to the large number of parameters needed; other theories have been developed to explain the data in this region.[1-5] Because of the success of Regge theory at high energies and partial wave analysis at low energies, it becomes particularly interesting to investigate both theoretically and experimentally the intermediate energy region 1 to 4 GeV/c.

Reactions (1) and (2) are relatively straightforward to measure since they have charged particles in their final states. The differential cross sections for these two reactions have been measured accurately over

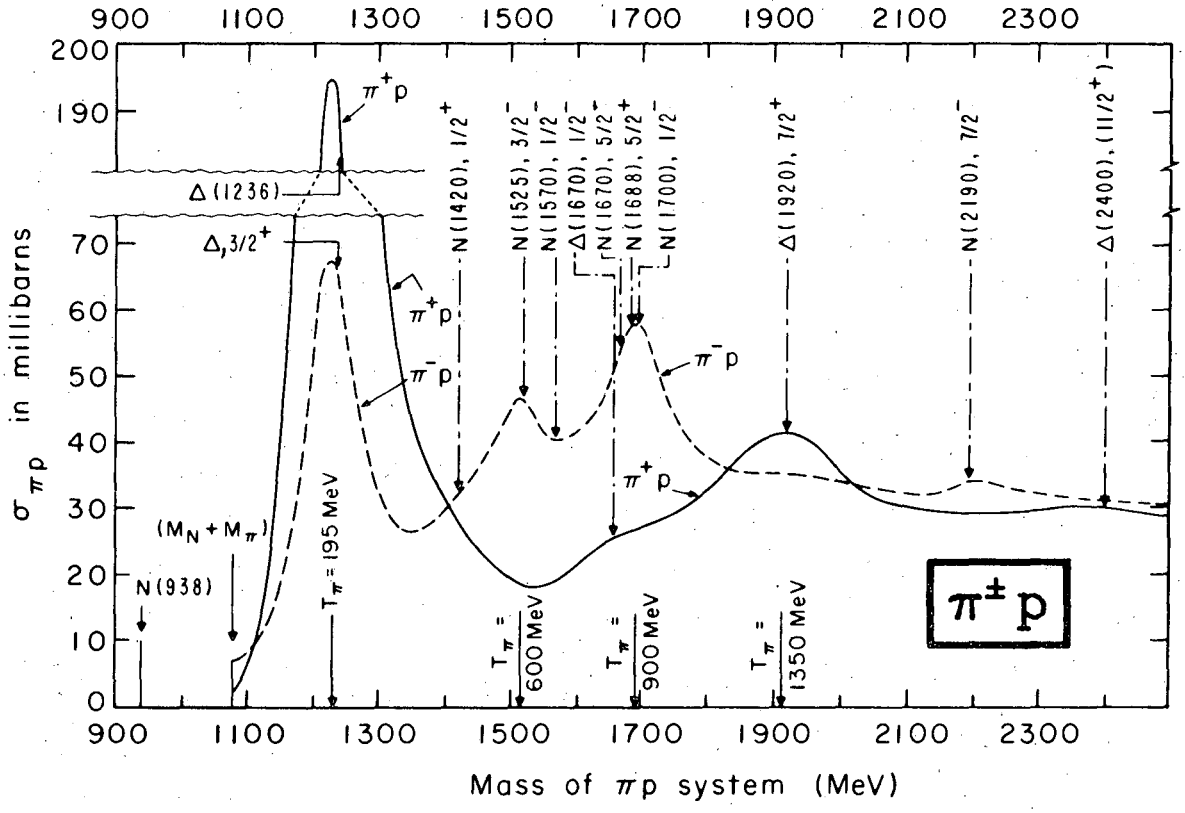

XBL 728-1394

Fig. 1. $\pi^\pm p$ total cross sections (from Ref. 26).

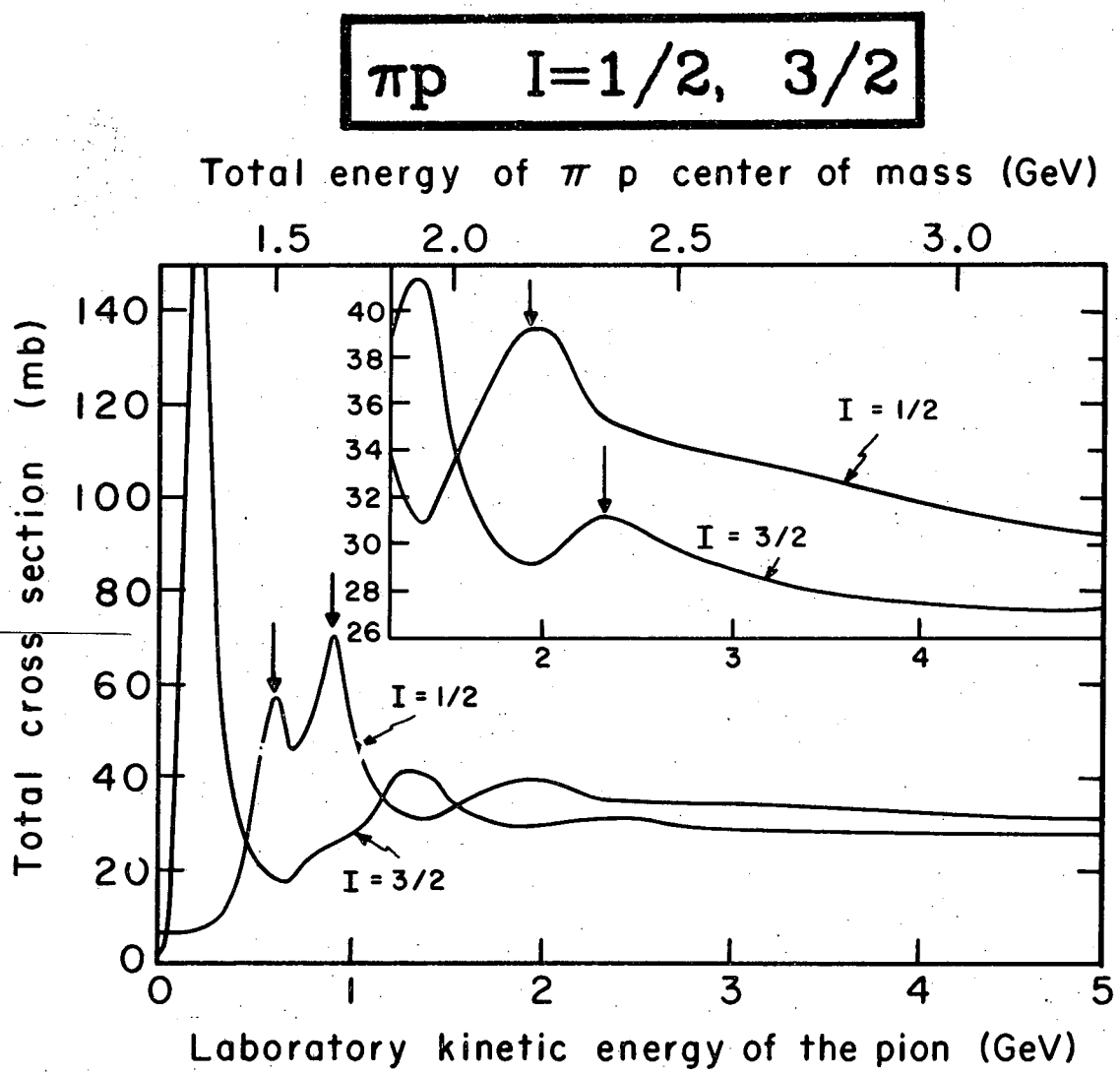

XBL 728-1395

Fig. 2. πp I = 1/2, 3/2 total cross sections (from Ref. 26).

Table I . Kinematics for $\pi^- p \rightarrow \pi^o n$

$p_{\pi^-}^{lab}$	$T_{\pi^-}^{lab}$	s	$\sqrt{s}$, $E_{c.m.}$	t_{max}	$p^{c.m.}$
1.030	.900	2.850	1.688	-1.31	.572
1.590	1.457	3.895	1.974	-2.28	.756
1.790	1.656	4.269	2.066	-2.64	.813
1.990	1.855	4.643	2.155	-3.00	.867
2.190	2.055	5.018	2.240	-3.37	.917
2.390	2.255	5.392	2.322	-3.73	.966

$p_{\pi^-}^{lab}$ is the incident beam momentum in GeV/c.

$T_{\pi^-}^{lab}$ is the incident beam kinetic energy in GeV.

S is the invariant mass^2 of the system in GeV^2.

$\sqrt{s}$ or $E_{c.m.}$ is the invariant mass of the system in GeV

t_{max} is the maximum momentum transfer^2 in $(GeV/c)^2$

$p_{c.m.}$ is the center of mass frame particle momentum in GeV/c.

a wide range of energies. Extensive polarization measurements for these reactions also exist.

Reaction (3), called "charge-exchange", has been given much less attention mainly because of the increased difficulty in measuring neutral final states. Reaction (3) can be particularly useful in constraining the I=3/2 and 1/2 scattering amplitudes ($F_{3/2}$ and $F_{1/2}$) since it depends on their difference:

$$d\sigma/d\Omega = 2/9 \left|F_{3/2} - F_{1/2}\right|^2 \qquad (5)$$

Charge exchange has been studied in this energy range with only a few experiments.[6-9] References 7 and 8 have fairly good statistics in the region 1.0 GeV/c but they have no data in the higher energy regions. While Refs. 6 and 9 have higher-energy data, these experiments have low statistical accuracy based on hundreds of π^o events, and also they use a rather unfavorable geometry which makes it difficult to avoid systematic uncertainties. An unambiguous determination of phase shifts at these energies will certainly require precise charge exchange measurements. This experiment gives results from thousands of π^o events at each momentum and uses a favorable geometry to minimize corrections. Charge exchange can be studied by detecting the neutron or the γ-rays from the decay $\pi^o \to \gamma\gamma$. The latter approach has been used here and the γ-rays are detected by using lead plate spark chambers to convert the γ-rays to charged particles.

II. EXPERIMENTAL PROCEDURE AND EQUIPMENT

A. General Method

The results described in this thesis are derived from two separate experiments conducted at the Bevatron. The first experiment was performed at the momenta 880, 930, 980, 1030, 1080, 1130 MeV/c. Only data taken at 1030 MeV/c were useful for this thesis. The second experiment was performed at momenta of 1590, 1790, 1990, 2190 and 2390 MeV/c. Data taken at all of these momenta were used in this analysis.

The main purpose of the first experiment was to study the reaction $\pi^- p \rightarrow N^*(1688) \rightarrow n\eta$. [10] Neutron counters measured both the neutron's direction and velocity. Twenty such counters were set up over a wide range of laboratory angles. The information thus gained effectively reduced the background from other processes. At 1030 MeV/c data were also taken without the neutron counters. This provided a check on the neutron counters and also supplied the data at 1030 MeV/c for this thesis.

The second experiment was designed to study the reaction $\pi^- p \rightarrow \pi^o \pi^o n$ [11] using the same apparatus by moving the neutron counters somewhat and making slight changes to the beam line to achieve the higher momenta. Extensive data were taken at 1590, 1790, 1990, 2190 and 2390 MeV/c without neutron counters, both for calibration purposes and to study charge exchange.

The experimental area and general beam layout are shown in Fig. 3. Negative pions were produced in the third quadrant of the Bevatron by collisions of circulating protons with an aluminum target. The Bevatron magnetic field and a series of bending and focusing magnets were used to deflect, momentum-analyze and finally refocus the particle beam on our hydrogen target where the reactions of interest were produced.

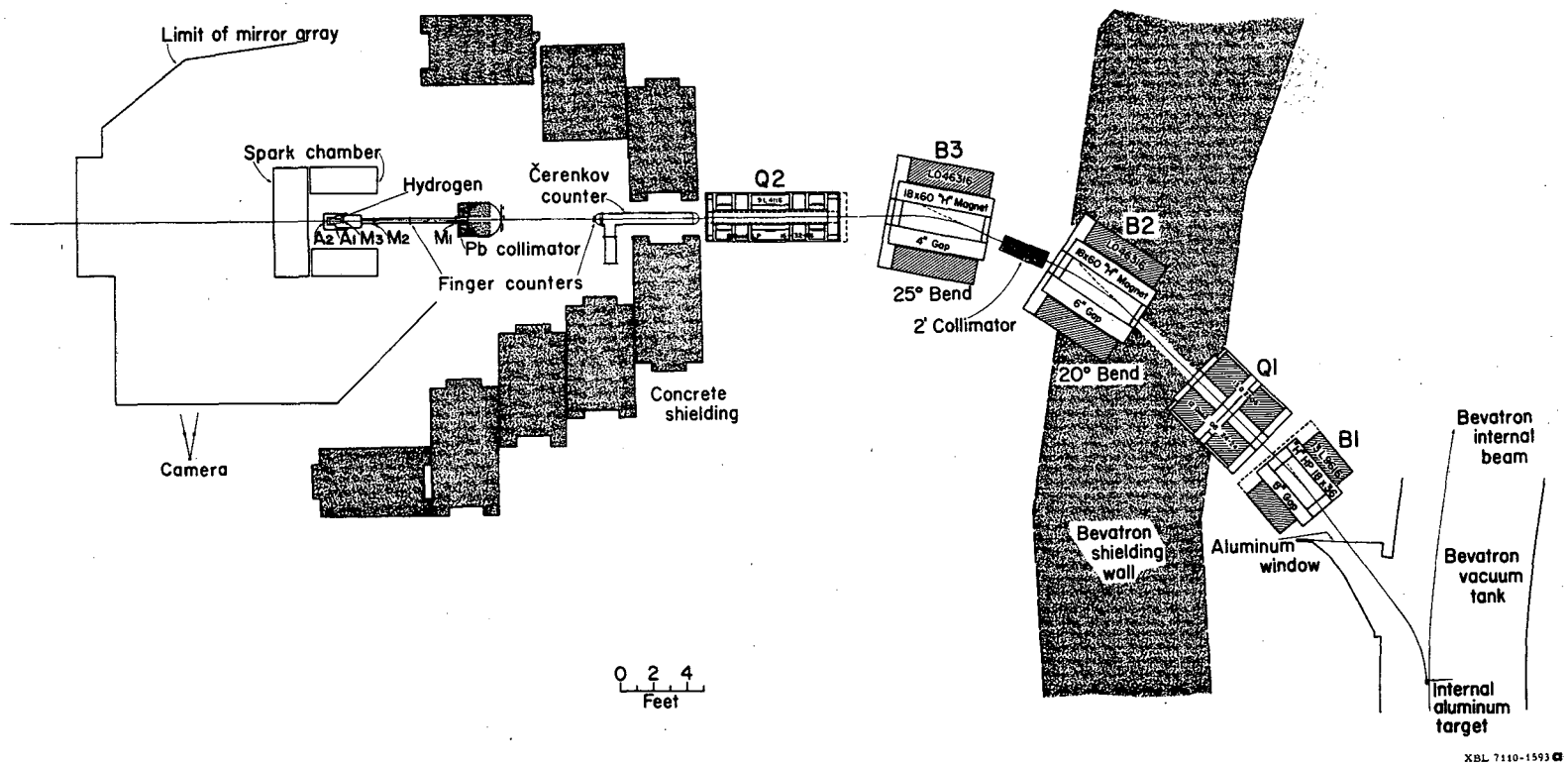

Fig. 3. The experimental set up for the investigation of the reactions $\pi^- p \rightarrow$ neutrals.

The pion beam was defined electronically by a coincidence between three scintillation counters upstream of the hydrogen target. Two sets of crossed finger counters further defined the incident pion direction and position. The hydrogen target was surrounded by scintillation counters which vetoed any events with charged particles leaving the target.

The entire target, veto-basket assembly was located inside a cubical array of spark chambers which were triggered when a charged particle entered the hydrogen target and no charged particles left the target, i.e., the final state was all neutral particles. The spark chambers covered five sides of a cube, with the upstream side left open for the beam to enter. These chambers contained about seven radiation lengths of lead to convert and detect gamma-rays from the neutral final state.

A variety of reactions at these energies are capable of producing neutral final states:

$$\begin{aligned}
\pi^- p &\rightarrow \pi^o n && (\rightarrow 2\gamma\text{'s}) \\
&\rightarrow \eta n && (\rightarrow 2,\ 6\gamma\text{'s}) \\
&\rightarrow \omega n && (\rightarrow 3\gamma\text{'s}) \\
&\rightarrow \pi^o\pi^o n && (\rightarrow 4\gamma\text{'s} \\
&\rightarrow \pi^o\pi^o\pi^o n && (\rightarrow 6\gamma\text{'s}) \\
&\rightarrow 4\pi^o n && (\rightarrow 8\gamma\text{'s}) \\
&\rightarrow \Lambda K^o && (\rightarrow 2,\ 6\gamma\text{'s}) \\
&\rightarrow \Sigma^o K^o && (\rightarrow 3,\ 7\ \gamma\text{'s}) \\
&\rightarrow \Lambda^o K^o \pi^o && (\rightarrow 4,\ 8\ \gamma\text{'s})
\end{aligned}$$

In the reaction of interest $\pi^- p \rightarrow \pi^o n$, the π^o decays immediately into two gamma-rays. These gamma-rays formed visible showers in the spark

chambers which were then photographed with the aid of a complex mirror system. The directions of the two gamma-rays were then determined. From the observed spatial distributions of these gamma-rays, the angular distribution of the decaying π^o was determined. Because many other reactions may produce γ-rays which are detected in the spark chambers, a major part of the analysis was spent in eliminating these undesirable events.

B. Apparatus

1. Pion Beam

The pions produced by the target in the internal proton beam were deflected by the Bevatron magnetic field, and a series of magnets further defined and focused the beam. The bending magnets defining the momentum were wire-orbited. The beam was designed using the program OPTIK.[12]

To handle a reasonable range of momenta, a bending magnet was used as the first beam element. Next a quadrupole doublet was used to form a focus where momentum selection was done. (In the 1600 to 2400 MeV/c beam, an additional bending magnet preceded this focus.) A brass collimator was placed in this focal plane and specified the central momentum, the momentum bite and to some extent the flux of the beam. This focus was followed by a bending magnet to specify the particle momentum and a quadrupole triplet which in turn focused the beam onto the hydrogen target. Downstream of the last quadrupole, a 2-ft lead collimator with a 4 by 4-inch aperture provided additional definition of the beam.

The momentum dispersion caused by the Bevatron field and the first bending magnet(s) together with the aperture of the collimator produced a final beam with $\Delta p/p = \pm .01$.

During the data-taking, a low pressure Freon Cerenkov counter 5-ft long was used to measure the electron and muon contamination in the beam (see Fig. 4). This counter detected all particles with velocities greater than the threshold velocity determined by the gas pressure.

The beam composition is given in Table II.

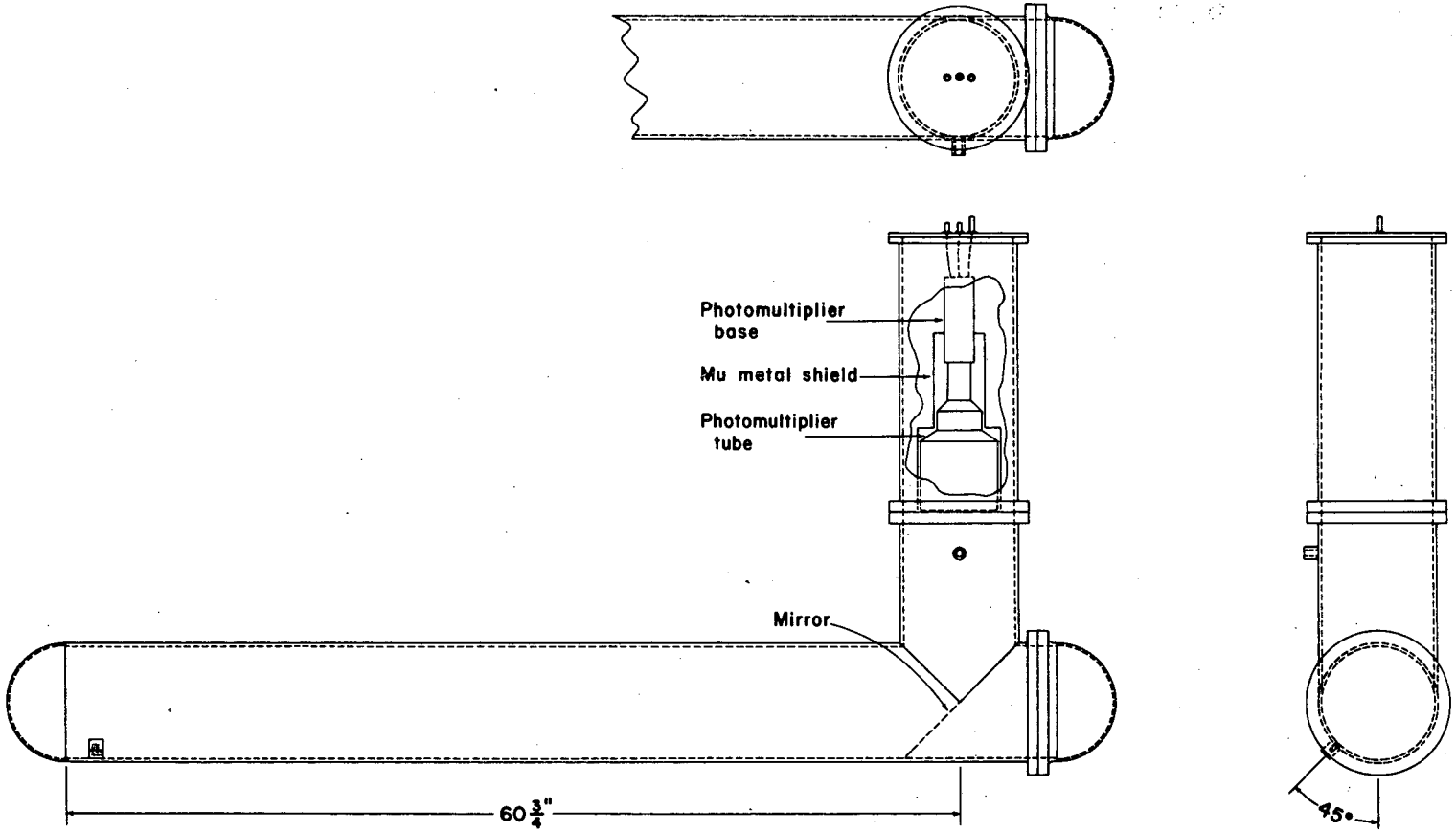

Čerenkov Counter

XBL 7110-1594

Fig. 4. Schematic of the Cerenkov counter.

Table II. Beam composition

P (MeV/c)	Percentage of beam π^-	e^-	μ^-
1030	89	7	4
1600	88.9	8.5	2.6
1800	92.4	5.6	2.0
2000	94.4	4.6	1.0
2200	96.2	3.0	.8
2400	97.2	2.3	.5

The beam intensity varied from 20 to 100 x 10^3 pions per second. The Bevatron spill was about 1.0 sec. long. Typically about 5% of the beam was vetoed because particles were too close to one another. (See Sec. 3 below.) The data-taking was ~ 5 to 8 pictures per Bevatron pulse.

2. Liquid Hydrogen Target

The liquid hydrogen was contained in a Mylar cylinder 8-in. long and 4-in. in diameter with .0075 in. wall thickness (Fig. 5). This flask was in an evacuated jacket of .030-in. aluminum with entrance and exit windows of .010-in. Mylar through which the beam passed. On the upstream end of this jacket a long pipe was connected to support the target jacket and surrounding counters, and to provide liquid hydrogen to the target from the reservoir (Fig. 6).

The reinforced section of the jacket had a re-entrant hole 4-in. in diameter to facilitate placement of the last beam counter close to the hydrogen flask. This counter (M_3) had a wafer of scintillator 1.7 in. from the flask, and an air light guide through which the beam passed axially (Fig. 7).

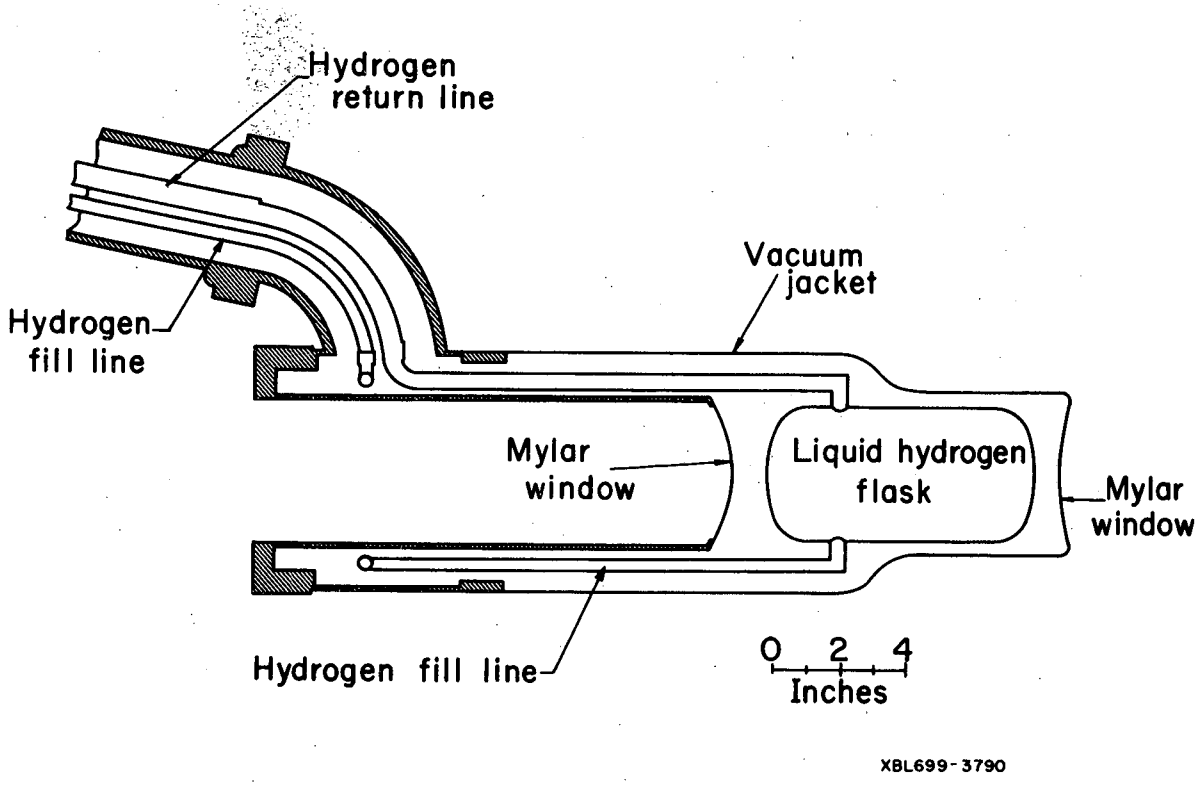

Fig. 5. The hydrogen target.

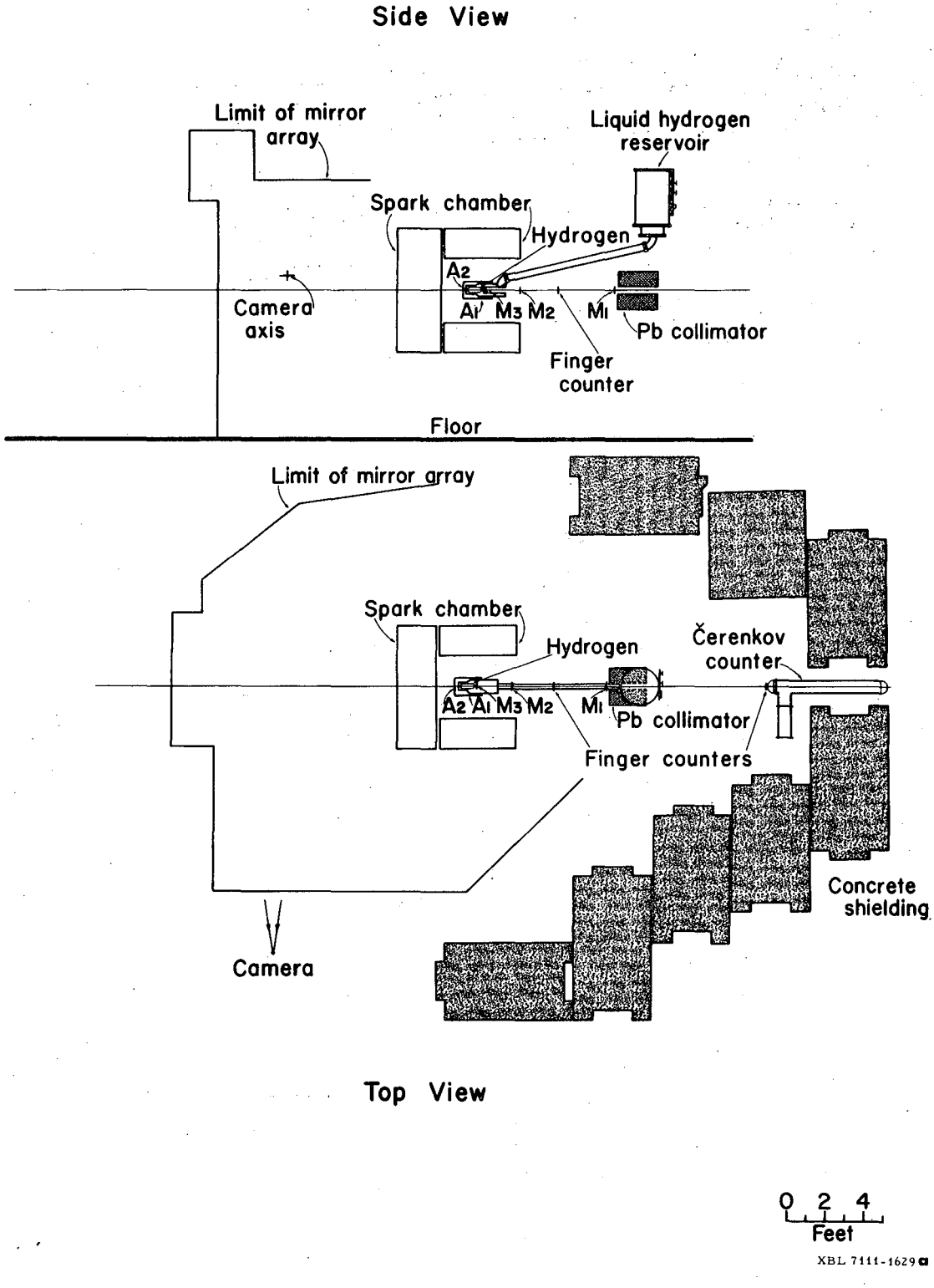

Fig. 6. The experimental layout.

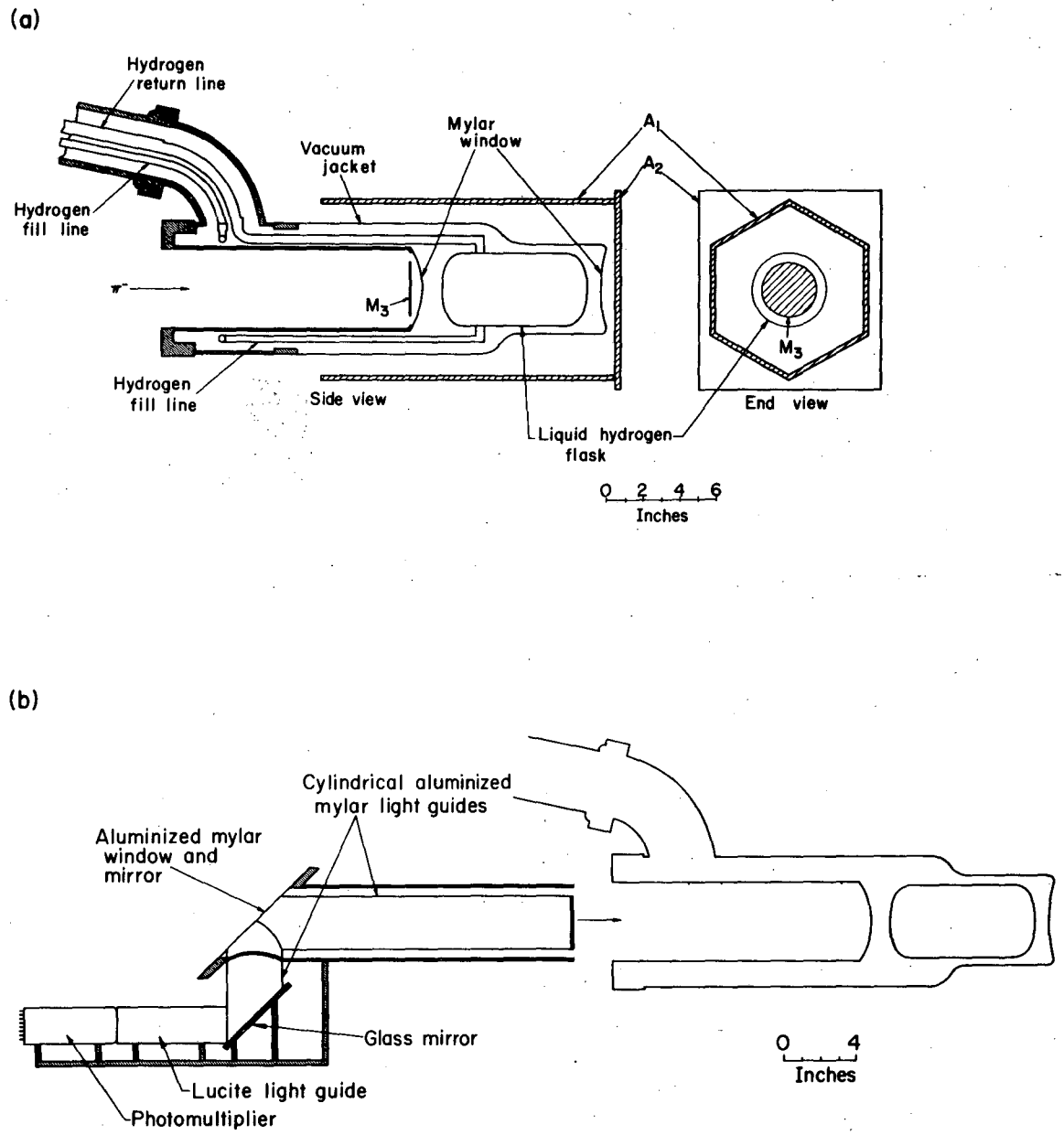

Fig. 7. The hydrogen target, veto counters, and the beam defining counter M3.

Other than the hydrogen, scattering centers which could produce logically acceptable events were the last beam counter, the Mylar walls of the hydrogen flask, and the Mylar windows. These provided .207 grams/cm^2 to the beam while the hydrogen provided 1.44 grams/cm^2. For processes with a neutral final state, we found the counting rate with hydrogen/counting rate without hydrogen was about 9/1.

3. Electronics and Scintillation Counters

The scintillation counters were made from "Pilot B" scintillator which is polyvinyl toluene doped with p-terphenyl and p,p'-diphenylstilbene.

The counters defining the beam (M_1, M_2, M_3) and the anticounters surrounding the hydrogen target (A_1, A_2) were viewed by RCA8575 photomultiplier tubes and, except for M_3, had light pipes of twisted Lucite strips. As M_3 was physically buried within the target structure, the pion beam passed through its light guide. For this reason, the light guide used was an air filled cylinder of aluminized Mylar. A thin (.0005 in.) 45 deg. mirror of the same material reflected the light to a photomultiplier outside the beam region (Fig. 7).

Each of the three beam counters was a plane disk. They decreased in size as the beam converged onto the target; M_1, M_2, and M_3 were 4-, 3.5-, and 3-in. in diameter respectively. M_1 was 1/2-in. thick and produced an output pulse which was very stable in time. (This helped define the neutron time-of-flight for the neutron counters used in other parts of the experiment.) M_2 and M_3 were each 1/16-in. thick to minimize scattering. Two sets of 4 by 4 crossed finger counters were also used to help define the particle direction. The upstream set consisted of eight 1.5 by 6-in. scintillators and the downstream set had eight .75 by 3-in. scintillators.

The veto counter surrounding the hydrogen target (A_1) was a 1/4-in. thick hexagonal cylinder viewed by three photomultiplier tubes (Fig. 7). The veto counter downstream of the target (A_2) was an 8-in. square, 1/4-in. thick. This counter was more than 99.9% efficient, since the neutral counting rate with target empty was ~ .04% of the beam rate.

The neutron counter system was not used for the data in this thesis, so no detailed description will be given. Details may be found in Refs. 11 and 13.

The open face of the spark chamber was partially covered with gamma-ray detection counters (Fig. 8). There were four of them (G_1 - G_4), each a multilayer sandwich of 1/4-in. sheets of scintillator alternating with 1/8-in. sheets of lead. There are eight such rectangular sheets of each material. The dimensions of the counters were:

G_1 = 5.5 x 20 in.

G_2 = 26 x 12.5 in.

G_3 = 7 x 20 in.

G_4 = 25.5 x 12 in.

G_2, G_3, and G_4 were each viewed by two Amperex 58AVP photomultiplier tubes placed directly in contact with the smallest side of the sandwich. G_1 had a single 5-in. photomultiplier tube mounted in the same way. These counters were calibrated so they would respond to a minimum ionizing particle passing through a single sheet of scintillator.

Since the two experiments for which this apparatus was designed typically used neutron counters, a rather complex electronic system was designed to insure maximum neutron time-of-flight accuracy. This system is

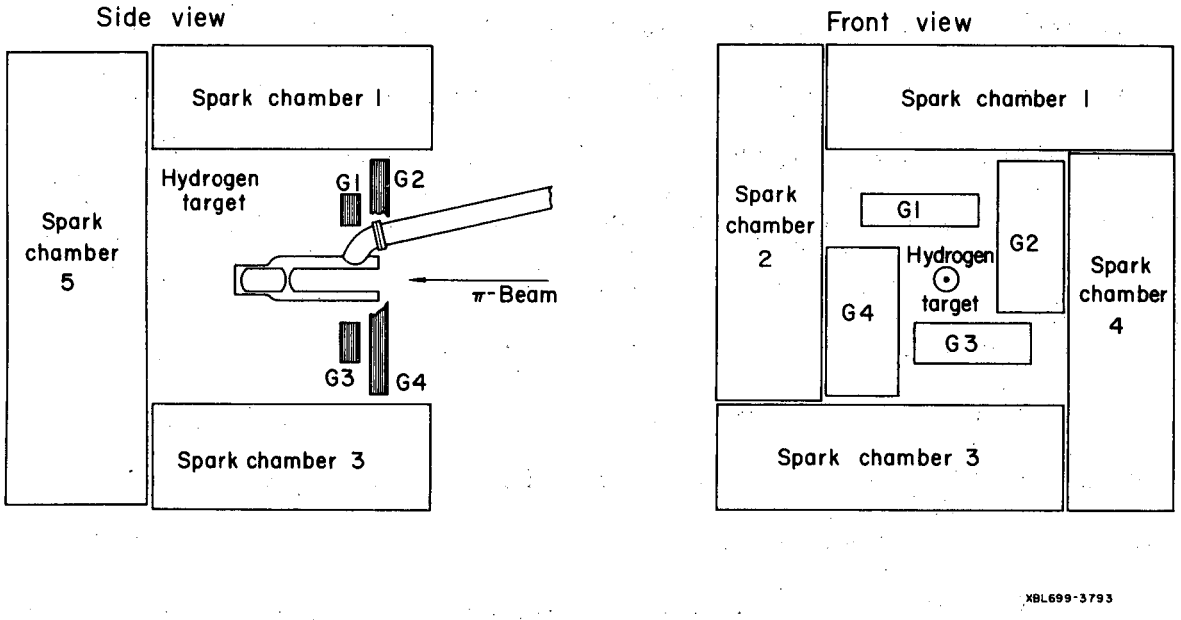

Fig. 8. The arrangement of spark chambers, hydrogen target, and gamma ray detection counters G_i.

described elsewhere.[10,11,13] The much simpler logic needed to acquire the data used here will be described briefly (Fig. 9).

The three beam counters (M_1, M_2, M_3) in coincidence defined a beam particle. This coincidence signal B (for beam) was then fed into a second coincidence unit M (monitor) where it could be vetoed by a DT (dead time) pulse. DT was a signal generated by M_1, designed to eliminate electronics jamming and extra tracks in the spark chambers by vetoing any beam particles too close together in time. M_1 generated a pulse in a special zero-dead-time discriminator, DT_1, 52 nsec earlier than in the regular M_1 discriminator. One output of DT_1 was delayed and triggered a similar unit, DT_2. The outputs of DT_1 and DT_2 were then added to form the DT signal at the input of M. This pulse began 68 nsec before B (at M), ended 2 nsec before B, began again 2 nsec after B had died away, and persisted for another 500 nsec. Thus each B signal was accompanied by its own early and late DT signal which was used as a veto at the M coincidence unit. It did not veto itself but did veto any beam particle nearby in time. Thus if two particles were within 68 nsec of each other, each vetoed the other. If they were within 500 nsec of each other, the earlier vetoed the later.

After the counting efficiency of the beam signal, B, had been rendered rate independent at M, it was fed into another coincidence unit, FIRE, where the target veto counters ($A = A_1 + A_2$) were put in anticoincidence. The output from this unit represented a "neutral final state" and was used to generate a FIRE signal. The FIRE signal performed a variety of functions:

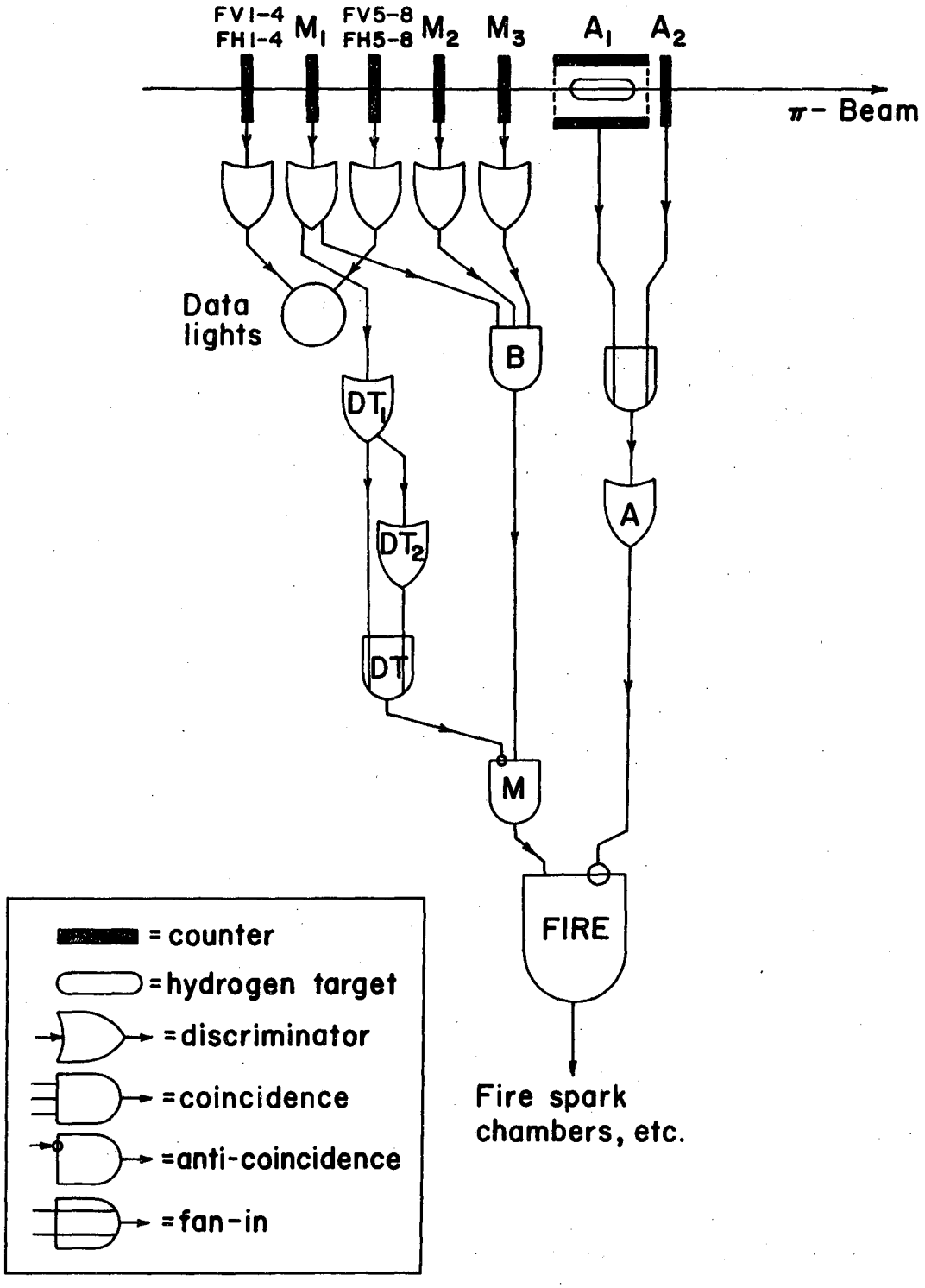

XBL 727-1334

Fig. 9. The electronics.

(1) It triggered the spark chambers, the fiducial lights, the event number lights, and the data box.

(2) It advanced the camera.

(3) It generated an 80 msec gate which shut down the system during chamber pulsing and recovery. FIRE was also put in coincidence with the gamma counters (G_1 - G_4) and the beam finger counters (F_1 - F_{16}) to cause the appropriate lights on the data box to light when a coincidence occurred. These counters were not part of the electronics logic in any other way.

4. Spark Chambers and Optics

The lead plate spark chambers and the associated optical system were inherited from a prior experiment. A detailed description can be found in the published results of that experiment.[14] The spark chamber pulsers and discharge gaps have also been described elsewhere.[15]

Each of the four side chambers contained 12 aluminum plates and 42 lead plates of dimension 4 by 5 ft. The back chamber, through which the beam passed, contained 13 aluminum and 48 lead plates 6.5-ft. square. These plates were separated by 5/16-in. thick optically clear Lucite frames. The "lead" plates were actually a laminate of 1/64-in. aluminum, 1/32-in. lead and 1/64-in. aluminum. The use of such very thin lead plates made the detection efficiency for low energy showers quite good (threshold for detection was $E_\gamma \simeq 10$ MeV; probability of detection was $\simeq$ .35, 0.75, 0.90, and 0.95 for E_γ = 20, 40, 60, and 80 MeV respectively). A large number of plates was then necessary to achieve the desired thickness in radiation lengths (7 radiation lengths in the side chambers,

8 radiation lengths in the back chamber).

The first five plates of each chamber were 3/64-in. aluminum. Gamma-rays entering the chambers were unlikely to convert here, the total thickness being only ~ .07 radiation lengths. A particle entering the chambers with a visible track in the first four gaps was thus usually presumed to be charged. This was particularly useful in the back chambers where beam contaminating electrons could cause confusing showers. The spark chambers had high multiple spark efficiency and a track sensitive time of about 1.5 μsec. The chambers were fired when the interesting event was about 600 nsec old.

Figure 10 shows the arrangement of the five spark chambers in space and on the film. Ten field lenses and 46 mirrors comprised the optical system which brought the 10 views to a single Flight Research camera.

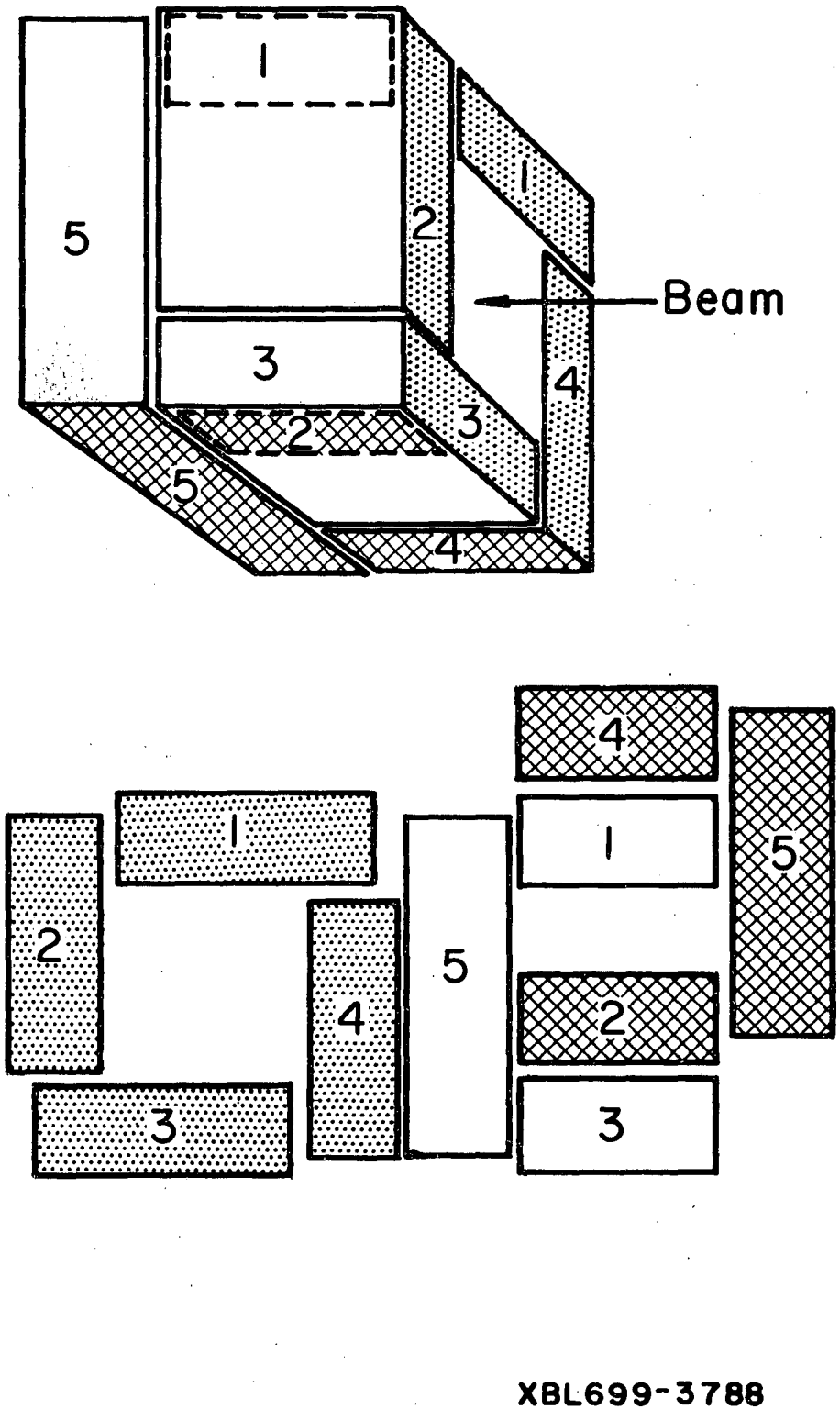

XBL699-3788

Fig. 10. The arrangement of spark chambers in space (top) and the arrangement of the spark chamber views on film (bottom).

III. DATA COLLECTION AND ANALYSIS

A. Introduction

Two experiments to study $\pi^- p \rightarrow$ (neutrals) were conducted at the Bevatron of the Lawrence Berkeley Laboratory. The first was performed during the period October 1968 to April 1969, at π^- momenta of 880, 930, 980, 1030, 1080, and 1130 MeV/c of which the data taken at 1030 MeV/c are included in this thesis. The second took place during the period August 1969 to February 1970, at π^- momenta of 1590, 1790, 1990, 2190, and 2390 MeV/c. Results from all of these momenta are included here.

Data were taken in these experiments both with and without neutron counters. Results from the data taken with neutron counters are reported elsewhere.[10, 11] This paper deals only with the data taken without neutron counters.

These data were used to calculate the cross section for $\pi^- p \rightarrow$ (neutrals), the partial cross sections for $\pi^- p \rightarrow$ n-gamma rays, and for the main purpose here of determining the differential cross section for $\pi^- p \rightarrow \pi^o n$.

The amounts of data taken are shown in Table III. This shows both the amount taken and the amount actually used in this analysis. Data were obtained with the target flask both empty and filled with hydrogen. About 50% of the data taken has been analyzed.

Table III.

Momentum	Target Full # pictures	Target Full # incident beam particles	Target Empty # pictures	Target Empty # incident beam particles
	Data accumulated			
1030	66007	7.585×10^6	2847	3.00×10^6
1590	34688	9.964×10^6	756	1.755×10^6
1790	38466	12.357×10^6	3522	8.932×10^6
1990	45063	15.406×10^6	1845	5.50×10^6
2190	40951	15.269×10^6	1667	5.50×10^6
2390	43273	18.674×10^6	1766	6.50×10^6
Total	268448	79.255×10^6	12403	31.187×10^6
	Data analyzed			
1030	23919	2.777×10^6	2839	2.992×10^6
1590	20755	5.974×10^6	756	1.755×10^6
1790	23822	7.616×10^6	3306	8.384×10^6
1990	23815	8.157×10^6	1840	5.485×10^6
2190	24631	9.237×10^6	201	0.663×10^6
2390	24349	10.571×10^6	1743	6.415×10^6
Total	141291	44.332×10^6	10685	25.694×10^6

B. Film Scanning and Measurement

The reaction $\pi^- p \rightarrow$ (neutrals) almost aways gives a neutron + gamma rays in the final state. These gamma rays were detected by the conversion of gamma rays to electron-positron pairs and the resultant showers in the lead plate spark chambers surrounding the hydrogen target. The pictures taken were scanned and measured by the LBL Group A scanning and measuring staff.

The film was examined by scanners who recorded the number of gamma rays observed in each picture including those detected in the spark chambers as showers and in the gamma counters as indicated by lights on the data box. The coordinates of the first spark of each shower were estimated by recording the grid location of the starting point of each shower. The grid gave a spatial resolution of 3 in. by 2 in. The showers were also paired in the two stereo views of each chamber.

In addition, scanners recorded coordinates for tracks in the spark chambers which were not considered to be valid showers. These included showers with only two sparks, beam tracks (the beam passed through the downstream spark chamber), remnants of old beam tracks, remnants of interactions of the beam with the spark chambers, showers that did not point to the hydrogen target, and showers that were probably fragments of another shower. Also, the same photon which triggered the gamma counters could cause a shower, in which case the shower usually took precedence over the gamma counter.

The film was also measured by SASS,[16] an automatic measuring system using a precision cathode ray tube and photomultiplier linked to a DDP-24 computer. SASS read the data box lights, and digitized the

positions of all the sparks as well as the fiducials in the frame. These data were written on tape with the program FLICKERS.[17]

Using the program DHS,[18] the data from the hand scan was compared with the digitized data from SASS to generate the shower starting point and direction and the number of sparks in the shower. DHS included corrections to take into account distortions due to the mirror-lens system.

Using this system, it was found that shower directions had typical uncertainties of $\pm$ 3 deg and starting point errors of $\pm$ .3 in. The angular error was due primarily to the lateral spread of the shower, while the error in the starting point (or first spark) was due to local optical distortions and ambiguities in selecting the first spark in the specified grid zones.

The geometric reconstruction of the event was then performed by a modified version of the LBL Group A fitting program SIOUX.[19] This program calculated the decay point in the target for the interaction, using the incident beam direction as determined by the finger counters, the shower starting points and directions as determined by DHS, and the known target coordinates. Once the decay point was determined, the shower directions were defined by the target decay point and the first spark of the showers.

The status of each event was stored on a Master List tape, using the program, SCALP.[20] On this tape was recorded the progress of each event as it was scanned, digitized by SASS, measured by DHS and reconstructed by SIOUX. The data box information from FLICKERS and the hand scan information were also recorded. For each event it was also possible to determine the beam momentum, target conditions, and the state of the

rest of the experimental system from SCALP.

The data recorded on the SCALP master list were used in determining the total cross sections for each photon multiplicity. In determining the differential cross section for $\pi^- p \rightarrow n\pi^0$, the output from SIOUX was used. The center-of-mass opening angle of the two gamma rays was calculated and events with opening angles within a specified interval were used to determine the differential cross section.

For each momentum, four rolls of film (~ 12000 events) were completely scanned, and, to save time, another four rolls were scanned for two shower events only. No difference in scanning reliability was detected between these two samples.

C. Scanning Efficiency and Corrections

Three rolls of film (~ 9000 events) were conflict scanned, one roll for each of the following momenta: 1030, 1990, 2390 MeV/c. These rolls were scanned three times and then, in any frames where the three independent scans differed as to the number, location, or quality of the showers, the event was rescanned by the most competent of the scanners. This conflict scan attempted to resolve the discrepency among the initial three scans, and thus define, within the constraints of the scanning criteria, a correct scan.

The largest scanning discrepancies arose from mislabeled grid zones (adjacent ones being confused) and, less often, mislabeled chamber number. The measuring program DHS could locate showers if their grid coordinates were off by no more than one zone. However, when the wrong chamber number was given, the event was lost.

The most important scanning errors were from disagreements on the number of gamma rays present. This error was ~ 6% for two shower events and rose to ~ 30% for six shower events. Errors in the number of triggered gamma counters recorded were inconsequential since the SASS system always picked them up correctly and entered them in the Master List. The significant errors then, occurred when a scanner failed to identify all the showers and consequently the event appeared on the Master List as a (j-1) or (j-2) gamma event. Occasionally, the scanner would report (j + 1) or (j + 2) gammas due to mistaking old beam tracks in the chambers for showers. Because the beam intensity

was rather low, this effect was less than that of missing showers. Thus, given a true j gamma event, there was a probability E_{ij} of it being scanned as an i-gamma event. Calling S_i the recorded number of i-gamma events on the Master List, and T_j the true number of j-gamma events, we see that

$$S_i = E_{ij} T_j$$ (unless otherwise noted, a repeated subscript implies summation over that subscript)

where E_{ij} was obtained from the conflict scan and defined by

$$E_{ij} = \frac{n_{ij}}{\sum_i n_{ij}}$$

where n_{ij} was the number of true j-gamma events (established by the conflict scan) which had been recorded as i-gamma events.

Since the number of events was well defined, $\sum_i S_i = \sum_j T_j$ and for the conflict scan $\sum_i E_{ij} = 1$. The event matrix n_{ij} and the scanning efficiency matrix are shown in Table IV. The efficiency matrices for the three rolls conflict scanned were found to be consistent with one another so the three rolls were considered as a single block of data to generate the efficiency matrix.

The data was corrected for scanning inefficiency by calculating

$$T_i = E^{-1}_{ij} S_j .$$

Table IV.

(a) The event matrix n_{ij}

(Note that each event was scanned three times, thus is counted as three events)

Observed number of gamma rays	True number of gamma rays									
	0	1	2	3	4	5	6	7	8	9
0	320	51	16	4	7	5	4	2	1	1
1	15	1300	322	14	2	1	1	0	0	0
2	4	98	9311	566	70	11	2	0	0	0
3	0	3	249	3242	598	53	8	0	3	0
4	4	0	14	175	5397	495	78	11	2	0
5	4	0	3	8	182	1352	326	46	10	0
6	1	0	0	2	22	105	1148	165	57	5
7	0	0	0	0	1	6	68	262	110	18
8	0	0	0	0	0	0	7	25	233	66
≥ 9	0	0	0	0	0	0	2	2	19	153

(b) Scanning efficiency matrix E

0	.920	.035	.002	.001	.001	.002	.002	.004	.002	.004
1	.043	.895	.033	.004						
2	.012	.068	.939	.141	.011	.001	.001			
3		.002	.025	.808	.095	.026	.005		.007	
4	.012		.001	.044	.860	.244	.047	.021	.005	
5	.012			.002	.029	.667	.198	.090	.023	
6	.003			.001	.004	.052	.698	.322	.131	.021
7						.003	.041	.511	.253	.074
8							.004	.049	.536	.272
≥ 9							.001	.004	.044	.630

D. Gamma Ray Detection Efficiency and Corrections

Once the scanning efficiency matrix had been calculated and applied to the observed vector of gamma events, the resulting vector T_j still did not represent the true number of j-gamma events produced in the target.

Within the scanning criteria, too many gamma rays could be counted in an event. Due to improper scanning an individual gamma ray could be counted as two gamma rays. Also gamma rays from previous interactions could be counted since the spark chambers had a sensitive time of about 2.5 μsec. Beam particles interacting in the spark chamber could produce showers or tracks that would mistakenly be counted as part of the event of interest. Processes that caused more showers to be recorded than were properly part of the event were called feedup.

To empirically estimate the size of the feedup processes, three and four gamma events from the data sample with neutron counters (to measure the neutron direction and velocity) were fit to the hypothesis $\pi^- p \rightarrow n\gamma\gamma$ and the π^0 region studied in the $\gamma\gamma$ opening angle distribution. An enhancement in the three γ events at the π^0 opening angle was found, which also corresponded to the π^0 mass and expected neutron time of flight. No enhancement was found in the four γ events. The number of events above background was estimated to be about 16% of the two shower events. For data taken with neutron counters the beam intensity was 300 to 600 K/second. The data taken without neutron counters had a much lower beam intensity of 20 to 100 K/second. Looking at the three gamma events which appeared to be π^0 events on the scan table, it was seen that typically a third shower of dubious quality was present,

probably caused by a previous event or an old beam particle in the spark chambers. Since this feedup process seemed to be a function of the beam intensity and could logically be assumed to be so, a correspondingly smaller feedup was assumed for the data without neutron counters.

A previous experiment had also studied the feedup process[13] and concluded that there was an extra gamma in 2% of the events and two extra gammas in 0.5% of the events. These values are dependent on both the beam intensity and momentum.

In the present experiment, the only evidence of feedup was for the type which is proportional to beam intensity. It was assumed that the probability of seeing one extra gamma was 4% and of seeing two extra gammas, 1%. Since the size of these effects was rather uncertain, errors of 2% and 1% were assigned to them. In any case the corrections were small and did not significantly alter the data. The correction was applied in the form of a matrix U_{ij} with

$$S_i = U_{ij} t_j$$

where S_i is the observed vector of i gamma events and t_j is the true vector of j gamma events. It is easy to see that the matrix will have the form

$$U_{ij} = \delta_{ij}(1 - u_1 - u_2) + \delta_{i-1,j} u_1 + \delta_{i-2,j} u_2$$

where $u_1 = 0.04$ and $u_2 = 0.01$.

A more serious problem that required larger corrections was that of not detecting all the gamma rays produced in the target, a process called feed-down. Gamma rays could be missed for a variety of reasons.

Gammas could fail to convert in the spark chambers; convert, but not produce enough sparks to be counted as a shower (a loss of low energy gammas); convert in the corners of the spark chambers where the chambers were optically insensitive; or escape upstream where no gamma ray detectors existed.

In order to understand and correct for the effects of the spark chambers in detecting gamma rays, an elaborate Monte Carlo program was constructed.[21] This program contained detailed information on the spark chamber geometry and a complex semi-empirical model for shower production in these spark chambers. When given the dynamics of a specific reaction, this program could then calculate the expected feed-down into all gamma multiplicities. One obvious limitation in this procedure arises from a lack of knowledge of the detailed dynamics of all the reactions involved in this experiment.

In fact, the uncertainty in the production dynamics proved to be a serious obstacle to the direct application of the Monte Carlo results to the calculation of spark chamber feed-down. The main reason for this difficulty was caused by γ-rays escaping the spark chamber array through the upstream hole. This problem was particularly severe for charge-exchange events where a peak in the cross-section in the backwards direction may exist, causing the loss of a γ-ray from relatively large numbers of events. This difficulty is discussed in more detail in the section on two-shower events (Sec. III.F.).

It was believed that the Monte Carlo calculations would have been correct if given the correct dynamics. For this reason the qualitative

properties of feed-down as deduced from the Monte Carlo were relied upon in correcting for feed-down. In particular it was found that the feed-down predictions of the Monte Carlo program for any particular reaction could be accurately described in a very simple way. It was possible to assume for a given reaction that there was a particular probability of detecting a gamma ray, and that this probability did not depend on what happened to the other gamma rays in the event. Thus it was found that for an m gamma event, the probability of detecting n of them could be written as

$$D_{nm} = \frac{m!}{(m-n)!\,n!}\, d_m^n (1 - d_m)^{m-n} \qquad n \leq m$$

$$= 0 \qquad n > m$$

where the average detection probability per gamma, d_m, was determined in principle from fitting this distribution to the Monte Carlo feed-down calculations. This very simple result facilitated the application of the Monte Carlo calculations to the data. While there is no particular reason to expect a binomial distribution to describe the feed-down process in general, it seems reasonable when the detection probability is large, as it was for these spark chambers.

The values of d_m for each γ multiplicity m, and for each momentum were determined by the following semi-empirical procedure. No known process could produce neutral final states with 0, 1, or 5γ's so it was assumed that no such events existed in our sample. The value of d_2 was calculated by the Monte Carlo program, using estimates of the charge exchange differential cross-section extrapolated from lower

energy differential cross-sections. This predicted value of d_2 adequately explained the number of observed 0 and 1 photon events. The values of d_2 defined by the Monte Carlo were typically $d_2 = 0.94 \pm 0.01$. For $m > 2$, the cross sections were not adequately known and the Monte Carlo predictions based on phase space assumptions did not agree with the data. Instead, for $m > 2$ we assumed d_m was independent of m; consequently our model for feed-down contained only two parameters, d_2 and d_3. The value of d_3 was selected by attempting to cause the number of 5-photon events to vanish, and cause the number of 3-photon events to agree with the known cross section of $\pi^- p \rightarrow \omega n$; $\omega \rightarrow \pi^0 \gamma$. This typically gave values of $d_3 = 0.89 \pm 0.02$. Because this procedure was rather arbitrary, the errors assumed for d_m were allowed to be large. The error on the probability of missing a γ-ray, $1-d_m$, was assumed to about 20% of the value itself. The values for feed-down, estimated above, are consistent with those found in a previous experiment, using the same apparatus.[13] The feed-down correction was applied in the form of a matrix D_{ij} with

$$S_i = D_{ij} t_j$$

where S_i is the observed vector of i gamma events and t_j is the vector of true j gamma events before feed-down. D_{ij} is defined above. As before, one corrected the data by inverting the matrix D_{ij} to calculate

$$t_i = D^{-1}_{ij} S_j .$$

E. Total Cross Sections

Since the trigger used to obtain the data discussed here required only that no charged particles leave the target, the data were ideal for calculating the total neutral cross-sections as well as the partial cross-sections for $\pi^- p \rightarrow n + \gamma$'s. It is assumed that the only production processes yielding 2γ's were $\pi^- p \rightarrow n\pi^0$ and $\pi^- p \rightarrow n\eta$, and that the only process giving 4γ's was $\pi^- p \rightarrow n\pi^0\pi^0$. (Recent measurements of the decay mode $\eta \rightarrow \pi^0\gamma\gamma$ had shown it was consistent with zero.[13]) The cross sections could be obtained by simply counting events of a particular gamma ray multiplicity and applying known corrections to them. These corrections are summarized as follows:

(a) Not all the gamma events originated in the hydrogen of the target. Some came from interactions of the beam with the target casing. These were corrected for by taking some data with no hydrogen in the target and subtracting this appropriately normalized sample from the target full data.

(b) The number of observed j-gamma events, n_j, was corrected for scanning efficiency and gamma detection efficiency.

(c) Some valid events were vetoed by the neutral final state requirement because one of the particles associated with the reaction $\pi^- p \rightarrow n+\gamma$'s would scatter and produce a charged particle, thus vetoing the event. The corrections for this case were small and well understood.

In Sec. III-C the scanning efficiency matrix E was calculated. In Sec. III-D the matrix U representing feedup processes adding extra γ-rays to an event was estimated, as well as the feed-down matrix D correcting for spark chamber inefficiencies.

The corrections due to vetoing of valid neutral final state events was denoted by the matrix V. Contributing to V were four factors:

1. Gamma rays from the neutral final state converted in the target, target casing, or anticounters thus vetoing the event. This correction was calculated to be about 2.0% per gamma ray in the final state.

2. The incident π^- which interacted to produce the neutral final state could also produce at least one delta ray energetic enough to leave the target and enter the veto counters, vetoing the event. A Monte Carlo study of this process with the target geometry of this experiment indicated a 1.5% correction was needed.

3. The neutron in the neutral final state elastically scattered with a proton in the target or target system which then escaped and vetoed the event. This was calculated to be about a 1% effect.

4. π^0's produced in the final state decayed 1.16% of the time by the mode $\pi^0 \rightarrow e^+e^-\gamma$. For an even number of γ-rays in the final state it was assumed they came from π^0 decays. For an odd number of γ-rays it was assumed all but one γ-ray was produced by π^0 decays. The slightly different rate for $\eta \rightarrow e^+e^-\gamma$ was neglected.

Including these factors, the matrix V had the following form.

$$V_{ij} = \delta_{ij}(1 - 0.02)^j(1 - 0.015)(1 - 0.01)\ (1 - 0.0116)^{[j/2]}$$

where $[j/2]$ indicates the largest integer $\leq j/2$.

Since the correction matrices did not commute, their order of application must be considered. If t_i was the true number of i gamma events, and 0_m was the observed number of m gamma events

$$0_m = E_{m\ell}U_{\ell k}D_{kj}V_{ji}t_i .$$

A little thought shows that this is the correct order of application. Since we know 0_m and wish t_i we simply invert the equation, yielding

$$t_i = V_{ij}^{-1} D_{jk}^{-1} U_{k\ell}^{-1} E_{\ell m}^{-1} 0_m .$$

Table V shows the number of scanned events and the corrections as they were applied to the data. For each momentum the number of events for each gamma multiplicity was obtained from a scan of four rolls of film from that momentum. They were then corrected for non-hydrogen associated events by normalizing the target empty data to the same number of incident beam particles as the target full data, and subtracting.

The uncertainties indicated in the tables come from the statistical uncertainties in the data sample being considered and in the conflict scan data, the systematic uncertainty in the amount and type of feedup, the systematic uncertainty in the Monte Carlo based feed-down calculations, and the systematic uncertainty in the estimation of the amount of neutral final state vetoing by the target anti system. The propagation of these errors is fully described in Appendix A. The errors after each step of correction to the data are given in the table. The dominant source of error comes from uncertainties in the Monte Carlo generated feed-down matrix.

The cross sections for $\pi^- p \rightarrow n + j\gamma$'s were calculated by setting

$$\sigma_{j\gamma} = - \frac{1}{\ell \rho N \alpha} \log_e \left[1 - \frac{T}{n_0}\right] \cdot \frac{t_j}{T}$$

where

ℓ = the effective length of the hydrogen target (19.75 cm)

ρ = density of boiling liquid hydrogen at 1 atm. ($0.0708\ g/cm^{-3}$)

Table V. Gamma multiplicities

	Total	0γ	1γ	2γ	3γ	4γ	5γ	6γ	7γ	8γ	≥ 9γ
					1030 MeV/c						
# target full events	14815	281	1561	7782	2047	2317	473	313	32	9	0
# target empty events	2839	316	457	1298	334	320	64	35	14	1	0
# hydrogen events	13200	101±20	1301±41	6043±91	1857±46	2135±49	437±22	293±18	24±6	8±3	0
# events after scanning efficiency correction	13200	45±23	1185±50	7116±101	1793±63	2236±61	437±38	369±29	8±14	13±6	-2±1
# events after feed-up correction	13200	48±24	1245±60	7437±179	1562±136	2209±85	351±56	350±36	-10±17	10±8	-2±1
# events after feed-down correction	13200	-4±29	152±169	8137±263	592±252	3450±234	111±132	787±107	-56±52	35±24	-6±3
# events after target veto correction	14566	-5±29	159±177	8791±302	653±278	3926±276	129±153	944±131	-68±64	45±30	-8±3
					1590 MeV/c						
# target full events	11720	190	815	5262	1696	2123	681	668	151	97	37
# target empty events	756	53	89	296	135	105	35	35	30	2	0
# hydrogen events	10267	88±20	644±34	4693±80	1437±47	1921±50	614±28	610±28	130±14	93±10	37±6
# events after scanning efficiency correction	10267	59±22	538±40	4724±88	1375±62	1945±63	589±49	739±47	118±33	133±23	47±10
# events after feed-up correction	10267	62±23	564±44	4948±137	1233±100	1944±75	525±60	735±52	87±38	128±25	41±11
# events after feed-down correction	10267	45±24	-64±118	5276±185	462±194	2843±193	-9±161	1424±175	-37±126	207±82	118±32
# events after target veto correction	11491	47±25	-66±123	5699±210	509±214	3236±228	-10±187	1707±214	-45±154	262±104	152±42
					1790 MeV/c						
# target full events	11842	164	640	4571	1997	2577	841	689	208	119	36
# target empty events	3306	202	351	1254	581	551	197	118	36	11	5
# hydrogen events	10338	72±14	480±27	4000±70	1733±46	2326±52	751±30	635±27	192±15	114±11	34±6
# events after scanning efficiency correction	10338	47±16	383±32	3941±77	1713±62	2348±66	772±52	703±46	225±36	167±24	39±11
# events after feed-up correction	10338	49±17	401±34	4131±118	1625±83	2360±74	696±65	686±52	200±41	158±27	31±11
# events after feed-down correction	10338	39±18	-91±105	4169±156	638±191	3439±218	363±178	1229±187	118±151	335±98	98±36
# events after target veto correction	11655	40±19	-95±109	4504±176	703±211	3913±259	422±206	1474±227	144±185	423±125	126±47
					1990 MeV/c						
# target full events	11911	146	540	4039	2041	2937	976	786	234	140	72
# target empty events	1840	99	159	644	291	373	119	98	31	20	6
# hydrogen events	10542	72±14	422±25	3560±66	1824±47	2659±56	887±32	713±29	211±16	125±12	68±9
# events after scanning efficiency correction	10542	48±16	334±30	3458±74	1797±63	2681±72	933±57	789±51	252±39	157±28	93±15
# events after feed-up correction	10542	51±17	350±32	3625±108	1735±78	2711±79	850±72	766±58	224±44	146±31	85±16
# events after feed-down correction	10542	42±18	-80±95	3590±144	555±203	3883±240	555±194	1315±205	296±170	116±118	269±52
# events after target veto correction	11946	43±18	-83±100	3879±162	611±224	4419±286	645±225	1577±249	362±209	147±150	347±69
					2190 MeV/c						
# target full events	13363	153	446	3937	2234	3609	1244	1044	344	239	113
# target empty events	201	11	12	59	34	41	19	15	8	2	0
# hydrogen events	11853	70±28	356±34	3494±85	1979±64	3301±77	1101±48	931±43	284±28	224±19	113±11
# events after scanning efficiency correction	11853	46±31	263±39	3367±94	1902±85	3348±98	1141±83	1035±76	291±67	305±43	155±19
# events after feed-up correction	11853	48±32	275±41	3533±124	1851±98	3409±108	1038±101	1010±85	253±74	297±46	140±20
# events after feed-down correction	11853	43±33	-97±98	3482±162	408±260	4760±306	614±256	1803±287	82±243	358±154	400±64
# events after target veto correction	13514	44±34	-101±102	3762±180	450±286	5417±364	713±297	2161±348	101±297	452±195	515±85
					2390 MeV/c						
# target full events	12038	173	460	3235	2038	3288	1169	984	326	238	127
# target empty events	1743	69	115	520	306	408	149	101	43	21	11
# hydrogen events	10630	117±15	367±23	2815±60	1791±47	2958±60	1049±36	902±32	291±19	221±16	118±12
# events after scanning efficiency correction	10630	98±17	299±27	2671±67	1738±64	2975±77	1089±64	991±59	314±49	293±38	163±21
# events after feed-up correction	10630	103±18	311±29	2797±90	1708±73	3030±86	1000±80	969±66	279±55	284±41	149±22
# events after feed-down correction	10630	94±18	-7±76	2717±124	465±211	4175±249	619±201	1660±224	182±196	299±144	426±68
# events after target veto correction	12146	96±19	-8±79	2935±138	513±233	4751±298	719±234	1990±274	222±240	378±182	549±90

N = number of particles per mole (6.022×10^{23} atoms mole^{-1})

α = number of moles per gram (0.992 moles/gram)

t_j = number of j photon events after all corrections

n_0 = total number of incident π^-'s = $(1 - c)n_b$

c = the fraction of μ^- and e^- contamination in the beam

n_b = the number of incident beam particles

T = the total number of scattered π^-'s after all corrections

$= n_0 (1 - e^{-\sigma_{Tot} \ell \rho N \alpha})$

where $\sigma_{Tot} = \sigma(\pi^- p \rightarrow \text{anything})$.

The partial and total cross sections are shown in Table VI. Since the total cross section does not depend on the scanning efficiency or the feed-up or feed-down corrections, the error on the total cross section comes mainly from the statistics on the original sample, except for errors in the corrections depending on gamma ray multiplicity in the matrix V.

The errors for the partial cross sections could be written approximately as

$$\langle \delta\sigma_i \delta\sigma_j \rangle = \sigma_i \sigma_j \left[\frac{\langle \delta t_i \delta t_j \rangle}{t_i t_j} + \left(\frac{\delta \ell}{\ell}\right)^2 + \left(\frac{\delta \rho}{\rho}\right)^2 + \left(\frac{\delta n_0}{n_0}\right)^2 \right]$$

where it is assumed $\frac{\delta \ell}{\ell} \simeq 0.01$, $\frac{\delta \rho}{\rho} \simeq 0.01$, and $\delta n_0 / n_0$ comes from the uncertainty (assumed 10%) in the beam contamination measurement. The error in the total cross section could be written as

$$(\delta\sigma_T)^2 = \sigma_T^2 \left[\frac{\sum_{ij} \langle \delta t_i \delta t_j \rangle}{(\sum_i t_i)^2} + \left(\frac{\delta \ell}{\ell}\right)^2 + \left(\frac{\delta \rho}{\rho}\right)^2 + \left(\frac{\delta n_0}{n_0}\right)^2 \right].$$

Table VI. Total and Partial Cross Sections (in mb).

	1030 MeV/c	1590 MeV/c	1790 MeV/c	1990 MeV/c	2190 MeV/c	2390 MeV/c
Total neutral cross-sections	11.71±.30	4.64±.13	4.05±.11	3.77±.10	3.43±.10	2.92±.08
Partial cross-section final state with						
0γ	-.004±.029	.019±.010	.014±.006	.014±.006	.01±.01	.023±.005
1γ	.130±.14	-.027±.05	-.030±.04	-.030±.03	-.03±.03	.002±.02
2γ	7.070±.28	2.300±.10	1.570±.07	1.220±.05	.96±.05	.710±.04
3γ	.530±.22	.210±.09	.240±.07	.190±.07	.11±.07	.120±.06
4γ	3.160±.23	1.310±.10	1.360±.09	1.390±.09	1.38±.09	1.140±.07
5γ	.100±.12	-.004±.08	.150±.07	.200±.07	.18±.08	.170±.06
6γ	.760±.11	.690±.09	.510±.08	.500±.08	.55±.09	.480±.07
7γ	-.060±.05	-.020±.06	.050±.06	.110±.07	.03±.08	.050±.06
8γ	.036±.024	.110±.04	.150±.04	.050±.05	.12±.05	.090±.04
$\geq 9\gamma$	-.006±.003	.060±.02	.040±.02	.110±.02	.13±.02	.130±.02

The calculation of the matrix $\langle \delta t_i \delta t_j \rangle$ is discussed in Appendix A.

A comparison of the total neutrals cross section for this experiment and other experiments is shown in Fig. 11. The data come from Ref. 6-9, 22, 23. In general the agreement is acceptable. One should note that the total cross-sections of Feldman et al.[23] have the strange particle production cross-sections subtracted from the data. The main modes of strange particle production that contribute to neutral final states are

$$\pi^- p \rightarrow \Lambda K^0$$

$$\pi^- p \rightarrow \Sigma^0 K^0$$

$$\pi^- p \rightarrow \Lambda K^0 \pi^0$$

The cross sections for these reactions in this energy range vary from 300 to 170 μb for ΛK^0 final state particles, 200 to 100 μb for $\Sigma^0 K^0$ final state, and 200 to 50μb for the $\Lambda K^0 \pi^0$ final state.[24] Since only about 20% of these final states decay into neutrals, the contribution of strange particle production to our neutral final states sample is about 3 to 4%. This amount has not been subtracted from our data.

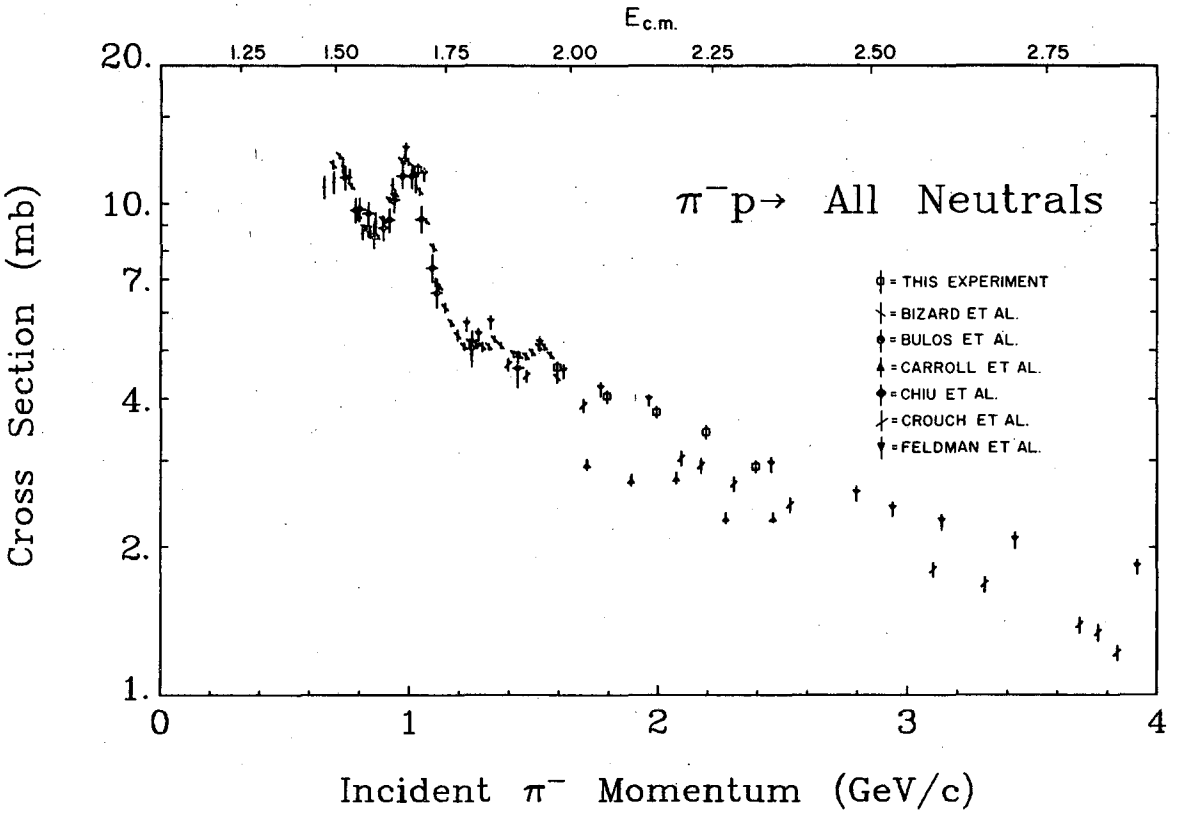

Fig. 11. The total cross section for the reaction $\pi^- p \rightarrow$ all neutrals, measured in this experiment as compared with other experimental results. See Refs. 6-9, 22, 23.

F. Analysis of the Two Shower Sample

At each momentum, eight rolls of film were scanned to produce the two shower event sample. This sample consisted of all events with two showers in the spark chambers, rather than a sample with two photons detected--i.e., in establishing this sample γ-counter information was ignored. From this sample the charge-exchange differential cross-section was derived, as well as the relative cross sections for the final states $\pi^0 n$, ηn. In all future discussion, the sample under consideration is one with the target empty events statistically deleted.

Events were removed from this sample according to the following procedural criteria:

1. Computer system difficulties caused a small number of events to be lost. These events accounted for $\leq 1\%$ of the sample. A fraction of these events was visually examined and no particular topology was detected which could bias the remaining sample.

2. The two showers seen in the chambers were extrapolated back to the target and a fit was made to determine whether the incident π^- direction and the two γ directions were consistent with a single point of interaction within the target volume. Events with $< 1\%$ likelihood of having a single point of interaction were rejected. Between 6 and 12% of the events were rejected by this criterion. These events were presumably caused by measurement errors and misscanning. The center-of-mass γ-γ opening angle distribution of these events is shown in Fig. 12(b) for the sample at 1990 MeV/c. The significance of opening angle distributions is discussed later in this section and in Appendix B. A cut this size in the data sample could potentially bias the results. To check for biases

in the angular distribution of the γ's the confidence level of the fit was plotted for various laboratory angle regions. For all regions, the confidence distribution looked the same, i.e., almost flat except for a spike at probabilities < 1% . Thus it was concluded that γ's from one region of the spark chambers were not being preferentially eliminated over any other region by this cut. As a further check events from this low likelihood group were selected with a c.m. γ-γ opening angle in the region expected from π^0 decays. The γ-γ bisector distribution of this subset of the low confidence level events was plotted and found to be similar to the bisector distribution of the "good" π^0 events. The bisector distribution is interesting because of its close relationship to the angular distribution of π^0 events. We concluded that these rejected events were probably simply poorly measured π^0 events and their exclusion would not bias the subsequent analysis.

3. Events with one or more γ counters triggered were rejected unless either shower in the spark chambers was responsible for the trigger. These events represented feed-down from interactions with more than two γ rays in the final state, for example $\pi^- p \rightarrow \pi^0 \pi^0 n$. A shower in the chambers was defined as responsible for a γ-counter trigger if the shower direction was such that it could have hit the triggered γ-counter. Between 3 and 5% of the events were rejected by this cut--none of them being valid two γ events. These events are shown in Fig. 12(a).

The sample remaining (shown in Figs. 12 and 13) after the deletions outlined above contained still other events in addition to π^0's and η's. In particular some feed-down events still remained. For example, the reactions $\pi^- p \rightarrow n\omega$; $\omega \rightarrow \pi^0 \gamma$ and $\pi^- p \rightarrow n\pi^0\pi^0$ can produce events

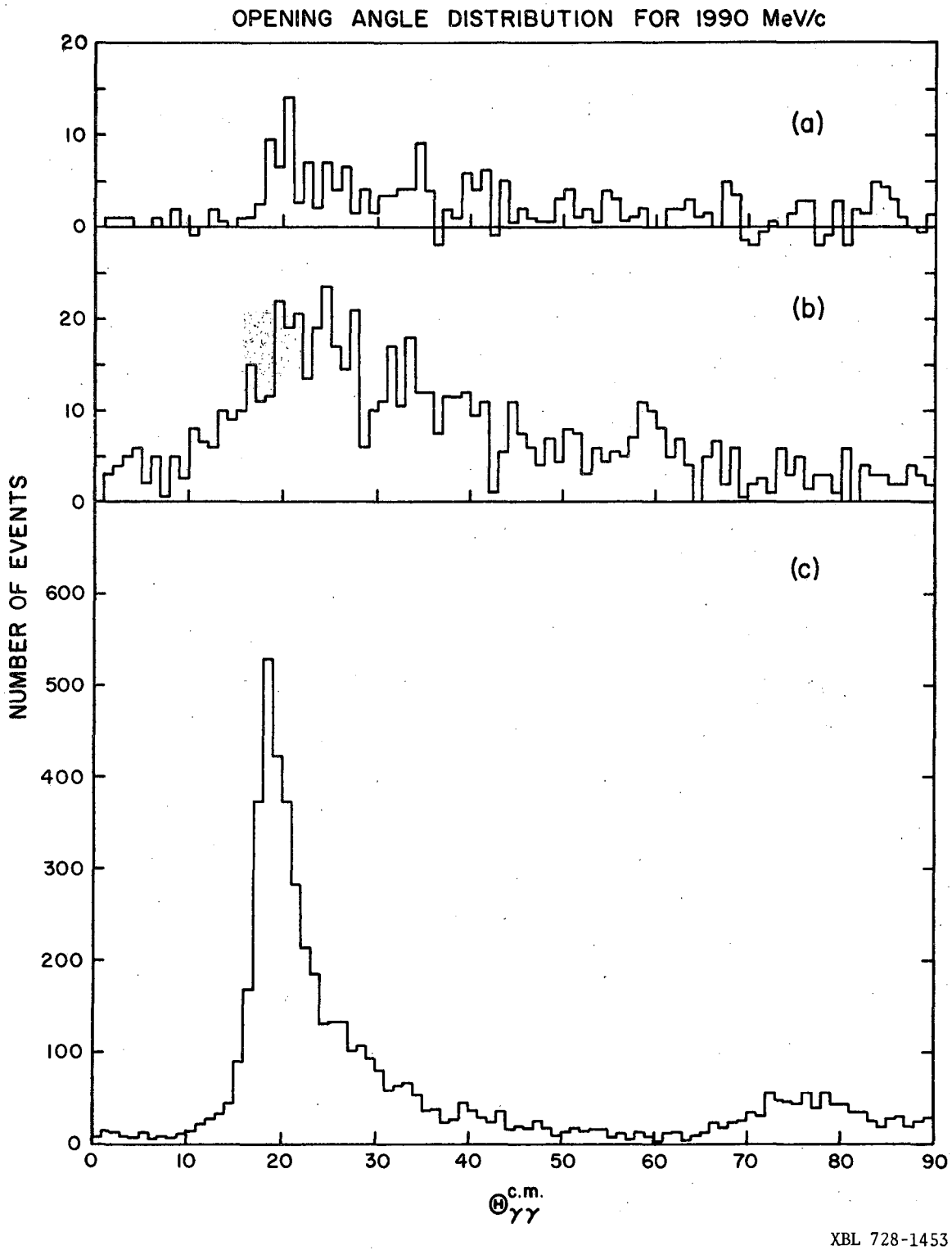

Fig. 12. The center of mass γ-γ opening angle distribution for 1990 MeV/c for two shower events: (a) those events rejected by the γ-counter cut, (b) those events rejected by the decay point cut, (c) the events remaining for analysis.

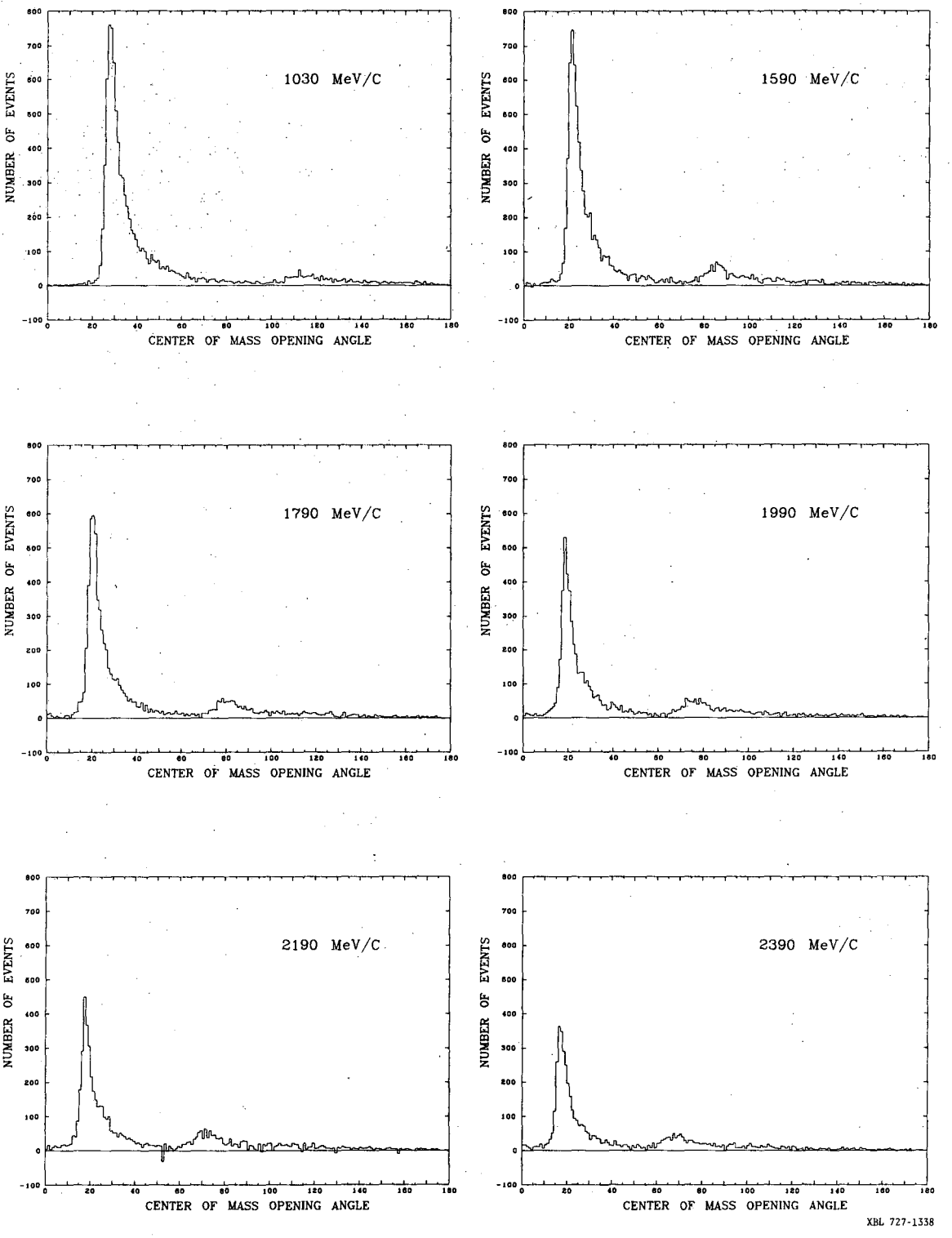

Fig. 13. The events remaining for analysis (after the γ-counter cut and the decay point cut) for the six momenta of this experiment.

in which one or two photons respectively are undetected and thus the two detected photons cause it to be grouped into the two shower sample.

The decay of spinless particles into two γ-rays produces a γ-γ opening angle distribution which is strongly peaked at the minimum opening angle, defined by the particles mass and velocity. The kinematics of this decay are fully discussed in Appendix B. Using this property of the opening angle distribution (seen clearly in the data shown in Figs. 12, 13, 14) one then accepts for further analysis only those events having an opening angle within a specified region. In this experiment the region selected was determined by two considerations: (1) maximizing the number of π^0 events in the region, and (2) minimizing the number of background (non π^0) events in the region.

The fraction of π^0's in the sample within any opening angle region can be calculated from the kinematics. (see Appendix B.) To determine the amount of background however, requires knowledge about the opening angle distribution of these events. This was determined in three different ways.

1. A sample of three shower events was analyzed, and the opening angles for all possible pairings of these γ's were plotted.

2. In a sample of three shower events, the shower with least number of sparks (and thus the one most likely to have remained undetected) was eliminated and the opening angle distribution of the remaining photons was plotted.

3. A Monte-Carlo calculation using the reactions $\pi^- p \rightarrow \pi^0 \pi^0 n$ and $\pi^- p \rightarrow N^*(1238) + \pi^0$; $N^* \rightarrow n\pi^0$ was done. The opening angle distribution of those events in which two photons remained undetected was plotted.

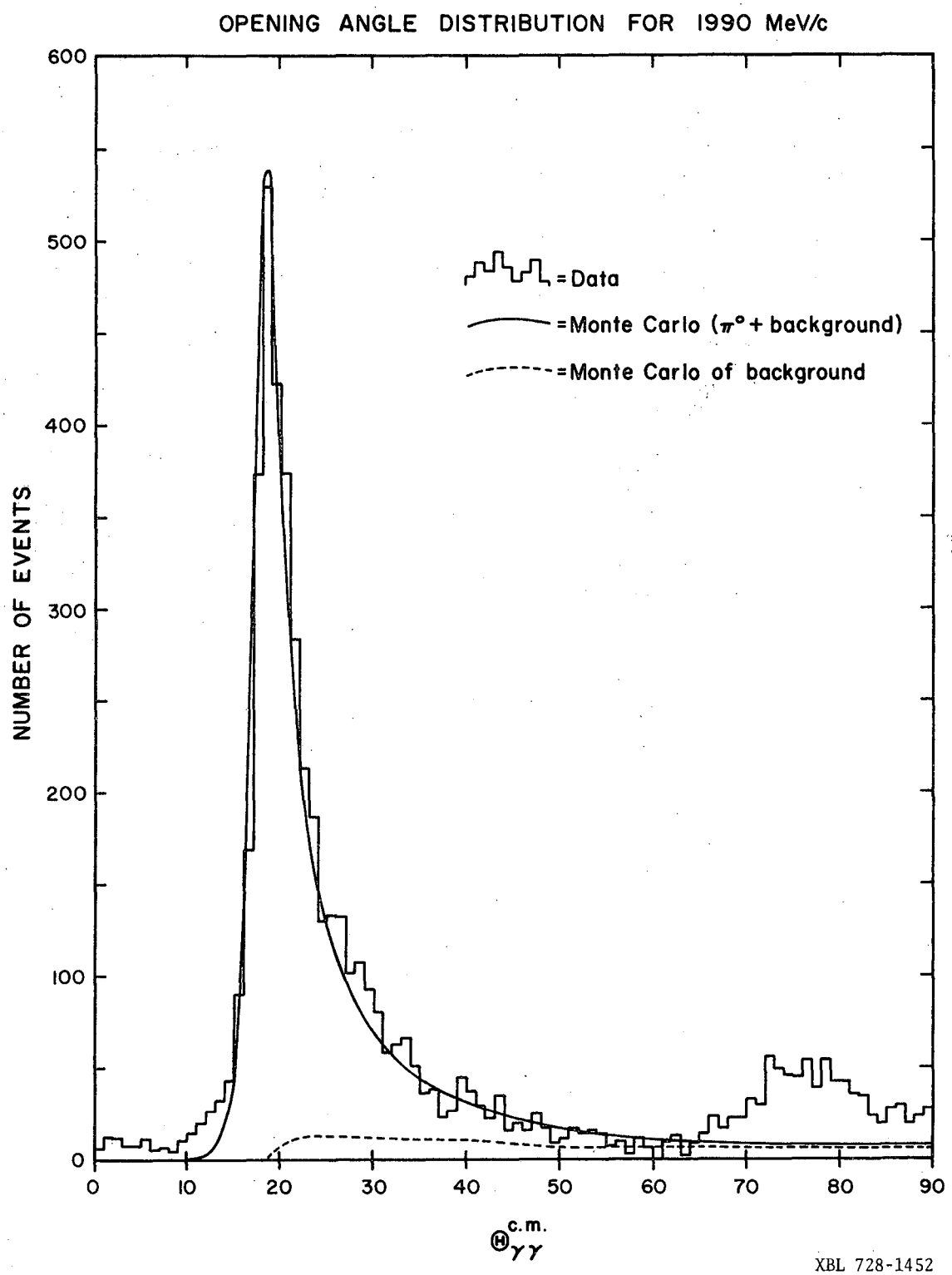

Fig. 14. The center of mass γ-γ opening angle distribution for 1990 MeV/c after cuts, compared with the expected distribution for $\pi^- p \to \pi^0 n$ and $\pi^- p \to \pi^0 \pi^0 n$ (background) as determined by Monte Carlo calculations. The peak at large opening angles is caused by $\pi^- p \to \eta n$; $\eta \to \gamma\gamma$.

It was found that all three procedures yielded similar results. The Monte-Carlo prediction of the opening angle distribution of feed-down events is shown in Fig. 14. A consistency check was made by determining whether the predicted background in addition to the π^0 opening angle distribution normalized to the π^0 peak agreed with the data. This is shown in Fig. 14. Since measurement errors exist, the Monte-Carlo was used to generate the π^0 opening angle distribution rather than simply using the ideal opening angle distribution. A measurement uncertainty of ± 0.3 in. on the position of the first spark of each shower was used in the Monte-Carlo. The normalization of the background events in Fig. 14 was determined from the information obtained in generating the partial cross sections in the previous section (Sec. III-E.) By studying the opening angle distribution of the π^0 events and the background events it was possible to select an opening angle region which contained 80% of the π^0 events and had $\leq 5\%$ background. For the data in Fig. 14 (1990 MeV/c) this region was 15 deg $\leq \theta_{\gamma\gamma} \leq$ 30 deg. The values for other momenta are given in Appendix B, Table B-I.

Having obtained a sample of (almost entirely) π^0 events, the center-of-mass angular distribution of the bisector of the two γ-ray directions was determined. It was assumed that the background events did not alter this distribution other than by changing the normalization. If one has 4π sr detection of γ-rays, it is possible to relate analytically the π^0 event bisector distribution to the π^0 angular distribution itself. This is shown in Appendix B. In our case, the detection efficiency is not 100% over the entire 4π solid angle, so the procedure for determining the π^0 distribution from the bisector distribution required modification. In

practice this modification consisted of using the Monte-Carlo program to relate the bisector and π^0 distributions.

By using a Monte-Carlo calculation, many corrections were applied simultaneously. This calculation corrected for the effects of measurement errors, detection efficiency, opening angle cut, and the difference between ideal π^0 and bisector distributions. The procedure was as follows:

1. An estimate of the π^0 angular distribution was given to the Monte-Carlo program. A flat cross section was assumed at the start.

2. It then generated about 50000 charge exchange events according to this distribution and determined which events had both γ's detected in the spark chambers. This corrected for chamber inefficiencies and the effects of the upstream opening.

3. The position of the first spark of each shower in each event was perturbed. The perturbation was Gaussianly distributed with a standard deviation of 0.3 inches. This simulated the measurement errors.

4. The apparent ("measured") opening angle was calculated and the same opening angle cut was applied to the Monte Carlo data as the real data.

5. The bisector distribution was then generated and divided by the real π^0 distribution to produce a correction function. The data and the Monte Carlo were both binned in intervals of 0.02 in $\cos \theta_{\pi^0}$--thus the angular region had 100 bins. This binning was larger than the resolution of spark chamber measurements.

6. The correction function was then smoothed to reduce the effect of statistics in the Monte-Carlo by averaging each bin with adjacent ones,

except where the efficiency was low. Since the correction function varied slowly with cos θ_{π^0}, this did not bias the distribution.

7. The actual data bisector distribution was divided by this correction function and the resultant estimate of the π^0 distribution was fit with a Legendre polynomial series.

8. The Legendre series was then used as the guess for the π^0 distribution and used in step (1) and the entire process repeated.

The iterative process described above was repeated until the π^0 distribution deduced from the nth iteration was consistent with that of the (n-1)th iteration. Typically this convergence was achieved after four iterations. The correction function, the bisector distribution, and the resultant π^0 distribution are shown in Fig. 15 for 1990 MeV/c. The π^0 angular distributions for all six momenta were obtained in this way.

Note the general features of the Monte Carlo correction function shown in Fig. 15:

1. The overall average is about 80% which simply reflects the fraction of π^0 events contained within the opening angle cut.

2. The slight dip in the forward direction is caused by the opening angle cut. The measurement errors cause the opening angle distribution for forward π^0's to be broadened more than for other π^0 directions. This means a smaller fraction of forward π^0 events will be included in an opening angle cut.

3. The peak around cos $\theta_{\pi^0} = 0.6$ reflects the smearing out of the bisector distribution relative to the true π^0 distribution. Thus when the π^0 distribution has a very low point, the bisector distribution will be more filled in, causing a peak in the ratio of bisector to π^0 distributions.

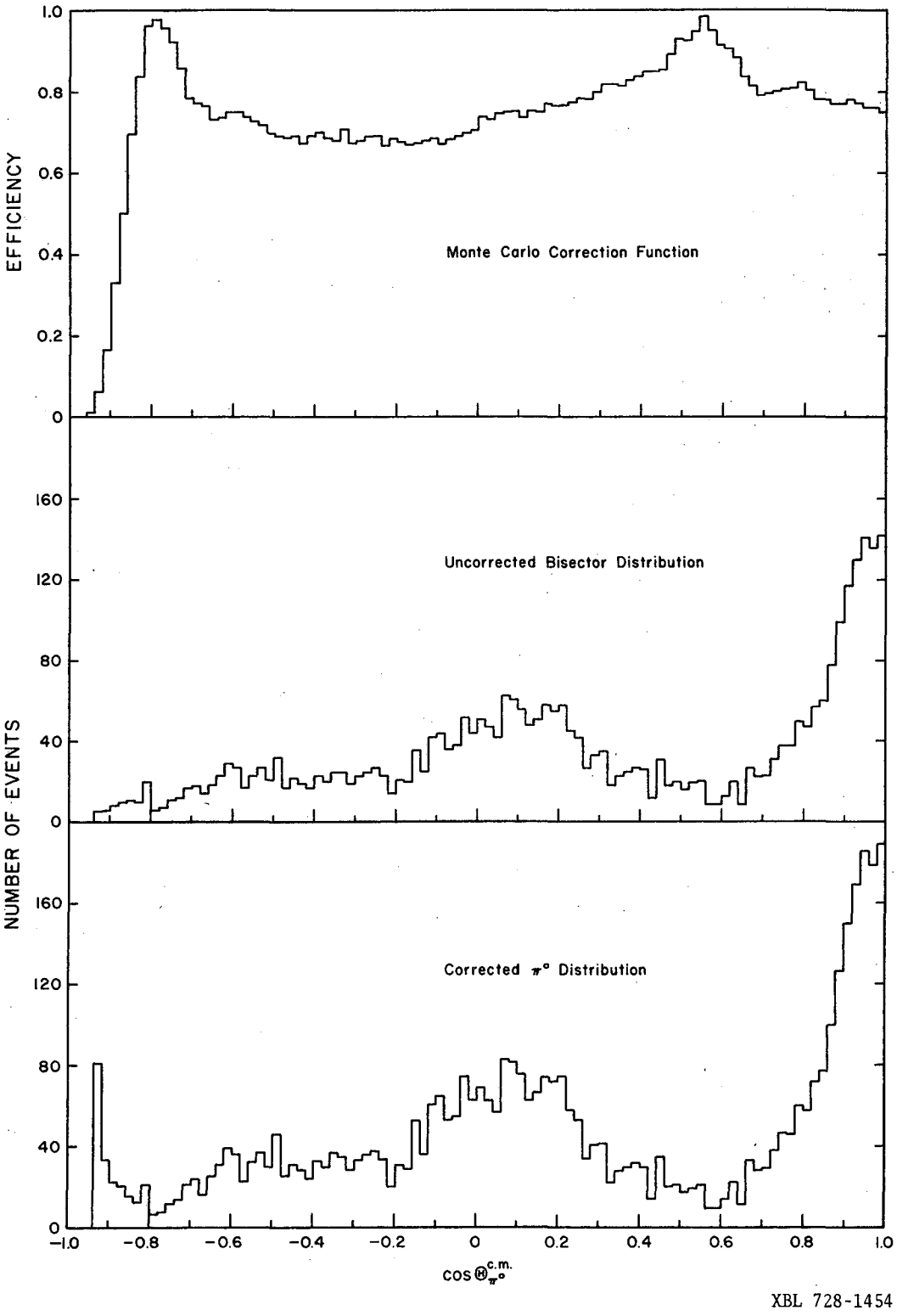

Fig. 15. For 1990 MeV/c, the center of mass Monte Carlo correction function, the uncorrected γ-γ bisector distribution (after the opening angle cut), and the bisector distribution divided by the Monte Carlo correction function to yield the π^0 angular distribution.

The peak at $\cos \theta = -0.8$ has the same origin.

4. The broad decrease around $\cos \theta = -0.4$ is caused by the slightly reduced spark chamber efficiency in the region where the side chambers and back chamber meet. In this region the edges of the chambers can absorb energy from the γ-rays without producing visible sparks.

5. The sharp cut off around $\cos \theta = -0.9$ is caused by the hole in the chambers in the upstream direction. The effects of this cutoff will be discussed more fully in the next section.

IV. RESULTS AND CONCLUSIONS

A. Differential Cross Sections

Once the π^0 angular distributions had been determined, only an overall normalization constant was needed to determine the differential cross section for charge exchange. The following procedure was used to obtain the normalization constant for each momentum.

1. The number of events was corrected to the number of events that would have been produced in an ideal experiment. We can write

$$N_{\pi^0}^{true}(x) = \frac{(1\text{-amount of background in } \theta_{\gamma\gamma} \text{ cut}) \cdot MC(x) \cdot n^{observed}(x)}{(\text{scanning efficiency}) \cdot (\text{feedup correction}) \cdot (\text{target veto correction})}$$

where $x = \cos \theta_{\pi^0}^{c.m.}$

$n^{observed}(x)$ is the observed distribution of events found by plotting against the bisector direction (rather than π^0 direction) and MC(x) is 1/the Monte-Carlo correction function.

The operation n(x) · MC(x) was performed in the last section (Sec. III.F.). The scanning efficiency, feed up correction and target veto correction have been discussed in Secs. III.C,D,E. The amount of background in the $\theta_{\gamma\gamma}$ cut was estimated by determining the fraction of background in the two-γ sample and then assuming the same fraction of background to be within the $\theta_{\gamma\gamma}$ cut at each momentum as that found at 1990 MeV/c where a detailed calculation was made of the background $\theta_{\gamma\gamma}$ distribution. The fraction of background in the 2γ sample was determined with the technique described in Secs. III-C,D,E. This correction (excluding the Monte-Carlo correction) was typically 15%.

2. The true number of charge-exchange events $N_{\pi^0}^{true}(x)$ was normalized according to the number of incident π^-'s at each respective momentum to

yield the differential cross-section by using the procedure described in Sec. III-E. In particular one can write

$$d\sigma/d\Omega(x) = \left\{ -\frac{1}{\ell \rho N \alpha} \log\left(1 - \frac{T}{n_0}\right) \frac{1}{T} \right\} \frac{N_{\pi^0}^{true}(x)}{\Delta\Omega}$$

where $\left\{ \right\}$ has been calculated in Sec. III-E and $\Delta\Omega$ is the bin size for the data sample. Typically $\Delta\Omega = (0.02) \cdot 2\pi$. In practice the bin size was an integral multiple of $(0.02)2\pi$. The multiple was determined by adding together the raw bisector distribution bins $n^{observed}(x)$ until ≥ 25 events were obtained. Thus larger bin widths were created in the backwards direction where the chamber efficiency was low, and wherever the differential cross section was particularly low.

The differential cross-sections for charge-exchange are given in Tables VIIa-c and plotted in Figs. 16a-c. The bin center and half width are given as well as the cross section and statistical error for each respective bin. The errors do not include an overall normalization error of 5%. The data in the most backward regions ($-1 \leq \cos\theta \leq -0.85$) where the chamber efficiency is very low have been omitted because the systematic error in the correction is large, and thus the related data is quite unreliable.

Table VIIa. Differential Cross Section for $\pi^- p \rightarrow \pi^o n$

$\cos \theta_{\pi^o}^{c.m.}$	$d\sigma/d\Omega$(mb/sr)	$\cos \theta_{\pi^o}^{c.m.}$	$d\sigma/d\Omega$(mb/sr)
	1030 MeV/c		1590 MeV/c
.99±.01	2.470±.141	.99±.01	.260±.036
.97±.01	2.247±.133	.97±.01	.293±.035
.95±.01	1.726±.119	.95±.01	.323±.034
.93±.01	1.735±.118	.93±.01	.380±.032
.91±.01	1.379±.105	.91±.01	.379±.036
.89±.01	1.163±.096	.89±.01	.273±.036
.87±.01	.980±.089	.87±.01	.305±.031
.85±.01	.983±.084	.85±.01	.264±.031
.83±.01	.664±.074	.83±.01	.272±.032
.81±.01	.551±.066	.81±.01	.245±.033
.79±.01	.568±.065	.79±.01	.234±.025
.77±.01	.451±.058	.77±.01	.177±.027
.75±.01	.358±.051	.75±.01	.146±.020
.73±.01	.248±.044	.73±.01	.139±.025
.71±.01	.246±.044	.71±.01	.177±.021
.69±.01	.239±.044	.69±.01	.150±.019
.67±.01	.228±.038	.67±.01	.096±.018
.65±.01	.195±.036	.65±.01	.067±.019
.63±.01	.144±.030	.63±.01	.065±.012
.61±.01	.181±.034	.60±.02	.041±.014
.59±.01	.209±.036	.56±.02	.053±.008
.57±.01	.272±.042	.52±.02	.059±.010
.55±.01	.173±.038	.48±.02	.047±.014
.53±.01	.182±.039	.45±.01	.100±.016
.51±.01	.281±.045	.43±.01	.068±.017
.49±.01	.263±.043	.41±.01	.066±.013
.47±.01	.183±.046	.39±.01	.156±.020
.45±.01	.225±.044	.37±.01	.078±.022
.43±.01	.318±.053	.35±.01	.121±.018
.41±.01	.216±.043	.33±.01	.121±.027
.39±.01	.240±.053	.31±.01	.130±.019
.37±.01	.258±.048	.29±.01	.163±.021
.35±.01	.352±.057	.27±.01	.194±.023
.33±.01	.263±.052	.25±.01	.133±.026
.31±.01	.338±.054	.23±.01	.141±.023
.29±.01	.318±.058	.21±.01	.162±.021
.27±.01	.380±.064	.19±.01	.142±.027
.25±.01	.441±.063	.17±.01	.180±.026
.23±.01	.321±.056	.15±.01	.129±.028
.21±.01	.330±.062	.13±.01	.232±.026
.19±.01	.415±.062	.11±.01	.202±.024
.17±.01	.388±.064	.09±.01	.180±.026
.15±.01	.337±.060	.07±.01	.159±.025
.13±.01	.398±.067	.05±.01	.214±.025
.11±.01	.319±.059	.03±.01	.207±.025
.09±.01	.370±.058	.01±.01	.227±.027
.07±.01	.333±.057	-.01±.01	.184±.031
.05±.01	.277±.053	-.03±.01	.124±.029
.02±.02	.209±.034	-.05±.01	.151±.027
-.01±.01	.229±.049	-.07±.01	.175±.024
-.03±.01	.198±.041	-.09±.01	.220±.027
-.06±.02	.156±.025	-.11±.01	.221±.026
-.10±.02	.111±.021	-.13±.01	.158±.037
-.14±.02	.100±.019	-.15±.01	.154±.025
-.19±.03	.054±.012	-.17±.01	.141±.024
-.24±.02	.075±.015	-.19±.01	.192±.027
-.28±.02	.088±.018	-.21±.01	.185±.024
-.31±.01	.142±.029	-.23±.01	.163±.022
-.34±.02	.130±.023	-.25±.01	.150±.026
-.37±.01	.188±.038	-.27±.01	.155±.030
-.39±.01	.226±.042	-.29±.01	.151±.030
-.41±.01	.202±.042	-.31±.01	.156±.030
-.43±.01	.367±.053	-.33±.01	.130±.025
-.45±.01	.374±.054	-.35±.01	.188±.024
-.47±.01	.514±.063	-.37±.01	.159±.022
-.49±.01	.504±.066	-.39±.01	.135±.024
-.51±.01	.560±.068	-.41±.01	.141±.027
-.53±.01	.579±.072	-.43±.01	.170±.022
-.55±.01	.809±.079	-.45±.01	.166±.022
-.57±.01	.841±.086	-.47±.01	.244±.030
-.59±.01	.945±.090	-.49±.01	.215±.029
-.61±.01	.797±.083	-.51±.01	.189±.030
-.63±.01	1.135±.097	-.53±.01	.211±.031
-.65±.01	1.182±.101	-.55±.01	.190±.033
-.67±.01	1.199±.099	-.57±.01	.187±.032
-.69±.01	1.202±.100	-.59±.01	.197±.027
-.71±.01	1.206±.105	-.61±.01	.175±.026
-.73±.01	1.341±.114	-.63±.01	.210±.025
-.75±.01	1.230±.117	-.65±.01	.180±.029
-.77±.01	1.547±.135	-.67±.01	.162±.027
-.79±.01	1.672±.156	-.69±.01	.135±.019
-.81±.01	1.577±.168	-.71±.01	.144±.025
-.83±.01	1.365±.173	-.73±.01	.123±.024
-.85±.01	1.249±.196	-.75±.01	.130±.018
		-.77±.01	.125±.022
		-.79±.01	.115±.023
		-.81±.01	.109±.024
		-.83±.01	.132±.024
		-.85±.01	.158±.030

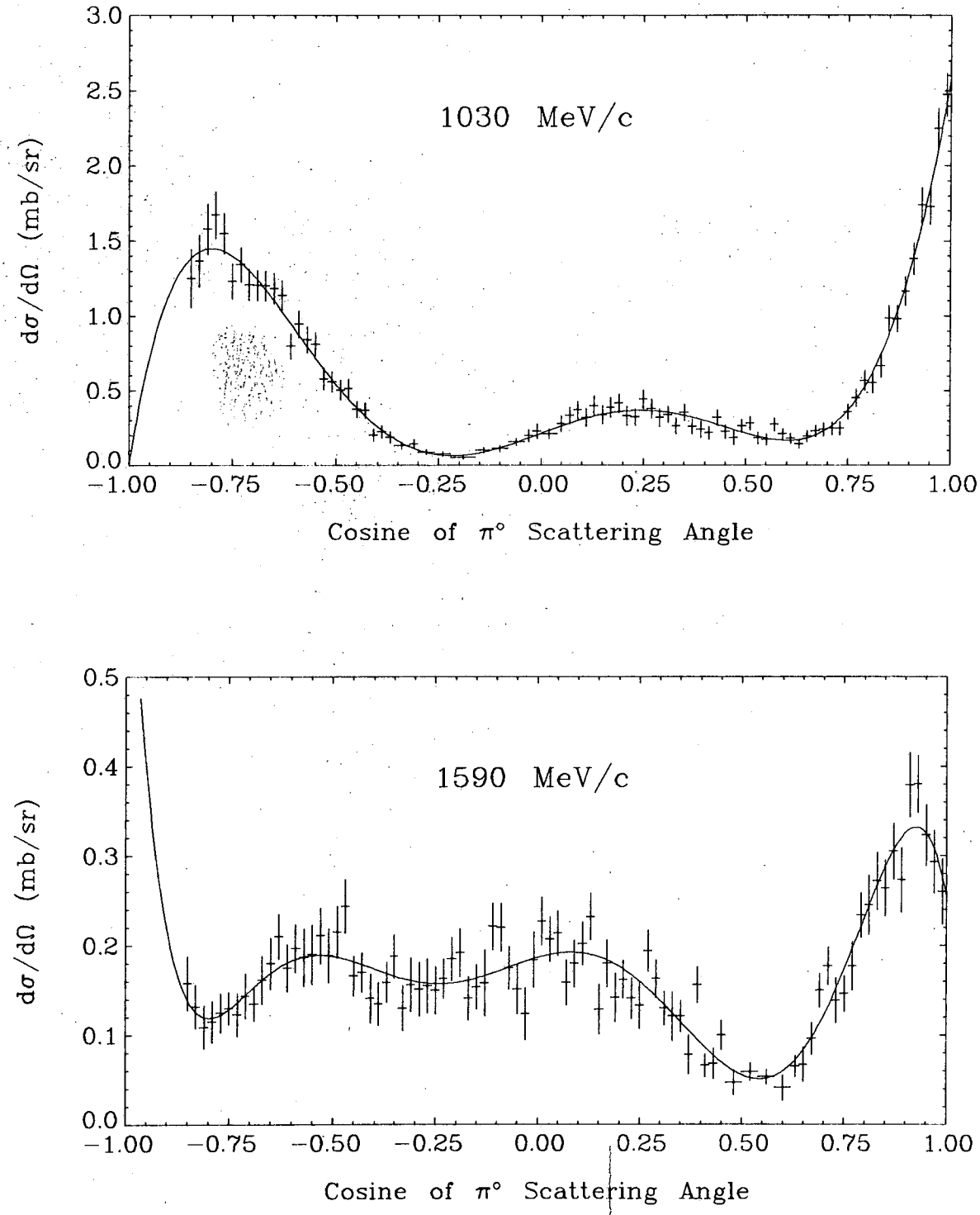

Fig. 16a. Differential cross section for the reaction $\pi^- p \to \pi^o n$ measured in this experiment. The curves are the Legendre fits whose coefficients are listed in Table VIII.

Table VIIb. Differential Cross Section for $\pi^- p \to \pi^o n$

$\cos \theta_{\pi^o}^{c.m.}$	$d\sigma/d\Omega$(mb/sr)	$\cos \theta_{\pi^o}^{c.m.}$	$d\sigma/d\Omega$(mb/sr)
	1790 MeV/c		1990 MeV/c
.99±.01	.450±.035	.99±.01	.323±.030
.97±.01	.381±.033	.97±.01	.306±.028
.95±.01	.360±.032	.95±.01	.319±.028
.93±.01	.380±.032	.93±.01	.289±.029
.91±.01	.293±.028	.91±.01	.256±.026
.89±.01	.264±.027	.89±.01	.218±.025
.87±.01	.261±.027	.87±.01	.172±.022
.85±.01	.195±.024	.85±.01	.132±.021
.83±.01	.182±.022	.83±.01	.124±.020
.81±.01	.163±.021	.81±.01	.099±.018
.79±.01	.134±.019	.79±.01	.104±.016
.77±.01	.126±.019	.77±.01	.079±.015
.75±.01	.115±.017	.75±.01	.080±.015
.73±.01	.085±.015	.73±.01	.065±.015
.71±.01	.085±.014	.70±.02	.049±.009
.69±.01	.054±.012	.66±.02	.037±.007
.66±.02	.040±.007	.61±.03	.026±.005
.61±.03	.026±.005	.56±.02	.026±.005
.56±.02	.028±.006	.52±.02	.032±.006
.51±.03	.019±.004	.48±.02	.035±.007
.46±.02	.037±.007	.44±.02	.043±.007
.43±.01	.057±.012	.41±.01	.052±.012
.41±.01	.056±.012	.39±.01	.054±.011
.38±.02	.054±.009	.37±.01	.052±.013
.35±.01	.061±.012	.34±.02	.043±.009
.33±.01	.092±.017	.31±.01	.072±.014
.31±.01	.116±.017	.29±.01	.070±.014
.29±.01	.079±.014	.27±.01	.058±.015
.27±.01	.134±.018	.25±.01	.091±.018
.25±.01	.122±.018	.23±.01	.098±.017
.23±.01	.142±.019	.21±.01	.128±.017
.21±.01	.129±.018	.19±.01	.123±.018
.19±.01	.122±.019	.17±.01	.128±.017
.17±.01	.099±.017	.15±.01	.114±.017
.15±.01	.146±.020	.13±.01	.108±.017
.13±.01	.148±.020	.11±.01	.130±.018
.11±.01	.129±.019	.09±.01	.139±.019
.09±.01	.161±.021	.07±.01	.142±.019
.07±.01	.159±.021	.05±.01	.097±.018
.05±.01	.107±.019	.03±.01	.108±.016
.03±.01	.124±.019	.01±.01	.118±.017
.01±.01	.152±.021	-.01±.01	.107±.017
-.01±.01	.140±.019	-.03±.01	.127±.020
-.03±.01	.134±.020	-.05±.01	.094±.015
-.05±.01	.160±.022	-.07±.01	.090±.016
-.07±.01	.131±.022	-.09±.01	.111±.019
-.09±.01	.112±.019	-.12±.02	.083±.012
-.11±.01	.121±.020	-.15±.01	.090±.017
-.13±.01	.123±.019	-.18±.02	.051±.010
-.15±.01	.092±.017	-.22±.02	.046±.010
-.17±.01	.116±.019	-.26±.02	.063±.009
-.19±.01	.123±.020	-.30±.02	.052±.009
-.21±.01	.126±.020	-.33±.01	.060±.012
-.24±.02	.100±.013	-.35±.01	.063±.013
-.27±.01	.119±.020	-.38±.02	.052±.009
-.29±.01	.081±.017	-.42±.02	.045±.009
-.31±.01	.108±.017	-.46±.02	.048±.009
-.33±.01	.114±.018	-.50±.02	.065±.010
-.35±.01	.108±.018	-.53±.01	.063±.013
-.37±.01	.099±.016	-.56±.02	.046±.008
-.39±.01	.115±.018	-.59±.01	.061±.013
-.41±.01	.072±.015	-.62±.02	.059±.009
-.43±.01	.085±.017	-.66±.02	.036±.007
-.45±.01	.072±.015	-.70±.02	.038±.007
-.47±.01	.118±.018	-.76±.04	.016±.004
-.49±.01	.108±.017	-.83±.03	.027±.005
-.51±.01	.103±.017		
-.53±.01	.063±.015		
-.55±.01	.080±.016		
-.57±.01	.082±.016		
-.59±.01	.089±.017		
-.61±.01	.132±.020		
-.63±.01	.095±.016		
-.65±.01	.068±.015		
-.67±.01	.099±.015		
-.69±.01	.074±.015		
-.72±.02	.063±.010		
-.76±.02	.053±.009		
-.80±.02	.060±.010		

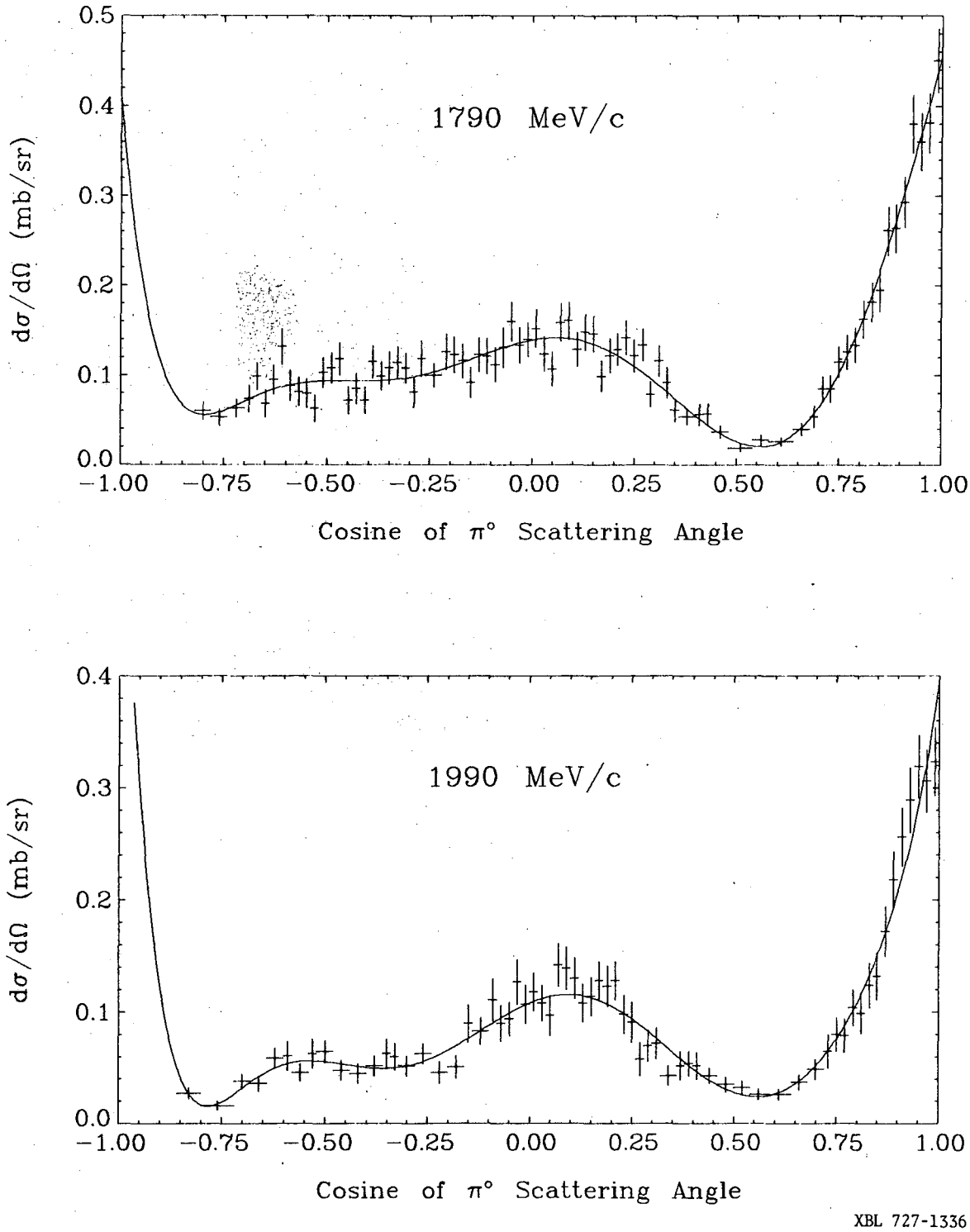

Fig. 16b. Differential cross section for the reaction $\pi^- p \to \pi^0 n$ measured in this experiment. The curves are the Legendre fits whose coefficients are listed in Table VIII.

Table VIIc. Differential Cross Section for $\pi^- p \rightarrow \pi^o n$

$\cos \theta_{\pi^o}^{c.m.}$	$d\sigma/d\Omega$(mb/sr)	$\cos \theta_{\pi^o}^{c.m.}$	$d\sigma/d\Omega$(mb/sr)
	2190 MeV/c		2390 MeV/c
.99±.01	.236±.044	.99±.01	.127±.017
.97±.01	.216±.043	.97±.01	.176±.020
.95±.01	.220±.034	.95±.01	.169±.019
.93±.01	.207±.033	.93±.01	.177±.020
.91±.01	.144±.031	.91±.01	.172±.018
.89±.01	.107±.029	.89±.01	.119±.017
.87±.01	.095±.013	.87±.01	.109±.015
.85±.01	.119±.015	.85±.01	.081±.014
.83±.01	.074±.029	.83±.01	.086±.013
.81±.01	.066±.011	.81±.01	.047±.011
.79±.01	.067±.011	.79±.01	.043±.009
.77±.01	.067±.011	.77±.01	.058±.010
.75±.01	.065±.011	.74±.02	.037±.006
.73±.01	.051±.010	.69±.03	.020±.004
.71±.01	.047±.009	.64±.02	.024±.004
.67±.03	.021±.009	.60±.02	.028±.005
.62±.02	.038±.006	.56±.02	.024±.005
.57±.03	.024±.009	.53±.01	.045±.010
.52±.02	.039±.006	.51±.01	.039±.008
.48±.02	.049±.007	.49±.01	.061±.011
.44±.02	.049±.007	.47±.01	.063±.010
.41±.01	.050±.009	.45±.01	.056±.010
.39±.01	.057±.010	.42±.02	.048±.007
.37±.01	.063±.011	.39±.01	.041±.011
.35±.01	.059±.010	.37±.01	.051±.010
.33±.01	.090±.013	.35±.01	.047±.009
.31±.01	.065±.011	.33±.01	.042±.009
.29±.01	.094±.013	.31±.01	.056±.010
.27±.01	.084±.013	.29±.01	.067±.011
.24±.02	.063±.015	.27±.01	.048±.009
.21±.01	.088±.013	.24±.02	.038±.006
.19±.01	.089±.013	.21±.01	.070±.012
.17±.01	.102±.014	.19±.01	.044±.010
.15±.01	.066±.028	.17±.01	.079±.013
.13±.01	.055±.029	.15±.01	.057±.010
.11±.01	.079±.031	.13±.01	.054±.010
.09±.01	.071±.030	.11±.01	.070±.012
.07±.01	.082±.013	.09±.01	.058±.010
.05±.01	.062±.011	.07±.01	.046±.010
.03±.01	.076±.012	.04±.02	.039±.007
.01±.01	.073±.012	.01±.01	.043±.010
-.01±.01	.098±.014	-.02±.02	.032±.006
-.03±.01	.060±.011	-.06±.02	.035±.006
-.05±.01	.085±.013	-.10±.02	.022±.006
-.07±.01	.072±.012	-.15±.03	.016±.004
-.10±.02	.049±.007	-.21±.03	.015±.004
-.13±.01	.054±.011	-.29±.05	.009±.003
-.16±.02	.055±.008	-.38±.04	.016±.003
-.20±.03	.046±.007	-.44±.02	.026±.005
-.24±.02	.042±.007	-.48±.02	.029±.006
-.28±.02	.030±.006	-.52±.02	.031±.006
-.32±.02	.029±.006	-.56±.02	.029±.005
-.36±.02	.033±.006	-.61±.03	.020±.005
-.40±.02	.041±.007	-.66±.02	.020±.004
-.44±.02	.028±.005	-.71±.03	.014±.003
-.48±.02	.029±.006	-.77±.03	.014±.003
-.52±.02	.043±.007	-.82±.02	.028±.005
-.56±.02	.028±.005	-.86±.02	.038±.007
-.60±.02	.030±.005		
-.64±.02	.028±.005		
-.68±.02	.032±.005		
-.73±.03	.020±.003		
-.80±.04	.011±.006		
-.86±.02	.041±.007		

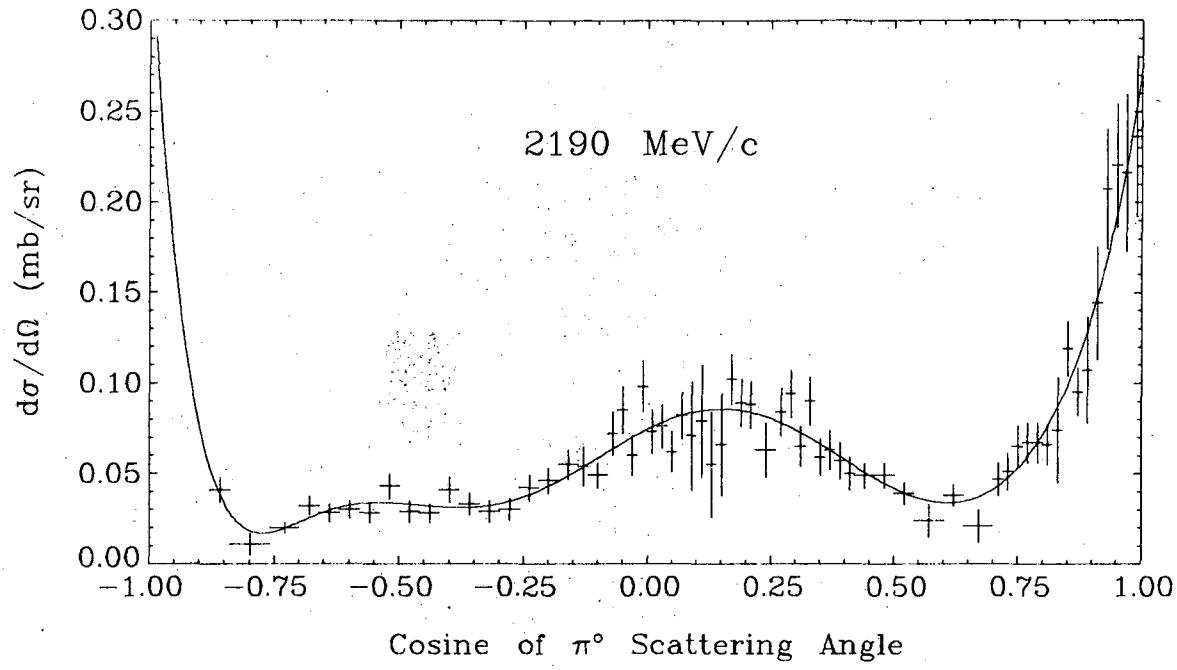

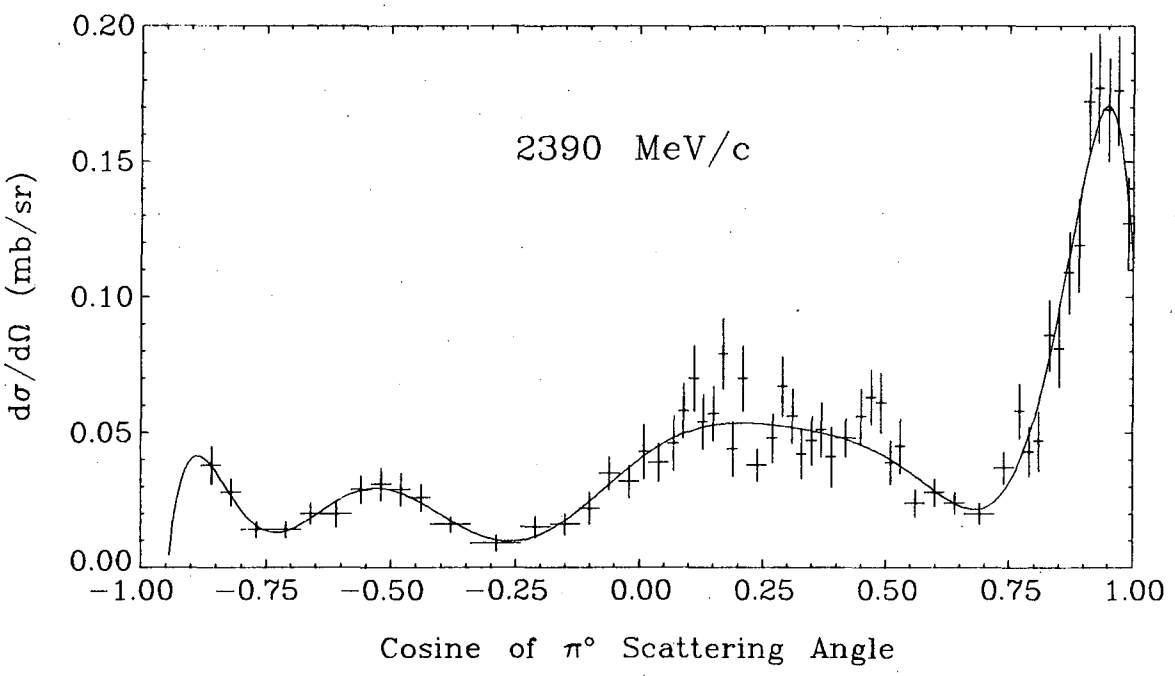

XBL 727-1337

Table 16c. Differential cross section for the reaction $\pi^- p \to \pi^0 n$ measured in this experiment. The curves are the Legendre fits whose coefficients are listed in Table VIII.

B. Legendre Polynomial Fits

The differential cross sections derived in the last section were fitted to the Legendre series

$$d\sigma/d\Omega(\cos\theta) = \sum_j c_j P_j(\cos\theta)$$

where $P_j(\cos\theta)$ are the Legendre polynomials, and $\cos\theta$ is the c. m. scattering angle. Since the coefficients c_j are unique functions of partial wave amplitudes,[25-26] this expansion can in principle have interesting physical significance.

The data given in Table VIIa-c were fitted to this series using the method of least squares. The series was terminated at an even order for each momentum. The order selected was unambiguously determined by picking the lowest even order that gave a reasonable confidence level to the fit. The Legendre coefficients, the number of data points fit, the confidence level of the fit, and the number of experimental events used in the fit are shown in Table VIII. The fits are shown with the data in Figs. 16a-c. Because the differential cross-section was not determined in the backward direction, the fit to the data was almost unconstrained in that area and therefore the values of the Legendre coefficients were highly correlative. For this reason the formal (diagonal) errors for the Legendre coefficients have been deliberately omitted from Table VIII. Also, of course, the fitted curve in the figures is not reliable in the region $\cos\theta \leq -0.85$.

The error matrix for the Legendre coefficients was diagonalized and its eigenvectors determined. It was found that one eigenvector had a large uncertainty and that the others had quite small errors. The eigenvector with the large uncertainty corresponded to a combination of

Table VIII. Legendre coefficients for $\pi^- p \to \pi^o n$ differential cross section

$$d\sigma/d\Omega(x) = \sum_j c_j P_j(x) \text{ (mb/sr)}$$

	1030 MeV/c	1590 MeV/c	1790 MeV/c	1990 MeV/c	2190 MeV/c	2390 MeV/c
c_o	.560	.1773	.1164	.0918	.0652	.0381
c_1	-.113	-.0229	.0300	.0124	.0206	.0437
c_2	.853	.1049	.0864	.1001	.0542	.0180
c_3	.437	.0259	.0723	-.0073	-.0096	.0386
c_4	.061	.1696	.1788	.1971	.1161	.0191
c_5	.955	-.0864	-.0032	-.0375	.0001	.0602
c_6	-.186	.0251	.0241	.0727	.0449	-.0220
c_7		-.1605	-.0765	-.0904	-.0466	-.0036
c_8		.0229	.0249	.0559	.0254	-.0498
c_9						.0127
c_{10}						-.0428
Number of data points	85	90	80	67	65	59
Confidence of fit	.77	.14	.64	.57	.75	.37
No. of experimental events	6500	5300	4400	3300	2900	2500

For a comment on errors, see section IV B.

Legendre polynomials with a small value over most of the cos θ interval and a large value in the backwards direction. This was consistent with the data distribution, i. e., accurate data over most of the cos θ interval and very poor data in the backwards direction. A future analysis of the one-shower events should significantly improve the data in the backwards region.

Since the fitted value of the cross section in the backwards direction is so uncertain, the integral of the differentiated cross-section is not a reliable estimate of the total charge-exchange cross-section. Thus the expression

$$\sigma_{tot}^{cex} = 4\pi c_0$$

is unreliable and the total cross section comes from a further analysis of the partial cross-sections (Sec. IV-C).

C. Total Cross Sections for $\pi^- p \rightarrow \pi^0 n, \eta n$

Since the differential cross-section was not measured in the backwards direction, the total cross section was derived from the partial cross sections. This was essentially a statistical analysis based on the number of the 0, 1 and 2 shower events. It was assumed that the 2γ cross section was divided between the final states $\pi^0 n$ and ηn. The 2γ cross-section comes from Sec. III-E where the 0 and 1 shower events have been included via the feed-down process. It was assumed the feeddown for η's was the same as for π^0's.

The two-shower sample was used to find the relative amounts of π^0 and η production. The number of η events in this sample was determined by estimating the number of events in the peak in the opening angle distribution caused by the decay of $\eta \rightarrow \gamma\gamma$. This peak can be seen in Figs. 13 and 14. The largest source of error in the estimate of the number of η events was due to background in this opening angle region. To minimize this uncertainty, the amount of background was substantially reduced by requiring that each shower have at least 15 sparks. Since the number of sparks in a shower is proportional to its energy, this gave excellent separation of the η's from background. A check was made to ensure that no η's were removed by this cut. The number of π^0 events was estimated by counting the events within a narrow opening angle cut such that only π^0 events would be included, and then calculating the total number of π^0 events without the cut.

This procedure was checked for consistency by varying the opening angle cut on the π^0 peak. The amount of background present was derived by subtracting the π^0 and η events from the two shower total. This

number was consistent with that expected from the feed-down of the 3- and 4-γ events calculated using the techniques described in Sec. III-C, D, E.

The strange particle production contribution to the two-γ cross section was ignored here. It corresponds to approximately one standard deviation effect on the cross sections. The $\pi^0 n$ and ηn total cross-sections are shown in Table IX. The $\pi^0 n$ total cross sections are compared with other experiments[6-9,27] in Fig. 17.

Table IX. Cross sections

p_π(MeV/c)	$\pi^- p \to \pi^o n$ $d\sigma/d\Omega(0^o)$(mb/sr)	cross section (mb) $\pi^- p \to \pi^o n$	cross section (mb)* $\pi^- p \to \eta n \quad \eta \to \gamma\gamma$
1030	2.57±.08	6.65±.26	.419±.033
1590	.255±.032	2.03±.10	.272±.020
1790	.453±.030	1.36±.06	.202±.015
1990	.395±.025	1.01±.05	.215±.016
2190	.270±.032	.79±.04	.170±.013
2390	.112±.020	.58±.03	.127±.010

*errors include a 5% uncertainty due to background subtraction

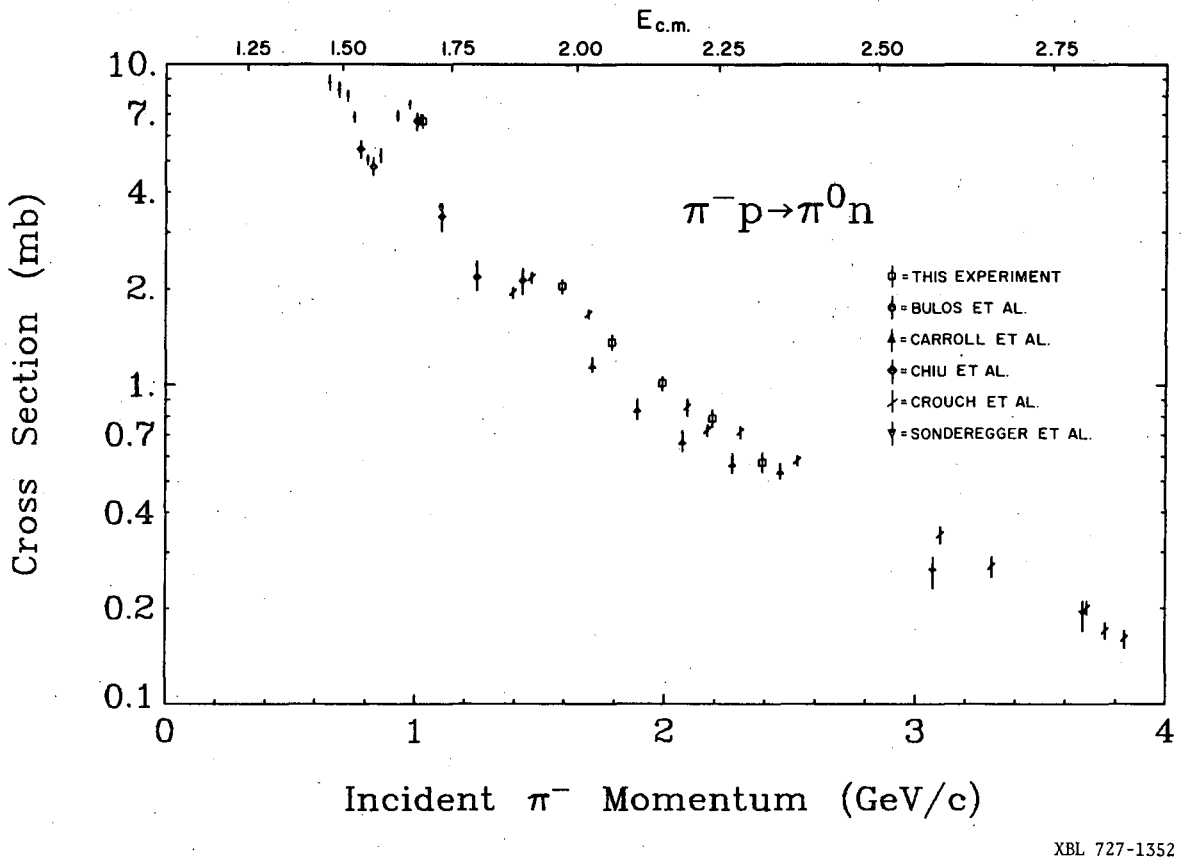

Fig. 17. The total cross sections for the reaction $\pi^- p \to \pi^0 n$ measured in this experiment as compared with other experimental results. See Refs. 6-9, 27.

D. Comparison with other Experiments

The only experiments in this energy range are Refs. 6-9. It is usual to compare Legendre coefficients of the fits to the differential cross-section, plotting each coefficient as a function of the beam momentum. Since in this experiment, a unique set of Legendre coefficients was not obtained (Sec. IV.B) it was not possible to make this comparison. Cross sections at momenta near those of this experiment have been selected for comparison from Refs. 6-9. Except for the data near 1030 MeV/c all the comparison data have rather large errors due to the small statistical sample which the Legendre coefficients are based on.

The data of Chiu[8] at 1005 MeV/c and Bulos[7] and 1024 MeV/c are quite similar to this experiment at 1030 MeV/c. The greatest disagreements occur around $\cos\theta = -0.8$ where this experiment is about 20% higher than either of the above. In the forward direction all three differ from each other by about 15%. The three agree on the general shape.

Neither Refs. 6 or 9 have data near 1590, 1790 or 1990 MeV/c. The very general trends are the same, but these two experiments clearly disagree with each other as well as this experiment. At 2170 MeV/c the data of Crouch[6] was similar to this experiment at 2190 MeV/c except in the forward direction Crouch obtains approximately twice the cross section of this experiment.

In summary, the general trends indicated by the other experiments are consistent with those seen in this experiment. In detail, particularly at the higher five momenta, the agreement between any of the three experiments is poor. This lack of agreement points out the need for additional accurate experiments in this energy region. One can speculate

that the disagreements are caused by the inability of Refs. 6 and 9 to properly correct for their geometry and background sources, and their poor statistical precision. This experiment also has greater statistical precision than those of Ref. 7 and 8 near 1030 MeV/c.

E. Comparison with Phase Shift Solutions

Since the charge exchange differential cross section depends on the difference between isospin 3/2 and isospin 1/2 scattering amplitudes (Eqn. 5, Sec. I), it can provide a sensitive check on phase shift parameterizations of pion-nucleon scattering. In Figs. 18a-c the data from this experiment is compared with various recent phase shift analyses.[28-30]

At 1030 MeV/c the agreement between the phase shift predictions and the data is fair. At 1590 MeV/c none of the solutions are in reasonable agreement with the data. Note that the two plotted solutions of Almehed and Lovelace[28] while only 20 MeV/c apart, differ considerably in the backwards hemisphere. If this rapid variation is realistic, then these comparisons with the data may only be of general qualitative value as the phase shift solutions are not calculated at exactly the experimental momenta. The solutions plotted are the closest ones available. At 1790 MeV/c and 1990 MeV/c, the solutions of Almehed and Lovelace are in strong disagreement with the data. At the higher two momenta, only Ayed et al.[29] have phase shift solutions available and their agreement is poor. However, the phase shift solutions are at quite different energies from the data.

It is interesting to note how different the phase shift solutions are from each other, indicating the need for additional data in this energy region to constrain the phase shifts. One hopes that with sufficient data, a unique set of phase shifts can be found which will agree with known data and have some predictive powers for reactions not yet measured.

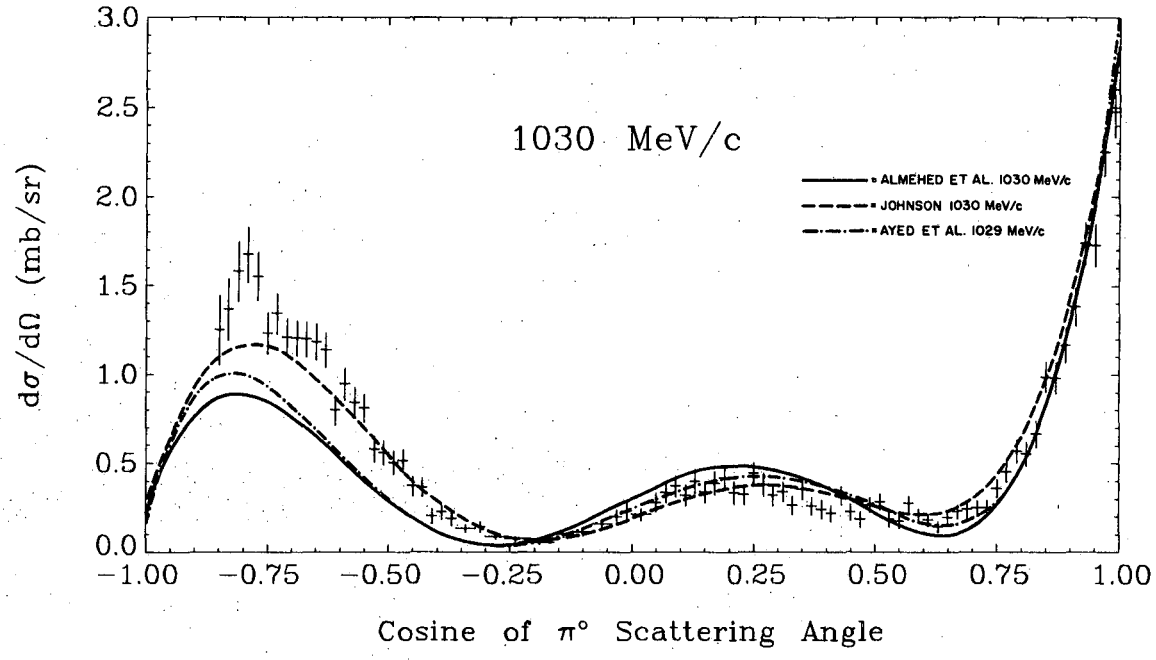

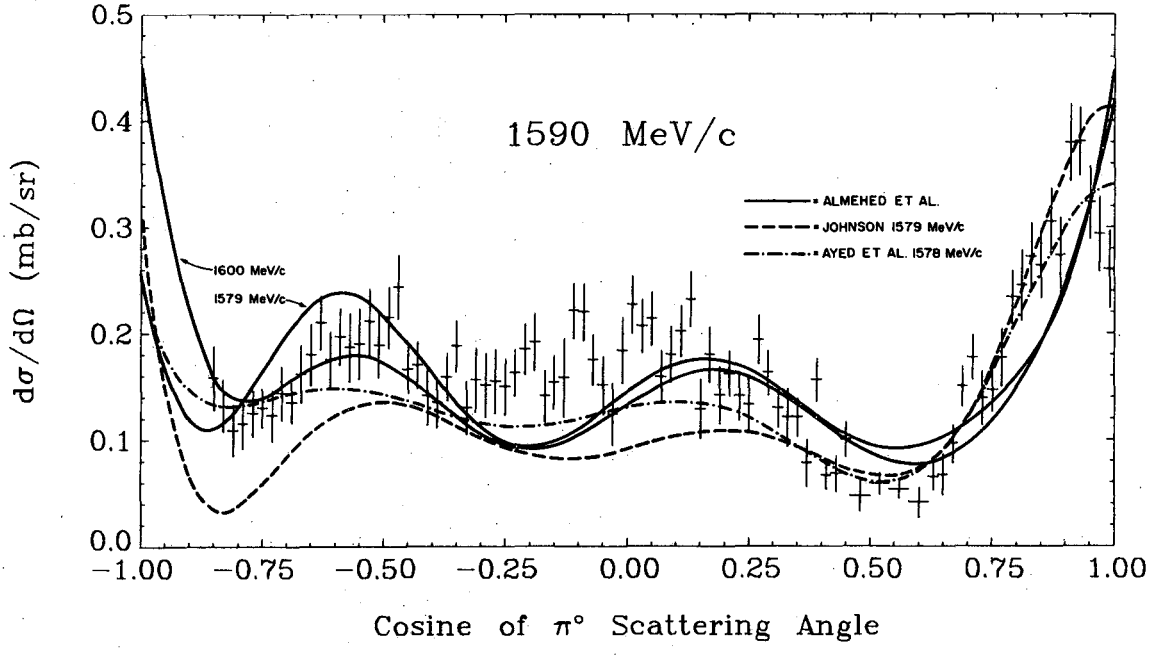

XBL 727-1350

Fig. 18a. Differential cross section for the reactions $\pi^- p \to \pi^0 n$ measured in this experiment compared with plots of the predictions from various extant phase shift sets, none of which are based on the data shown here. See Refs. 28-30.

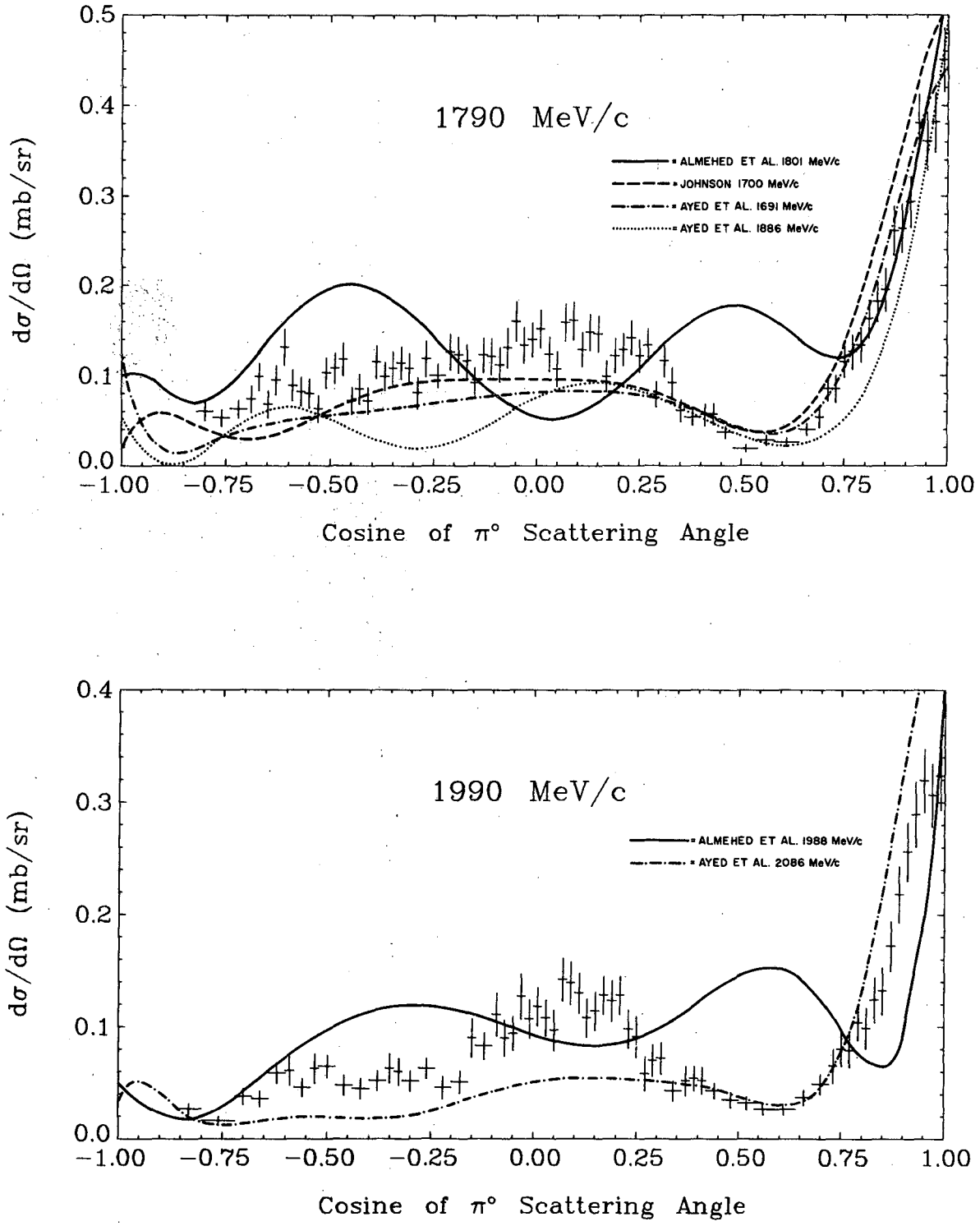

XBL 727-1349

Fig. 18b. Differential cross section for the reaction $\pi^- p \to \pi^0 n$ measured in this experiment compared with plots of the predictions from various extant phase shift sets, none of which are based on the data shown here. See Refs. 28-30.

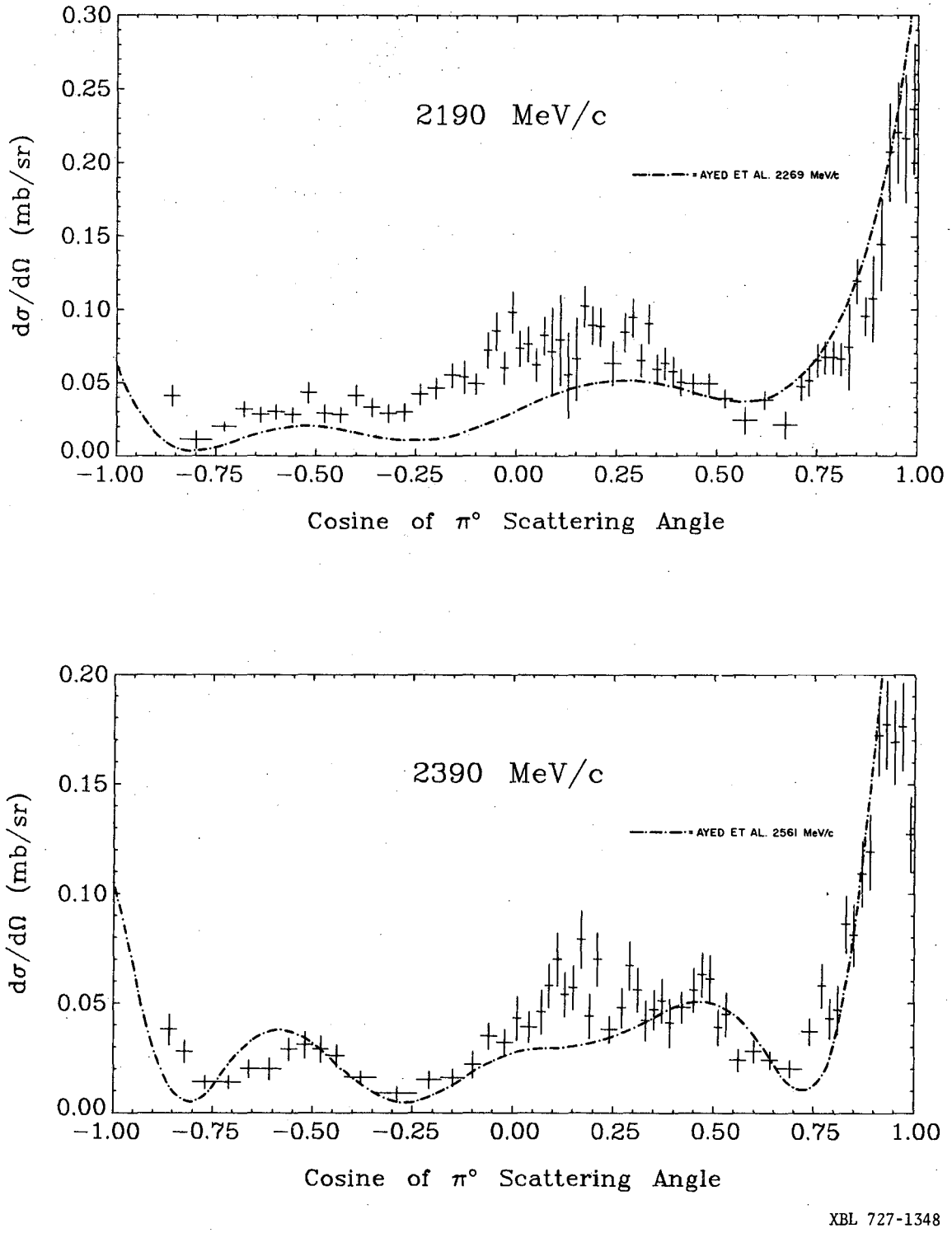

Fig. 18c. Differential cross section for the reaction $\pi^- p \to \pi^0 n$ measured in this experiment compared with plots of the predictions from various extant phase shift sets, none of which are based on the data shown here. See Refs. 28-30.

The phase shift analysis of Almehed and Lovelace[28] used the Legendre coefficients of fits to the charge-exchange differential cross-section of the four experiments[6-9] in the energy range of this experiment. The analysis of Ayed et al.[29] also uses the results of these four experiments. The fact that different groups using the same data can obtain quite different results again underlines the need for extensive, precise charge exchange data.

F. Forward Cross Sections

The cross section in the forward direction may be found by extrapolating the Legendre polynomial fits to $\cos\theta = +1.0$. This is given in Table IX. At any given energy

$$d\sigma/d\Omega(0^0) = (\text{Re } f)^2 + (\text{Im } f)^2$$

where f is the forward scattering amplitude.

Assuming isospin conservation, the optical theorem yields

$$\text{Im } f = \frac{k}{4\pi\sqrt{2}} (\sigma_+ - \sigma_-)$$

where k is the pion c.m. momentum and $\sigma_\pm$ are the $\pi^\pm p$ total cross sections. Forward dispersion relations can be used to calculate Re f.[31,32] Figure 19 shows the comparison of our forward cross section with both the lower limit implied by the optical theorem (the imaginary part of f) and the predictions of $d\sigma/d\Omega(0^0)$ by dispersion relations.[31,32] The results are compatible with the lower limit set by Im f, but at the five higher momenta, they differ significantly from the predictions of dispersion relations. No bias has been discovered in our experimental procedure or method of analysis which could produce such an effect. In particular our charge-exchange total cross-sections appear consistent with other experiments (Fig. 17) and the forward cross section at 1030 MeV/c appears consistent with the predictions of dispersion relations.

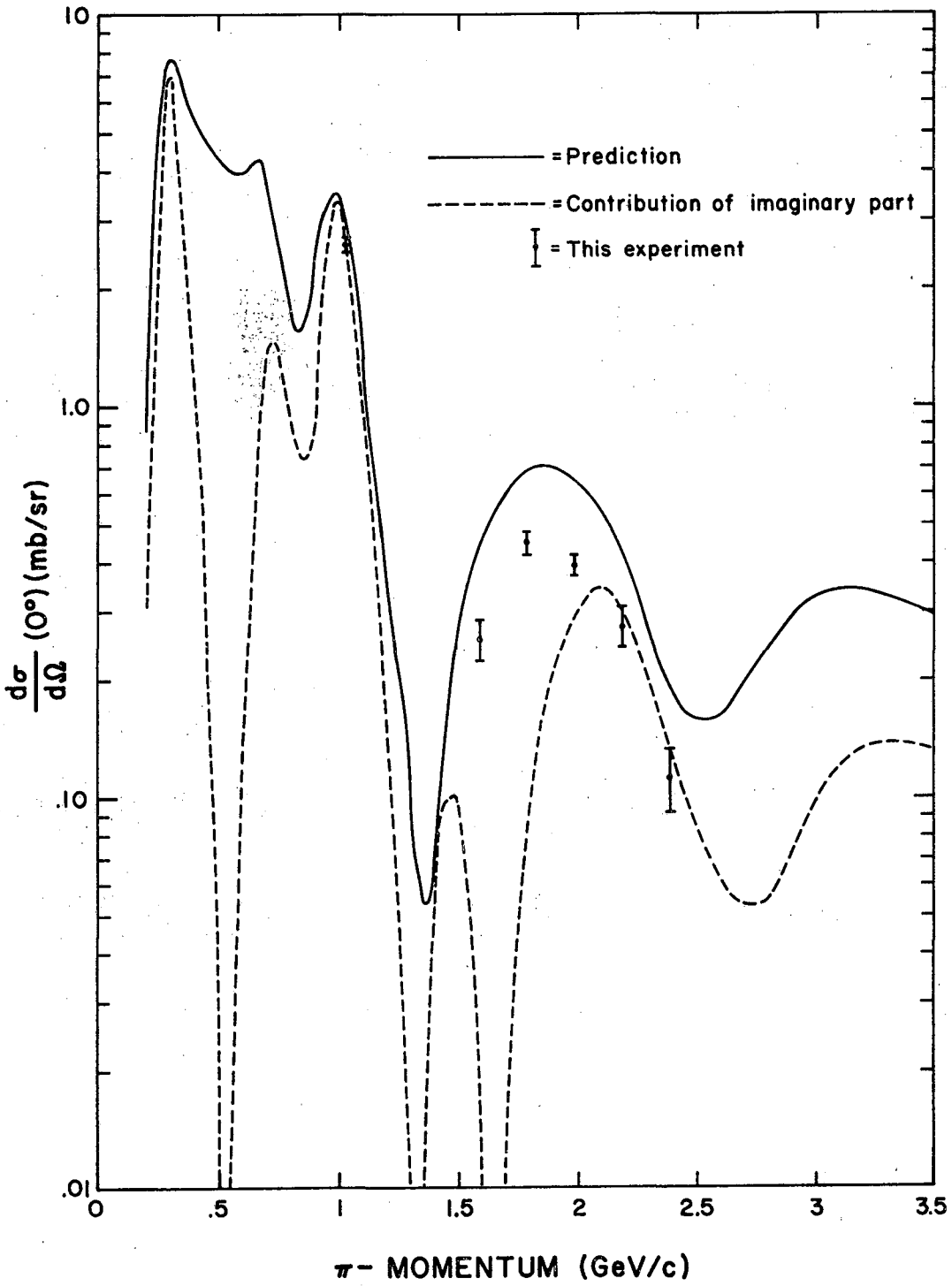

XBL 728-1386

Fig. 19. Our forward differential cross section for the reaction $\pi^- p \to \pi^0 n$ compared with the optical theorem (imaginary part) and dispersion relation predictions (differential cross sections). The uncertainty in the contribution of the real part is ~ 20%. See Refs. 31, 32.

G. The t-Distributions and Comparison with Regge Theory

The t-distributions of the charge exchange cross section are shown in Figs. 20a-c. Both the data and the Legendre polynomial fits are plotted. Figure 21 shows all six momenta on one figure with just the Legendre fits plotted.

At high energies, Regge pole theory provides a description of scattering cross sections, including that of charge exchange.[3-5, 33] In particular, for charge exchange, in simple Regge theory only the ρ trajectory can be exchanged and the vanishing of the spin-flip amplitude at $t \simeq -0.6(\text{GeV}/c)^2$ causes a dip in $d\sigma/dt$ at this point. This dip may be seen here even at these low energies, but its position still moves somewhat with incident momenta.

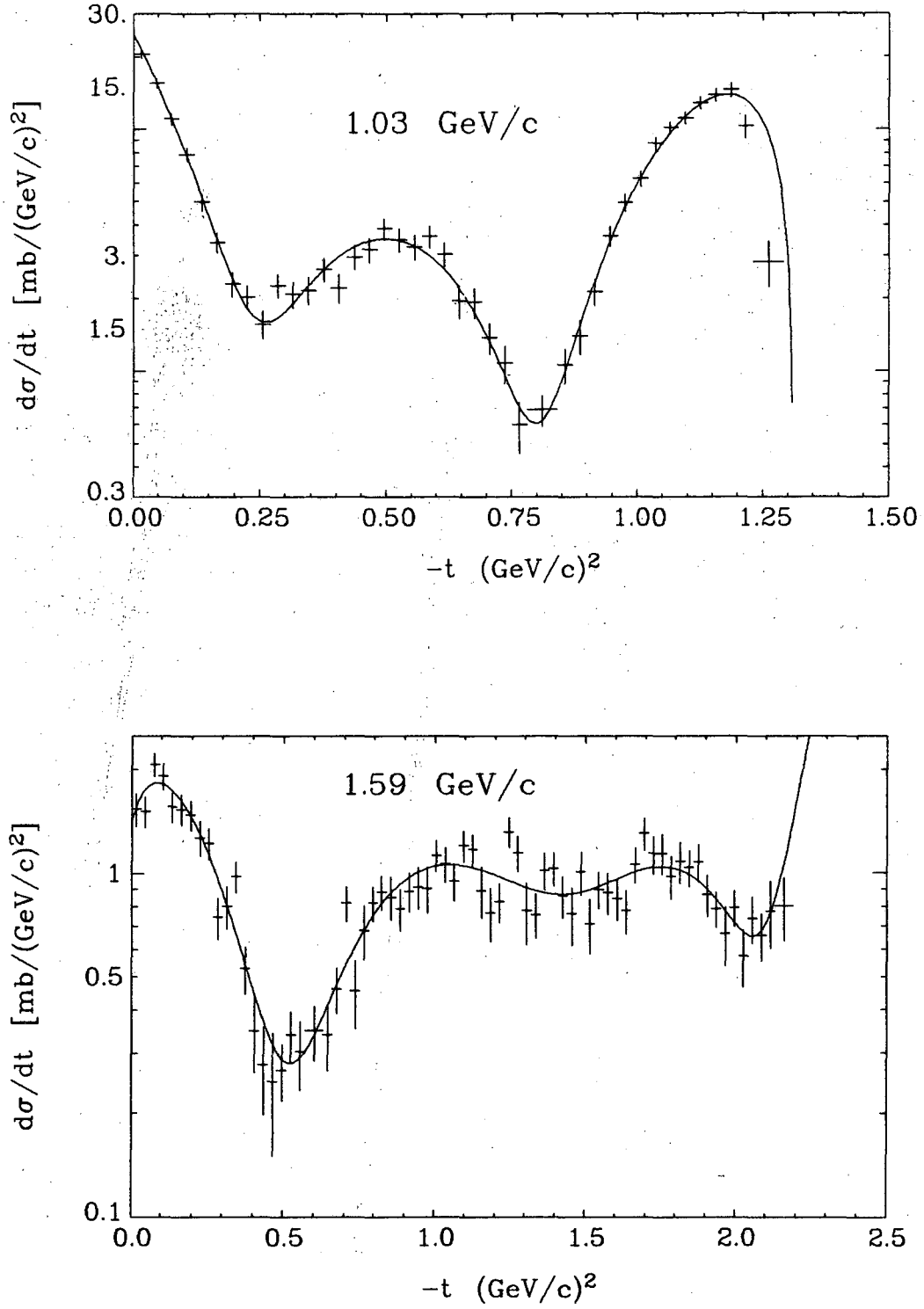

XBL 728-1383

Fig. 20a. The charge exchange differential cross section measured in this experiment plotted as a function of t. The curves are the Legendre fits, given in Table VIII.

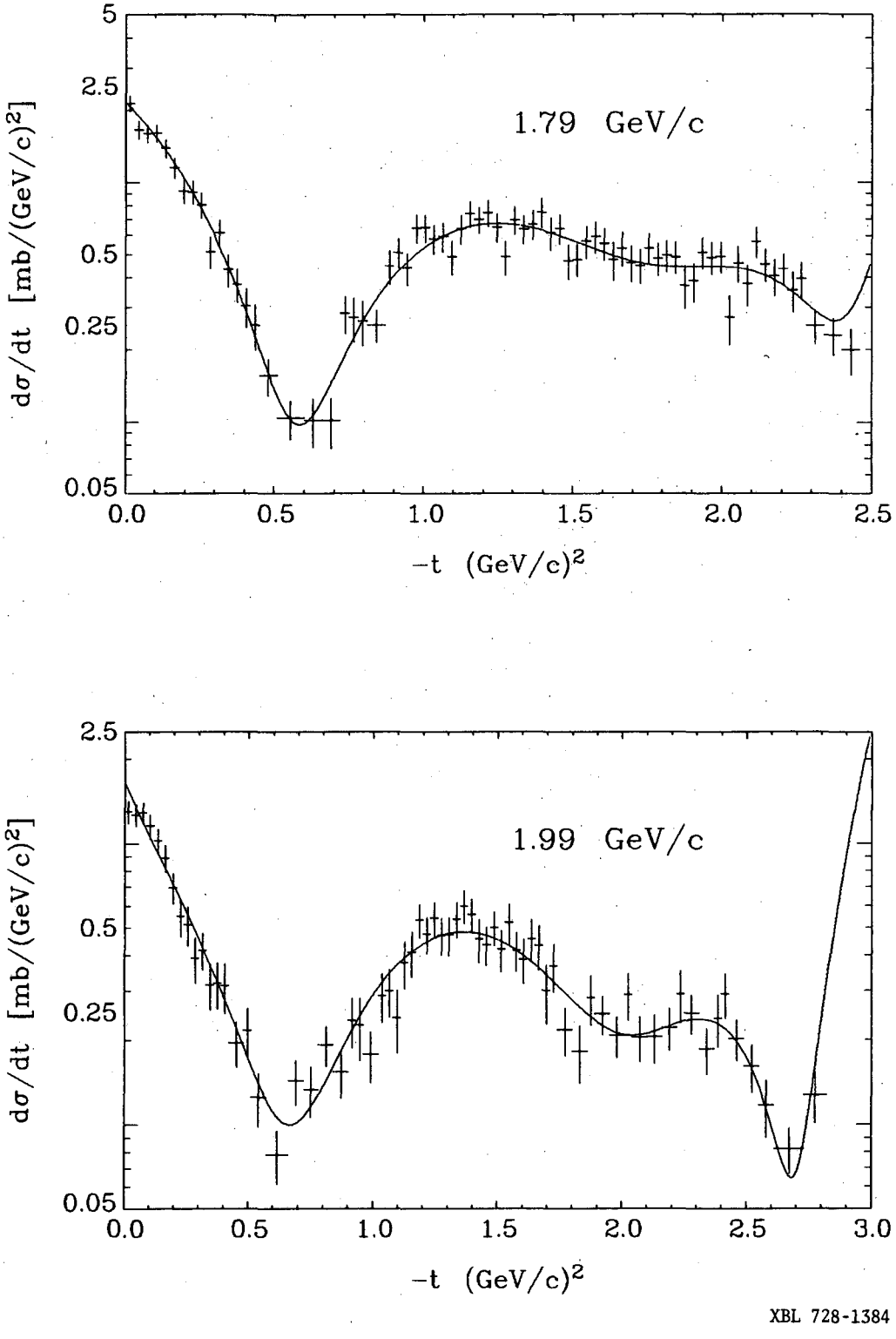

Fig. 20b. The charge exchange differential cross section measured in this experiment plotted as a function of t. The curves are the Legendre fits, given in Table VIII.

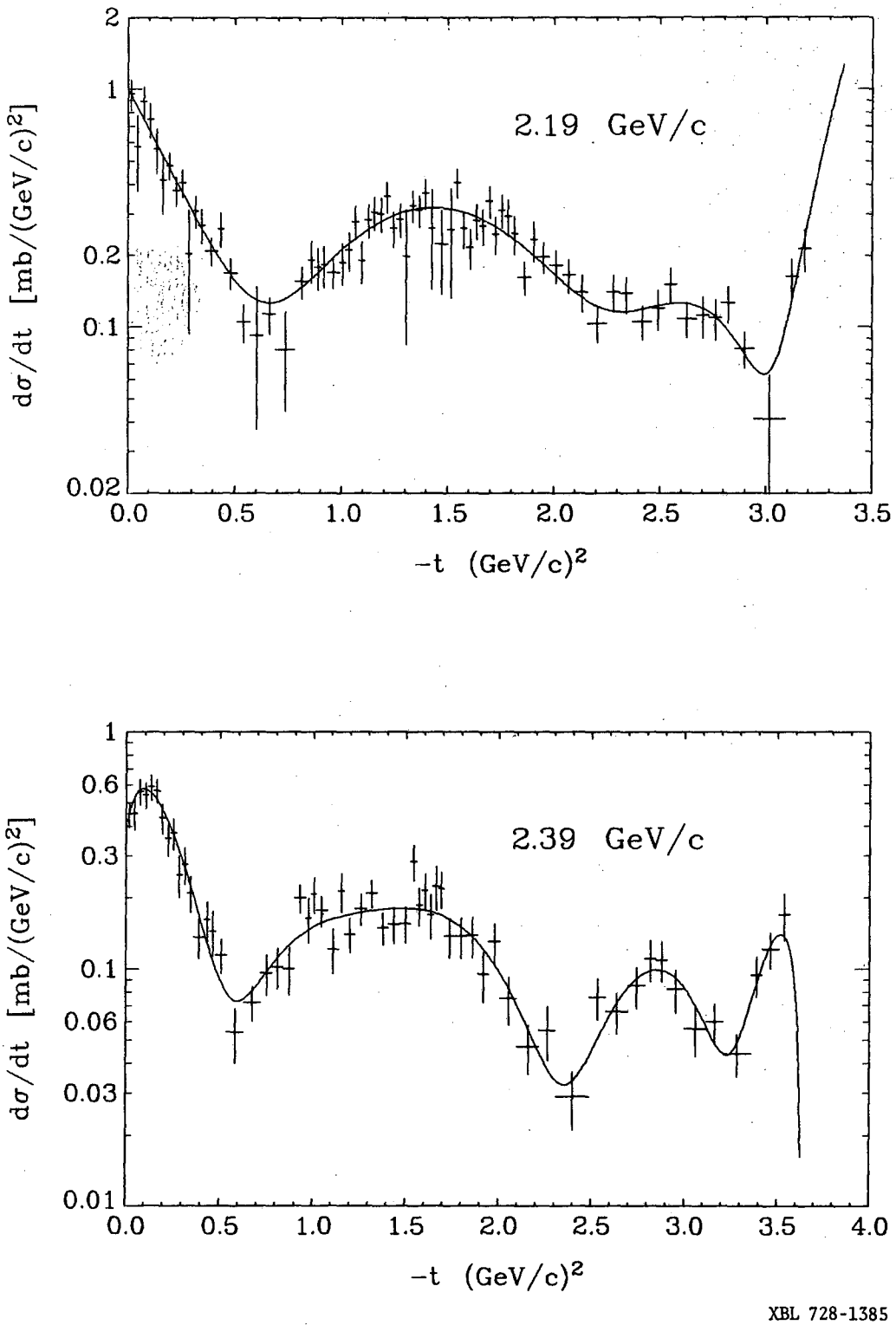

Fig. 20c. The charge exchange differential cross section measured in this experiment plotted as a function of t. The curves are the Legendre fits, given in Table VIII.

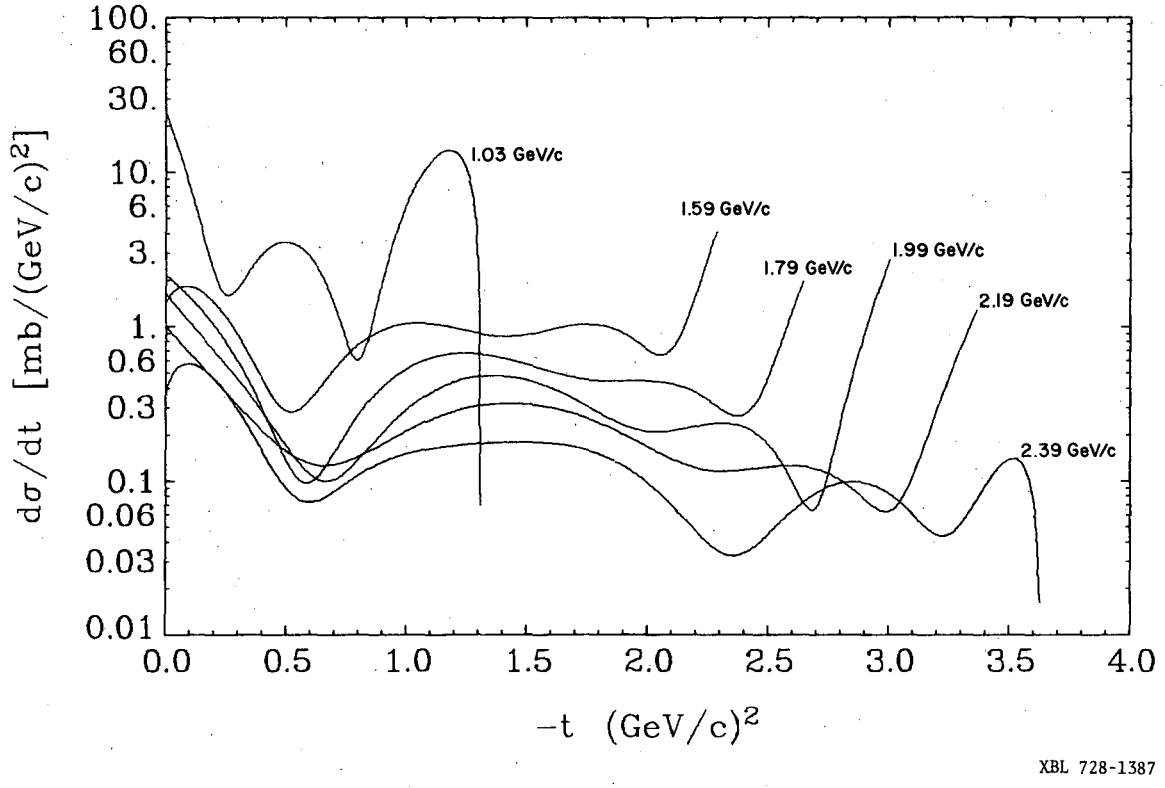

Fig. 21. The Legendre fits to our data plotted as a function of t for all six momenta.

ACKNOWLEDGMENTS

The great interest and support of my various activities by my advisor, Burton J. Moyer, is deeply appreciated.

I am indebted to O. Dahl, R. W. Kenney, M. Pripstein and M. Wahlig for my guidance and professional upbringing during the course of this experiment.

My fellow students, Roger Chaffee, Ivan Linscott, Andris Skuja and Tom Risser have all contributed greatly to my understanding of this research.

I appreciate numerous conversations with Bill Oliver, Sherwood Parker, and Charles Rey concerning the theory and operation of the spark chamber system.

The organization of the extensive amounts of data and the scanning and measuring results is due to the tireless efforts of Ellen Epstein and Bob Hogrefe.

I thank Miriam Machlis for her patience and understanding in typing this thesis and Tim Daly for drawing some of the figures. The CDC 6600 computer and its staff made this thesis possible.

Finally I thank my wife, Vikki Nelson, for her encouragement and patience over these many years.

Work done under the auspices of the U. S. Atomic Energy Commission.

REFERENCES

1. Pion-Nucleon Scattering, ed. G. L. Shaw and D. Y. Wong (John Wiley and Sons, New York, 1969).

2. R. G. Moorhouse, Ann. Rev. Nuc. Sci. 19, 301 (1969).

3. G. Höhler, J. Baacke, H. Schlaile, P. Sonderegger, Phys. Letters 20, 79 (1966).

4. G. Höhler, J. Baacke, G. Eisenbeiss, Phys. Letters 22, 203 (1966).

5. R. K. Logan, Phys. Rev. Letters 14, 414 (1965).

6. H. R. Crouch, jr., R. Hargraves, R. E. Lanou, Jr., J. T. Massimo, A. E. Pifer, A. M. Shapiro, M. Widgoff, A. E. Breener, M. Ioffredo, F. D. Rudnick, G. Calvelli, F. Gasparini, L. Guerriero, G. A. Salandin, A. Tomasin, C. Voci, F. Waldner, Y. Eisenberg, E. E. Ronat, S. Toaff, P. Bastien, B. Brabson, B. T. Feld, V. Kistiakowski, Y. Goldschmidt-Clermont, D. Miller, I. A. Pless, A. Rogers, L. Rosenson, L. Ventura, T. L. Watts, and R. K. Yamamoto, Phys. Rev. Letters 21, 849 (1968).

7. F. Bulos, R. E. Lanou, A. E. Pifer, A. M. Shapiro, C. A. Bordner, A. E. Brenner, M. E. Law, E. E. Ronat, F. D. Rudnick, K. Straugh, J. J. Szymanski, P. Bastien, B. B. Brabson, Y. Eisenberg, B. T. Feld, V. K. Kistiakowsky, I. A. Pless, L. Rosenson, R. K. Yamamoto, G. Calvelli, F. Gasparini, L. Guerriero, G. A. Salandin, A. Tomasin, L. Ventura, C. Voci and F. Waldner, Phys. Rev. 187, 1827 (1969)

8. Charles B. Chiu, Richard D. Eandi, A. Carl Helmholz, Robert W. Kenney, Burton J. Moyer, John A. Poirier and W. Bruce Richards, Phys. Rev. 156, 1415 (1967)

9. A. S. Carroll, I. F. Corbett, C. J. S. Damerell, N. Middlemas, D. Newton, A. B. Clegg and W. S. C. Williams, Phys. Rev. 177, 2047 (1969)

10. Roger Burton Chaffee, "A Study of the Reaction $\pi^- p \rightarrow \eta n$" (Ph. D. Thesis), Lawrence Berkeley Laboratory Report LBL-1060 (1972) (unpublished).

11. Andris Skuja, "A Study of Dipion Production in the Reaction $\pi^- p \rightarrow \pi^o \pi^o n$ between 1.6 and 2.4 GeV/c," (Ph. D. Thesis), Lawrence Berkeley Laboratory Report, LBL-1019 (1972) (unpublished).

12. T. J. Devlin , OPTIK: An IBM 709 Computer Program for the Optics of High Energy Particle Beams Lawrence Radiation Laboratory report UCRL-9727 (1961), and R Chaffee (private communication).

13. T. B. Risser, "Neutral Decays of the η^o Meson," (Ph. D. Thesis) LAwrence Radiation Laboratory Report UCRL-20039 (1970) (unpublished).

14. R. J. Cence, B. D. Jones, V. Z. Peterson, V. J. Stenger, J. Wilson, D. Cheng, R. D. Eandi, R. W. Kenney, I. Linscott, W. P. Oliver, S. Parker, and C. Rey, Phys. Rev. Letters 22, 1210 (1969).

15. C. A. Rey and S. I. Parker, Nuc. Instr. Meth. 24, 314 (1967); 43, 361 (1966).

16. A. R. Clark, L. T. Kerth, Proc. 1966 Inter. Conf. on Instrumentation for High Energy Physics, Stanford, California (1966) page 355.

17. M. Leavitt, LBL Group A programming note P-188 (unpublished).

18. I. Linscott, M. Leavitt, O. Dahl and A. Skuja (private communication).

19. O. I. Dahl, T. B. Day, F. T. Solmitz and N. L. Gould, Group A programming note No. P-126 (unpublished).

20. C. O. Gimber, M. Leavitt and R. Chaffee, LBL Group A Programming note No. P-194 (unpublished).

21. R. Chaffee, C. Rey LBL (private communication).

22. G. Bizard, Y. Declais, J. Duchon, J. L. Laville, J. Seguinot, C. Bricman, J. M. Perreau, and C. Valladas, Phys. Letters 31B, 481 (1970).

23. M. Feldman, W. Frati, J. Halpern, A. Kanofsky, M. Nussbaum, S. Richert P. Yamin, A. Choudry, S. Devons and J. Grunhaus, Nuovo Cimento 50A 89 (1967).

24. Orin I. Dahl, Lyndon M. Hardy, Richard I. Hess, Janos Kirz and Donald H. Miller, Phys. Rev. 163, 1377 (1967).
Orin I Dahl, Lyndon M. Hardy, Richard I. Hess, Janos Kirz, Donald H. Miller and Joseph A. Schwartz, Phys. Rev. 163, 1430 (1967).

25. R. D. Tripp, Baryon Resonances, lectures delivered at the International School of Physics, Enrico Fermi, XXXIII Course, Strong Interactions, (Academic Press, New York, 1966) page 70.

26. Angela Barbaro-Galtieri, Baryon Resonances, Advances in Particle Physics, Vol. II ,ed. R. L.Cool, R. E. Marshak (John Wiley and Sons, 1968).

27. P. Sonderegger et al., Physics Letters 20, 75 (1966).

28. S. Almehed and C. Lovelace, Nuclear Physics B40, 157 (1972).

29. R. Ayed, P. Bareyre, and G. Villet, Physics Letters 31B, 598 (1970).

30. C. H. Johnson, Jr., Lawrence Radiation Laboratory Report UCRL-17683 (1967).

31. G. Höhler, J. Baacke, and R. Strauss, Phys. Letters 21, 223 (1966).
G. Höhler and R. Strauss, Z. Physik. 240, 377 (1970).

32. G. Höhler and R. Strauss, "Tables of Pion-Nucleon Forward Amplitudes," University of Karlsruhe preprint (October 1971).

33. G. Höhler, J. Baake, H. Schlaile and P. Sonderegger, Phys. Letters 20, 79 (1966).

B. R. Desai, Phys. Rev. 142, 1255 (1966).

L. Sertorio and L. Wang, Phys. Rev. 178, 2462 (1969).

G. E. Hite, Rev. Mod. Phys. 41, 669 (1969).

B-1. J. D. Jackson, Classical Electrodynamics (John Wiley and Sons, 1962) page 67.

APPENDICES

A. Analysis of Errors

The dominant uncertainty in the partial cross sections for $\pi^- p \rightarrow n + m\gamma$'s comes from our inability to correctly estimate the number of such events generated in the experiment. To find the true number of i gamma events t_i a number of corrections must be applied to the observed number of i gamma events O_i. In particular we can write

$$O_i = E_{ij} U_{jk} D_{k\ell} V_{\ell m} t_m \tag{A-1}$$

or

$$t_i = V^{-1}_{ij} D^{-1}_{jk} U^{-1}_{k\ell} E^{-1}_{\ell m} O_m \tag{A-2}$$

where

$$O_m = f_m(\text{target full}) - e_m(\text{target empty}) \cdot \left[\frac{\#\pi^-\text{'s for target full}}{\#\pi^-\text{'s for target empty}}\right]$$

and E = the scanning efficiency matrix

U = the feedup matrix

D = the feed-down matrix

V = the neutral final state veto matrix

All are described more fully in Sec. III of the text.

First consider the error in O_m

$$\delta O_m = \delta f_m - \alpha \delta e_m$$

where the error on α is negligible, then

$$\langle \delta O_i \delta O_j \rangle = \delta_{ij} f_i \left[1 + \alpha^2 \left(\frac{e_i}{f_i}\right)\right] \tag{A-3}$$

since there are no correlations between any elements of either vector.

Now consider the general equation

$$V_i = A_{ij} V_j' \tag{A-4}$$

where we wish to find $\langle \delta V_i' \, \delta V_j' \rangle$. To estimate this, differentiate Eq. (A-4) to obtain

$$\delta V_i = A_{ij} \delta V_j' + \delta A_{ij} \, V_j'$$

Assuming

$$\langle \delta A_{ij} \delta V_k' \rangle = 0$$

(since they come from independent sources) we can then obtain

$$\langle \delta V_i' \delta V_j' \rangle = A^{-1}_{ik} \left[\langle \delta V_k \delta V_\ell \rangle + V_m' V_n' \langle \delta A_{km} \delta A_{\ell n} \rangle \right] A^{-1}_{j\ell} \qquad \text{(A-5)}$$

We can apply this formula iteratively on Eq. (A-1) to find the final error matrix $\langle \delta t_i \delta t_j \rangle$. We know $\langle \delta 0_k \delta 0_\ell \rangle$, so all that is needed to carry out this procedure are the arrays

$\langle \delta E_{km} \delta E_{\ell n} \rangle$, $\langle \delta U_{km} \delta U_{\ell n} \rangle$, $\langle \delta D_{km}, \delta D_{\ell n} \rangle$ and $\langle \delta V_{km} \delta V_{\ell n} \rangle$.

We now proceed to calculate these arrays.

1. <u>The scanning efficiency matrix E.</u>

Recall $E_{ij} = n_{ij} / \Sigma_i n_{ij}$ where n_{ij} was the number of true j-gamma events (established by the conflict scan) which had been recorded as i-gamma events. Since the true m-gamma ray and n-gamma ray samples are independent

$$\langle \delta E_{km} \delta E_{\ell n} \rangle = \delta_{mn} \langle \delta E_{km} \delta E_{\ell m} \rangle$$

To obtain the term $\langle \delta E_{km} \delta E_{\ell m} \rangle$ we use the fact that, for a fixed value of N if

$$a + b = N, \; (\delta a)^2 = ab/N$$

Thus, writing $n_{km} + n_{\ell m} + R_m = N_m$ where N_m are the number of true m shower events in the sample that has been conflict scanned and $R_m = N_m - n_{km} - n_{\ell m}$, a little algebra yields the relationship

$$\langle \delta E_{km} \delta E_{\ell m} \rangle = \frac{1}{N_m} \left[E_{km} \delta_{k\ell} - E_{km} E_{\ell m} \right]$$

so

$$\langle \delta E_{km} \delta E_{\ell n} \rangle = \frac{\delta_{mn}}{N_m} \left[E_{km} \delta_{k\ell} - E_{km} E_{\ell m} \right] \qquad \text{(A-6)}$$

2. The Feed-up matrix U

In Sec. III-D we defined

$$U_{ij} = \delta_{ij}(1 - u_1 - u_2) + \delta_{i-1,j}\, u_1 + \delta_{i-2,j}\, u_2$$

then

$$\delta U_{ij} = \delta u_1 \left[\delta_{i-1,j} - \delta_{ij} \right] + \delta u_2 \left[\delta_{i-2,j} - \delta_{ij} \right]$$

assuming the error in u_1 is uncorrellated with that of u_2, i.e.,

$$\langle \delta u_1 \delta u_2 \rangle = 0$$

we obtain

$$\langle \delta U_{km} \delta U_{\ell n} \rangle = (\delta u_1)^2 (\delta_{k-1,m} - \delta_{km})(\delta_{\ell-1,n} - \delta_{\ell n}) \qquad \text{(A-7)}$$

$$+ (\delta u_2)^2 (\delta_{k-2,m} - \delta_{km})(\delta_{\ell-2,n} - \delta_{\ell n})$$

It was assumed $\delta u_1 = .02$ and $\delta u_2 = .01$.

3. The Feed-down Matrix D

In Sec. III-D we defined

$$D_{ij} = \frac{j!}{(j-i)!\,i!}\, d_j^{\,i} (1 - d_j)^{j-i} \qquad i \le j$$

$$= 0 \qquad i > j$$

then

$$\delta D_{ij} = D_{ij}\, \delta d_j \left[\frac{i}{d_j} - \frac{j - i}{1 - d_j} \right]$$

or

$$\langle \delta D_{km} \delta D_{\ell n} \rangle = D_{km} D_{\ell n} \left[\frac{k}{d_m} - \frac{m - k}{1 - d_m} \right] \left[\frac{\ell}{d_n} - \frac{n - \ell}{1 - d_n} \right] \langle \delta d_m \delta d_n \rangle \qquad \text{(A-8)}$$

the expression $\langle \delta d_m \delta d_n \rangle$ was conservatively replaced with $\delta d_m \delta d_n$ where

$$\delta d_i = .005 \qquad i = 0, 1, 2$$
$$= .01 \qquad i = 3, 4, 5, 6, 7, 8, 9$$

4. The Neutral Final State Veto Matrix V

in Sec. III-E we defined

$$V_{ij} = \delta_{ij}(1 - c_1)^j(1 - c_2)(1 - c_3)(1 - c_4)^{\lfloor j/2 \rfloor}$$

then

$$\delta V_{ij} = - V_{ij}\left[\frac{j}{1 - c_1}\delta c_1 + \frac{\delta c_2}{1 - c_2} + \frac{\delta c_3}{1 - c_3}\right]$$

or

$$\langle \delta V_{km} \delta V_{\ell n} \rangle = V_{km} V_{\ell n} \left[\frac{mn}{(1 - c_1)^2}(\delta c_1)^2 + \frac{(\delta c_2)^2}{(1 - c_2)^2} + \frac{(\delta c_3)^2}{(1 - c_3)^2}\right] \qquad \text{(A-9)}$$

since the uncertainties in c_1, c_2 and c_3 are uncorrelated.

It was assumed $\delta c_1 = .005$

$\delta c_2 = .005$

$\delta c_3 = .005$

and as was implied above, $\delta c_4 = 0.0$.

In summary, the error matrix $\langle \delta t_i \delta t_j \rangle$ for Eq. (A-2) can be found by the iterative application of Eq. (A-5) to (A-3) using Eqs. (A-6), (A-7) (A-8) and (A-9). The errors from the diagonal elements of the error matrices after each application of Eq. (A-5) are given in Table V.

B. Kinematics of Two-Gamma Decay

In this appendix equations will be derived which were used in the analysis of the π^o angular distributions. The opening angle distribution of the gamma rays and the relationship between the gamma ray bisector angular distribution and the true π^o angular distribution will be discussed. Unless noted, all calculations are in the center-of-mass of the reaction $\pi^- p \rightarrow \pi^o n$ (the analysis will be valid for any mass π^o) and units will be such that c = 1.

Two body kinematics (reactions such as $\pi^- p \rightarrow \pi^o n$) have the useful property that in the system c.m. the velocity of the particles is not a function of the angle of scatter, thus the π^o can be described by a fixed velocity β, and its angle of scatter.

Two important distributions are needed to relate the bisector and π^o distributions. These are the opening angle distribution $dn/d\phi$, and the distribution $dn/d\delta$ of the magnitude of the angle between the bisector and the π^o, the relevant angles are shown in Fig. B-1.

We first derive the opening angle distribution $dn/d\phi$.

Define $\gamma = E_o/M_o$ $\eta = P_o/M_o$ $\beta = \sqrt{1 - 1/\gamma^2}$

β, E_o, P_o, M_o the velocity, energy, momentum, and mass respectively of the π^o. Let E_1, E_2 be the energies of γ_1 and γ_2. Since $E_o = E_1 + E_2$, specifying E_1 defines E_2 also. This defines the respective momenta P_1, P_2 which in turn defines the angles α, β. Thus we can write the opening angle $\phi(= \alpha + \beta)$ as a function of only one variable, E_1. Thus we can express the opening angle distribution as

$$\frac{dn}{d\phi} = \frac{dn}{dE_1} \frac{dE_1}{d\phi} \qquad (B\text{-}1)$$

Manipulating four vectors easily yields

$$\cos \phi = 1 - \frac{M_o^2}{2(E_1 E_o - E_1^2)}$$

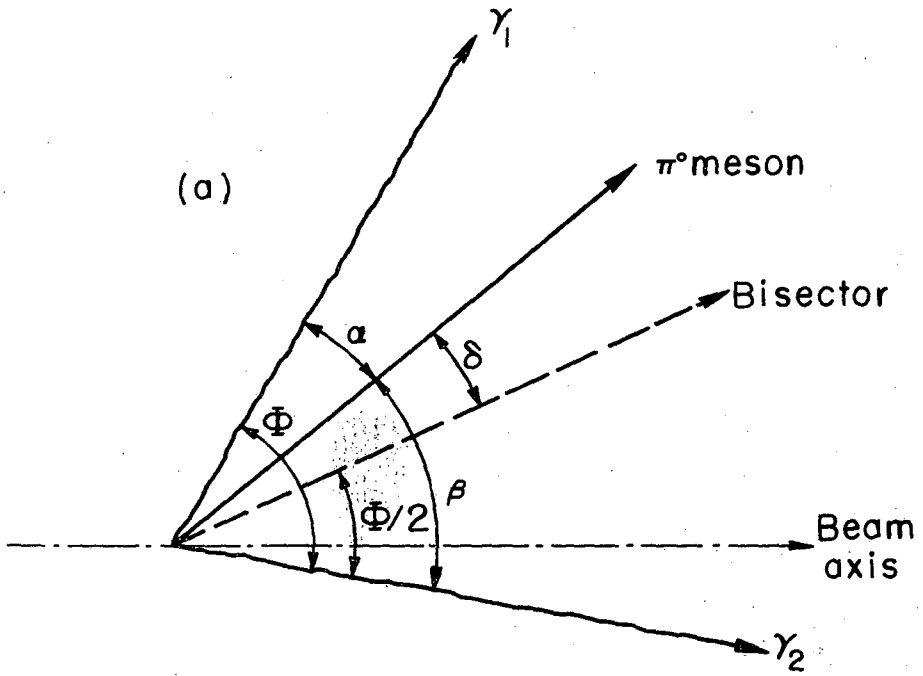

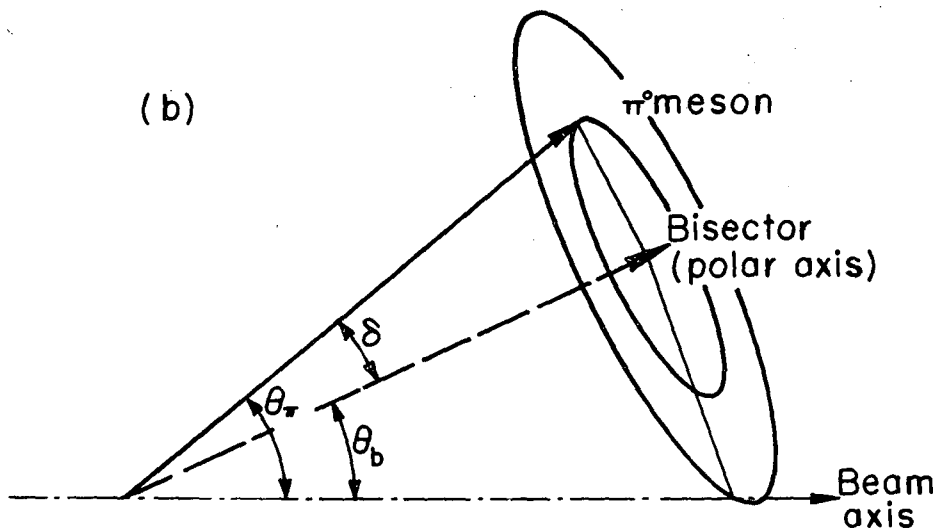

MU-36829A

Fig. B-1. a. Angles used in kinematical equations.

b. Coordinate system for integration of bisector equation.

giving

$$E_1 = \frac{E_o}{2} \pm \sqrt{\frac{E_o^2}{4} - \frac{M_o^2}{2(1 - \cos \phi)}}$$

(B-2)

$$\frac{dE_1}{d\phi} = \pm \frac{M_o^2 \sin \phi}{4(1 - \cos \phi)^2 \sqrt{\frac{E_o^2}{4} - \frac{M_o^2}{2(1 - \cos \phi)}}}$$

where the $\pm$ yields the two possible solutions E_1 and E_2. Now write E_1 in terms of the angle of decay of γ_1 (in the π^o rest frame) with respect to the direction of the π^o. So

$$E_1 = \gamma E_1^* + \eta P_1^* \cos \alpha^*$$

$$dE_1 = \eta P_1^* \, d(\cos \alpha^*)$$

where the * indicates evaluation in the π^o rest frame. Also note that

$$dn = \frac{1}{4\pi} d\Omega^* = \frac{1}{2} d(\cos \alpha^*)$$

so

$$\frac{dn}{dE_1} = \frac{1}{2\eta P_1^*} = \frac{1}{P_o} \qquad \text{(B-3)}$$

Putting Eqs. (B-2) and (B-3) into (B-1) yields

$$\frac{dn}{d\phi} = \frac{1}{4\gamma^2 \beta} \frac{\cos \frac{\phi}{2}}{\sin^2 \frac{\phi}{2} \sqrt{\beta^2 - \cos^2 \frac{\phi}{2}}}$$

Specifying the normalization by

$$\int_{\phi_{min}}^{\pi} \frac{dn}{d\phi} \, d\phi = 1$$

yields

$$\frac{dn}{d\phi} = \frac{1}{2\gamma^2 \beta} \frac{\cos \frac{\phi}{2}}{\sin^2 \frac{\phi}{2} \sqrt{\beta^2 - \cos^2 \frac{\phi}{2}}} \qquad \text{(B-4)}$$

Figure B-2 shows an example of this function and its integral as a function of ϕ.

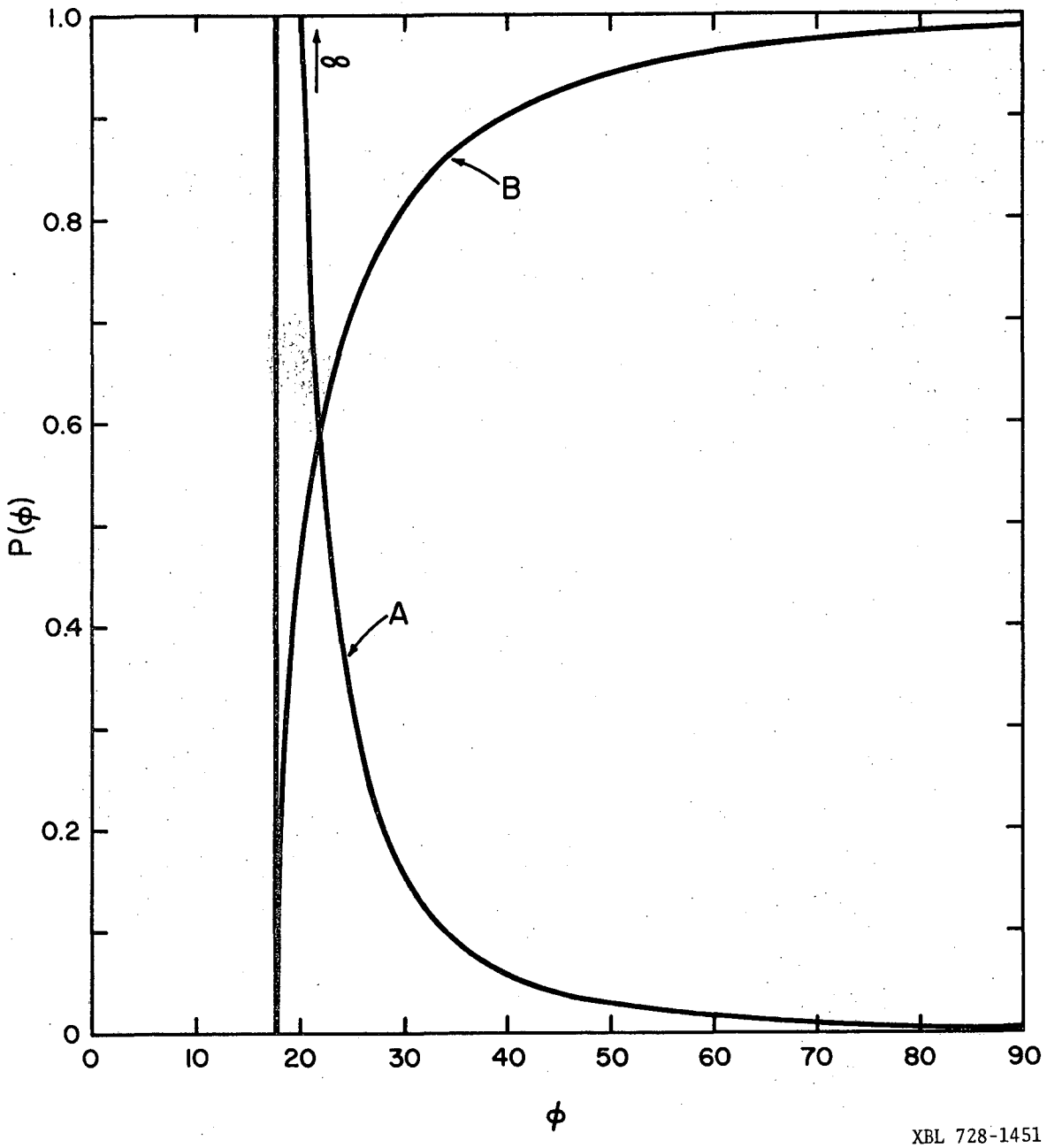

XBL 728-1451

Fig. B-2. Curve A. The theoretical opening angle distribution of decay gammas from charge exchange π^o's in the c.m. system for the 1990 MeV/c. The ordinate is arbitrary.
Curve B. The integrated probability $p(\phi)$ of the opening angle being $\leq \phi$. $p(180^o) = 1$.

To find $dn/d\delta$ write

$$\frac{dn}{d\delta} = \frac{dn}{d\phi}\frac{d\phi}{d\delta} \tag{B-5}$$

Conservation of energy and momentum yield

$$P_o = P_1 \cos\alpha + P_2 \cos\beta$$

$$E_0 = E_1 + E_2$$

$$\frac{P_2}{P_1} = \frac{\sin\alpha}{\sin\beta}$$

Since in our units $E_1 = P_1$ $\quad E_2 = P_2$ $\quad \beta = \frac{P_o}{E_o}$

and $\quad \alpha = \frac{\phi}{2} - \delta \qquad \beta = \frac{\phi}{2} + \delta$

we obtain

$$\beta = \frac{P_1 \cos\alpha + P_2 \cos\beta}{P_1 + P_2} = \frac{\cos\alpha + \frac{\sin\alpha\cos\beta}{\sin\beta}}{1 + \frac{\sin\alpha}{\sin\beta}}$$

$$= \frac{\cos\alpha \sin\beta + \sin\alpha\cos\beta}{\sin\alpha + \sin\beta} = \frac{\sin\phi}{2\sin\frac{\phi}{2}\cos\delta}$$

or $\quad \beta\cos\delta = \cos\frac{\phi}{2} \tag{B-6}$

Thus $\quad \frac{d\phi}{d\delta} = \frac{2\beta\sin\delta}{\sin\frac{\phi}{2}} \tag{B-7}$

Combining (B-4) and (B-7) in (B-5) and using (B-6) to eliminate ϕ gives us

$$\frac{dn}{d\delta} = \frac{\cos\delta}{\gamma^2(1 - \beta^2\cos^2\delta)^{3/2}} \tag{B-8}$$

Alternately

$$\frac{dn}{d(\cos\delta)} = -\frac{1}{\sin\delta}\quad\frac{dn}{d\delta} = \frac{-(1-\beta^2)\cos\delta}{\sqrt{1-\cos^2\delta}\ (1-\beta^2\cos^2\delta)^{3/2}} \tag{B-9}$$

Now we wish to find an expression for the angular distribution of the bisectors, given the angular distribution of the π^o meson. Write

$$\frac{d\sigma}{d\Omega_b} = \int \frac{d^2\sigma}{d\Omega_b d\Omega_\pi} d\Omega_\pi \qquad (B\text{-}10)$$

where

$$\frac{d^2\sigma}{d\Omega_b d\Omega_\pi}$$

is the cross section for events with the bisector direction in the solid angle $d\Omega_b$ and with the π^o direction in the solid angle $d\Omega_\pi$. The integration then is over all π^o directions, holding the bisector direction fixed. We can rewrite

$$\frac{d^2\sigma}{d\Omega_b d\Omega_\pi} = \frac{d\sigma}{d\Omega_\pi} \cdot \frac{dn}{d\Omega_b}$$

where

$$\frac{dn}{d\Omega_b} = \frac{1}{2\pi} \frac{dn}{d(\cos\delta)}$$

and

$$\frac{d\sigma}{d\Omega_\pi} = \sum_\ell C_\ell P_\ell(\cos\theta_\pi)$$

Thus, Eq. (B-10) can be written as

$$\frac{d\sigma}{d\Omega_b} = \frac{1}{2\pi} \sum_\ell C_\ell \int P_\ell(\cos\theta_\pi) \frac{dn}{d(\cos\delta)} d\Omega_\pi \qquad (B\text{-}11)$$

To perform this integration, we can use any coordinate system, so we pick the convenient one with angles measured relative to the axis defined by the bisector direction. With this coordinate system, we can write

$$d\Omega_\pi = d(\cos\delta)d\phi_\pi \qquad (B\text{-}12)$$

This integration can be performed with the aid of the addition theorem for spherical harmonics.[B-1] Stated in our coordinate system it reads

$$P_\ell(\cos\theta_\pi) = P_\ell(\cos\theta_b)P_\ell(\cos\delta) + 2\sum_{M=1}^{\ell} \frac{(\ell - M)!}{(\ell + M)!} P_\ell^M(\cos\theta_b)P_\ell^M(\cos\delta) \times \cos\left[M(\phi_\pi - \phi_b)\right] \qquad (B\text{-}13)$$

where ϕ_b, ϕ_π are the azimuthal angles of the beam direction and π^o direction with respect to the bisector direction.

We can substitute Eqs.(B-12) and (B-13) into Eq. (B-11) and perform the integration over $d\phi_\pi$. The integral over 2π of all terms containing $\cos\left[M(\phi_\pi - \phi_b)\right]$ vanishes, leaving the other terms (not containing ϕ_π) simply multiplied by 2π. Thus

$$\frac{d\sigma}{d\Omega_b} = \sum_\ell C_\ell \left[\int P_\ell(\cos\delta) \frac{dn}{d(\cos\delta)} d(\cos\delta) \right] P_\ell(\cos\theta_b)$$

Or writing $\cos\delta = x$ and putting in Eqs.(B-9) and (B-6) for the maximum opening angle (integrating from $\Delta = 0$ to some maximum)

$$\frac{d\sigma}{d\Omega_b} = \sum_\ell C_\ell \xi_\ell P_\ell(\cos\theta_b) \qquad \text{(B-14)}$$

where

$$\xi_\ell = \int_{\frac{1}{\beta}\cos\frac{\phi_{max}}{2}}^{1} \frac{(1-\beta^2)xP_\ell(x)}{\sqrt{1-x^2}\sqrt{1-\beta^2x^2}}\, dx \qquad \text{(B-15)}$$

with ϕ_{max} being the maximum opening angle which is desired.

Thus we see that the bisector distribution can be related to the π^o angular distribution simply by calculating the ξ_ℓ and observing that the Legendre coefficients of the bisector angular distribution, $\xi_\ell C_\ell$ are related to the Legendre coefficients of the π^o angular distribution C_ℓ. Numerical integration of Eq. (B-15) has been done for the momenta of the data in this paper and is shown in Table B-1.

Table B-I. Values of ξ_ℓ at the momenta of this experiment.

p_{π^-}(MeV/c)	1030	1590	1790	1990	2190	2390
$\beta_{c.m.}(\pi^o)$	.9733	.9844	.9865	.9881	.9893	.9904
ϕ_{min}(deg)	26.54	20.25	18.86	17.71	16.74	15.92
ϕ_{max}(deg)	44.0	34.0	32.0	30.0	29.0	27.0
ξ_0	.8120	.8117	.8152	.8136	.8223	.8131
ξ_1	.8039	.8068	.8109	.8099	.8188	.8100
ξ_2	.7879	.7973	.8024	.8024	.8117	.8040
ξ_3	.7645	.7831	.7898	.7913	.8013	.7950
ξ_4	.7347	.7648	.7734	.7768	.7876	.7832
ξ_5	.6994	.7425	.7534	.7592	.7709	.7687
ξ_6	.6598	.7169	.7303	.7386	.7514	.7518
ξ_7	.6171	.6884	.7044	.7155	.7294	.7327
ξ_8	.5727	.6575	.6763	.6902	.7053	.7115
ξ_9	.5278	.6248	.6463	.6631	.6794	.6886
ξ_{10}	.4836	.5910	.6150	.6346	.6520	.6642
ξ_{11}	.4411	.5567	.5829	.6050	.6236	.6388
ξ_{12}	.4013	.5223	.5505	.5749	.5945	.6124

C. Layman's Summary

The aim of particle physics is to discover the properties of so-called elementary particles and with this description to be able to predict the behavior of particle interactions. As more particles have been discovered, the demands on any given theory have progressively increased.

When atoms were the fundamental units of man's world, relatively simple theories sufficed for describing the characteristics of atoms, i.e., the variety of ways they interact. As experimental measurement techniques improved the discrepancies between simple atomic theories and experiment became apparent and thus more sophisticated and comprehensive theories were needed. Our understanding was significantly expanded when it was realized that the fundamental units of nature were not atoms but rather the smaller building blocks of electrons, neutrons and protons which in special combinations formed atoms. The development of quantum mechanical ideas on how to combine these building bocks, and to describe some of their separate properties provided the essential theory to explain the experimental findings. This substantive increase in understanding required both new building blocks (new particles) and new ways to describe their properties (quantum mechanical ideas).

One of the more elegant aspects of the above synthesis (quantum electrodynamics) was the inclusion and natural explanation of those phenomena variously attributed to photons, light, electromagnetic radiation. The word "photon" will be used hereafter. While making no comment as to why "charge" exists, this theory successfully describes the various properties of charge. Specifically, charges interact with one another by the exchange of photons. This highly successful conceptualization of the interactions

of charges forms a basic framework for many subsequent ideas of elementary particle physics.

While quantum electrodynamics (QED) explained in remarkable detail the properties of charge (atoms, photons, radiation from charged particles, spin, etc.) it offered little explanation as to the properties of atomic nuclei uncovered experimentally during this period. Thus, while QED was a more comprehensive theory than previous ones in that it explained all that previous theories had successfully explained, and a great deal more, it was still not a definitive explanation of particle interactions.

The hypothesis of Yukawa, that the interaction between nucleons was mediated by the exchange of "massive photons"--π mesons, was the first significant step towards an explanation of the short range interactions within the nucleus. The π meson was subsequently discovered, along with a bewildering list of additional particles. Since most of these particles decay rather rapidly, their study has proved to be particularly difficult. This rapid decay also implies that the interactions have great strength (so called strong interactions) which in turn has provided the major obstacle to the successful application of Yukawa's generalization of QED to these particles. In QED, perturbation theory has been used in performing calculations by expanding in powers of the strength of the interaction $\alpha = 1/137$. For QED, this expansion converges rapidly. For strong interactions, the equivalent constant is approximately 1 so this technique fails completely.

At the present time, an adequate theory of strong interactions does not exist. In spite of this lack, a great deal is known, particularly in the form of conservation laws. Energy, momentum, angular momentum,

charge, lepton number and baryon number each seem to be (additatively) conserved quantities for all types of particle interactions. In addition other conservation laws and symmetries appear valid for strong interactions, although not for particle interactions in general. These include the concepts of parity, charge conjugation, time reversal, strangeness and isotopic spin. For example, isotopic spin, is a concept that arose from the observation that for strong interactions, the respective charges of the interacting particles play no role. This observation has been generalized to the idea of a quantum number (analogous to spin) whose z-component represents the actual charge of the system. The interaction is then dependent on the quantum number of isotopic spin, but not on its z-component. This is similar to those atomic interactions which depend on spin, but not its z-component. The hypothesis of isotopic spin is well tested and appears to be correct. Apparent violations at the 1% level are to be expected due to the electromagnetic interactions of the charged particles, but this is, at least formally, separable from the strong interactions.

The most common techniques used to study the strong interactions are those employing energetic collisions of these particles. In particular, with the construction of particle accelerators, beams of protons, neutrons, π^{+}_{-} and K^{+}_{-} mesons can be produced and collided with targets of protons and neutrons. Very crudely, this process is analogous to that of scattering marbles off an object of unknown shape, and then deducing the target's shape by observing the direction of scatter of the marble for many incident marbles. The process is made much more complex by the fact that often, more (and different) marbles scatter off the target than impinge on it.

If one restricts oneself to elastic scattering (same particles after the collision as before the collision) then the situation appears somewhat simpler. Assuming the applicability of quantum mechanics, one can deduce the form of a scattering potential, i.e., the nature of the particle-particle force, by performing scattering experiments, at least in the non-relativistic domain. The mathematical procedure is to consider the incident particle as a superposition of waves of definite angular momentum and the scattered particle as a superposition of outgoing waves of definite angular momentum. The effect of the scatter is to change the phase of each partial wave and possibly to attenuate it. Measurements of the angular distribution of the scattered particles can then define these phase shifts and attenuation coefficients which in turn (in principle) determine the nature of the particle-particle interaction.

Since the π meson in strong interactions appears to have some analogue with the photon in electromagnetic interactions, it is particularly interesting to study the interactions of π mesons with nucleons. The π meson occurs in three charge states +, o , - and appears to be an isospin = 1 particle. The nucleon occurs in two charge states, the proton and neutron, and is describable as an I = 1/2 particle. Consequently π-N interactions can occur in both I = 3/2 and 1/2 states (in analogy to spin), and the scattering parameters for both states need to be determined. As the scattering process is a function of the total energy of the system as well, measurements of π-N scattering need to be made at all energies in order to completely describe the interaction.

Because of isospin, there are a number of elastic reactions that can be studied, for example

$$\pi^+ p \rightarrow \pi^+ p \qquad (1)$$

$$\pi^- p \rightarrow \pi^- p \qquad (2)$$

$$\pi^- p \rightarrow \pi^o n \qquad (3)$$

are three reactions experimentally accessible. All of these must be studied to determine unambiguously the phase shifts for the I = 3/2 and 1/2 states.

This thesis describes a study of the charge-exchange reaction, $\pi^- p \rightarrow \pi^o n$. While this data alone does not define the π-N interaction a unique set of phase shift parameters may be derived in conjunction with known experiments on the first two reactions. In practice the determination of these phase shifts is very complex mathematically and is not done in this thesis. Previous determinations of the phase shifts are compared with the data in this thesis. New calculations of these parameters, incorporating this data will be performed in the near future.

This thesis reports the measurement of the differential cross section $d\sigma/d\Omega(\theta,\phi)$ for reaction (3). There is no dependence on the azimuthal angle ϕ, so the differential cross section (the angular distribution) is only a function of the polar angle defined by the incident π^- and the scattered π^o, and of course the total energy of the system. The differential cross section describes the actual amount of scatter as well as the angular distribution. The observed differential cross section is fit with a Legendre polynomial series. This serves two functions: (1) it provides a simple representation of the data itself and (2) it provides limited information on the nature of the phase shifts. The differential

cross section can be written as the absolute square of the sum of the outgoing partial waves. This sum is simply another Legendre series, so the coefficients determined experimentally are a well defined function of the phase shifts of the scattered partial waves. For instance, the order of the fit needed is simply twice the highest angular momentum which is significantly scattered. Integrating over all scattering angles, we can write

$$\sigma_{total} = \int \frac{d\sigma}{d\Omega} \, d\Omega$$

where σ_{total} represents the total cross section for this reaction. (Cross sections are usually measured in barns, 1 barn = 10^{-24} cm^{+2}. Thus the total cross section is some measure of the cross sectional area of the target.)

Because the nucleon has spin, the scattering process is somewhat more complex than described above (the π has 0 spin). To unravel the complexities introduced by spin, scattering experiments with polarized protons (the proton spin aligned in a magnetic field) must also be performed. These have been performed at many energies for reactions (1) and (2) and are currently underway for reaction (3). With all of this information, one hopes to determine the phase shifts unambiguously and thus one can potentially find a simple way to understand π-N interactions. Further generalizations could potentially lead to a more complete understanding of strong interactions.

TECHNICAL INFORMATION DIVISION
LAWRENCE BERKELEY LABORATORY
UNIVERSITY OF CALIFORNIA
BERKELEY, CALIFORNIA 94720